NAVAL POSTGRADUATE SCHOOL

Monterey, California

THESIS

SATELLITE PRECIPITATION ANALYSIS FOR A DEVELOPING NORTH PACIFIC OCEAN CYCLONE

by

Timothy F. Sheridan

December 1988

Co-Advisor	Carlyle H. Wash
Co-Advisor	Philip A. Durkee

Unclassified

security classification of this page

REPORT DOCUMENTATION PAGE

1a Report Security Classification: Unclassified		1b Restrictive Markings	
2a Security Classification Authority		3 Distribution Availability of Report: Approved for public release; distribution is unlimited.	
2b Declassification Downgrading Schedule			
4 Performing Organization Report Number(s)		5 Monitoring Organization Report Number(s)	
6a Name of Performing Organization: Naval Postgraduate School	6b Office Symbol (if applicable): 35	7a Name of Monitoring Organization: Naval Postgraduate School	
6c Address (city, state, and ZIP code): Monterey, CA 93943-5000		7b Address (city, state, and ZIP code): Monterey, CA 93943-5000	
8a Name of Funding Sponsoring Organization	8b Office Symbol (if applicable)	9 Procurement Instrument Identification Number	
8c Address (city, state, and ZIP code)		10 Source of Funding Numbers	
		Program Element No	Project No / Task No / Work Unit Accession No

11 Title (include security classification): SATELLITE PRECIPITATION ANALYSIS FOR A DEVELOPING NORTH PACIFIC OCEAN CYCLONE

12 Personal Author(s): Timothy F. Sheridan

13a Type of Report	13b Time Covered	14 Date of Report (year, month, day)	15 Page Count
Master's Thesis	From To	December 1988	83

16 Supplementary Notation: The views expressed in this thesis are those of the author and do not reflect the official policy or position of the Department of Defense or the U.S. Government.

17 Cosati Codes			18 Subject Terms (continue on reverse if necessary and identify by block number)
Field	Group	Subgroup	Meteorology, Satellite Remote Sensing, Precipitation Analysis

19 Abstract (continue on reverse if necessary and identify by block number)

Three satellite-based precipitation techniques are used to analyze the precipitation pattern associated with a developing winter cyclone over the eastern North Pacific Ocean. A visible infrared technique, developed by the Naval Postgraduate School (NPS), uses cloud-top temperature and albedo thresholds to produce a rain estimate. A microwave method, based on an algorithm made by the Hughes Aircraft Company (HAC), retrieves rain rate estimates based on both the thermal emission at 19 GHz and the scattering by precipitation-size ice at 37 GHz. Another microwave technique identifies rain coverage based solely on the high sensitivity of 85 GHz channels to ice scattering above the freezing level. A polarization corrected temperature (PCT) is formulated to isolate the 85 GHz precipitation effect.

A subjective evaluation and comparison of the rain estimations are performed. The NPS technique produces representative results within the warm front, but appears to underestimate potential rain associated with the cold front. The HAC retrieval provides a synoptically realistic analysis of the cyclone's rain pattern, but does not resolve the potential precipitation within the isolated, convective clouds behind the cyclone. The PCT method gives a representative coverage of the convective activity within the cyclone and its surrounding area, but does not depict the potential rain areas associated with stratiform clouds.

20 Distribution Availability of Abstract	21 Abstract Security Classification	
☒ unclassified unlimited ☐ same as report ☐ DTIC users	Unclassified	
22a Name of Responsible Individual: Carlyle H. Wash Philip A. Durkee	22b Telephone (include Area code): (408) 646-3465 2295	22c Office Symbol: 63Wx 63De

DD FORM 1473,84 MAR — 83 APR edition may be used until exhausted. All other editions are obsolete — security classification of this page

Unclassified

Approved for public release; distribution is unlimited.

Satellite Precipitation Analysis for a Developing North Pacific Ocean Cyclone

by

Timothy F. Sheridan
Lieutenant Commander, United States Navy
B.S., St. Louis University, 1976

Submitted in partial fulfillment of the
requirements for the degree of

MASTER OF SCIENCE IN METEOROLOGY AND OCEANOGRAPHY

from the

NAVAL POSTGRADUATE SCHOOL
December 1988

Author: Timothy F. Sheridan

Timothy F. Sheridan

Approved by:

Carlyle H. Wash, Co-Advisor

Philip A. Durkee, Co-Advisor

Robert J. Renard, Chairman,
Department of Meteorology

Gordon E. Schacher,
Dean of Science and Engineering

ABSTRACT

Three satellite-based precipitation techniques are used to analyze the precipitation pattern associated with a developing winter cyclone over the eastern North Pacific Ocean. A visible infrared technique, developed by the Naval Postgraduate School (NPS), uses cloud-top temperature and albedo thresholds to produce a rain estimate. A microwave method, based on an algorithm made by the Hughes Aircraft Company (HAC), retrieves rain rate estimates based on both the thermal emission at 19 GHz and the scattering by precipitation-size ice at 37 GHz. Another microwave technique identifies rain coverage based solely on the high sensitivity of 85 GHz channels to ice scattering above the freezing level. A polarization corrected temperature (PCT) is formulated to isolate the 85 GHz precipitation effect.

A subjective evaluation and comparison of the rain estimations are performed. The NPS technique produces representative results within the warm front, but appears to underestimate potential rain associated with the cold front. The HAC retrieval provides a synoptically realistic analysis of the cyclone's rain pattern, but does not resolve the potential precipitation within the isolated, convective clouds behind the cyclone. The PCT method gives a representative coverage of the convective activity within the cyclone and its surrounding area, but does not depict the potential rain areas associated with stratiform clouds.

TABLE OF CONTENTS

LIST OF TABLES

LIST OF FIGURES

ACKNOWLEDGMENT

I would like to express my gratitude to Dr. Carlyle Wash and Dr. Philip Durkee, my thesis advisors, for their strong support and direction throughout this project. Special thanks to Craig Motell and Donna Burych for spending many hours programming the microwave data so it would display on the Naval Postgraduate School computer. Many thanks to Rick Kohrs for his work in preparing the satellite data output. I also wish to acknowledge those who provided the satellite data for this research project: Naval Research Laboratory, SCRIPPS Institution of Oceanography, University of Wisconsin and Dr. Andy Goroch of the Naval Environmental Prediction Research Facility.

I. INTRODUCTION

There are ever-increasing demands for more and better rainfall determination to aid military, scientific and economic decision making. Rain is certainly a critical parameter in naval operations. It results in a decreased performance of flight, amphibious, weapons and acoustic operations. Also, the ability of a ship to "hide" in the radar return of precipitation is a tactically advantageous factor.

Rainfall is also important because it is the primary input into the hydrologic cycle. It plays a critical role in the dynamics of the earth's atmosphere. The latent heat released by precipitation is the largest source of atmospheric heating in the tropics and a significant heat source in the temperate latitudes as well (Wilheit, 1986). Understanding the atmosphere demands high-quality measurements of precipitation. Rainfall studies are growing in significance also because of the steep upward demand for water supplies as populations, living standards and expectations continue to rise in many parts of the world. The need for precipitation monitoring is certain to continue growing.

Precipitation is one of the most variable elements of weather. It varies appreciably with respect to its frequency, duration, intensity and areal coverage, not to mention the different types (rain, hail, sleet and snow). In view of the significant variability of rainfall, it is not surprising that monitoring it with the desired detail and accuracy is often difficult. Measurement of rainfall by gauges is affected in particular by the interrelated factors of topography, site, wind and gauge design (Barrett and Martin, 1981). Surface-based weather radar has the singular advantage over gauges of providing a spatially continuous view of rainfall. However, there is a comparable range of problems which accompany the use of such a system. The problems relate to an unresolved relationship of backscattered microwave energy to drop size spectrum, partial filling of the radar beam, attenuation of the radar beam by intervening drops, absorption and reflection by the ground (anomalous propagation), and signal calibration (Barrett and Martin, 1981). More importantly, the present network for rainfall monitoring around the world by these conventional means is deficient. There are obvious practical and economic problems of maintaining raingauge and surface radar networks over many types of surfaces, including oceans, areas of high relief, high latitudes, deserts, etc. Consequently, rainfall data are inadequate for military operations, hydologic science, weather forecasting and climate studies over most of the globe. Spaceborne remote

sensing can help resolve these problems and figures to be a major component of any global-scale precipitation monitoring system.

Already, satellite remote sensing has begun to play an important part in the parameterization of the rainfall input into the hydrologic cycle. Many different techniques have been developed and tested for such purposes. These include:

- Visible and infrared techniques, which derive rainfall estimates from satellite imagery through models which relate the indirect evidence of rainfall derived from cloud analyses to either ground calibration data, and or to physical expectations based on cycles of cloud growth and dissipation.
- Microwave techniques, which have yielded rainfall estimates from the physically more direct evidence of radiation emanating from the active rain areas themselves, embedded within the clouds.

Infrared and visual imagery have good spatial resolution but represent observations of the tops of the clouds only. Therefore, precipitation methods using infrared and visual data are indirect estimations. Microwave radiation is not affected by most clouds and represent a great potential for improved satellite observation of rain. However, high-spatial resolution is difficult to achieve in microwave sensors (Wilheit, 1986). A system of exploiting the complimentary strengths of visual, infrared and microwave techniques provides the best opportunity for immediate improvements in rainfall estimates.

The Naval Postgraduate School's (NPS) Department of Meteorology has recently developed a satellite-derived cloud and precipitation analysis program using infrared and visible data from the Geostationary Operational Environmental Satellite (GOES) and the National Oceanic and Atmospheric Administration (NOAA) Advanced TIROS-N weather satellite (Wash et al., 1985). The Navy plans to incorporate passive microwave measurements of precipitation into the Tactical Environmental Support System (TESS), a satellite processor and display unit primarily designed for shipboard operations. TESS will utilize data from the Special Sensor Microwave Imager (SSM I) which is flying on the latest Defense Meteorological Satellite Program (DMSP) spacecraft F-8.

The primary purpose of this thesis is to improve the current understanding of rainfall determination by evaluating the combined analyses of precipitation measurements from visual, infrared and microwave data for a rapidly developing cyclone over the eastern North Pacific Ocean. The objectives of this study are:

- Describe the cyclone in its developing stage using the infrared and visual satellite data.
- Estimate precipitation from the infrared and visual data with the NPS precipitation analysis model.

- Analyze SSM I microwave radiance data of the cyclone for comparable times.
- Estimate precipitation from the microwave data using two methods.
- Subjectively evaluate the estimates based on the data and available ship observations.

Background concerning rainfall estimation from satellite imagery is discussed in the next chapter. Chapter 3 describes the NPS precipitation analysis model and the microwave rain retrieval algorithms. Analysis of the data along with an evaluation of the precipitation results are presented in Chapter 4 followed by conclusions and recommendations (Chapter 5).

II. BACKGROUND

A variety of approaches using satellite observations have been applied to the precipitation-estimation problem. Many of these have met with a measure of success. This chapter describes the basic properties of visible, infrared and microwave imaging and background information on the methods of each for monitoring rainfall.

A. RAINFALL FROM VISIBLE AND INFRARED IMAGES

1. Infrared Images

Satellite infrared images are composed of radiant energy originating in the atmosphere or from land and water surfaces below. The intensity of this energy, integrated over all wavelengths, is by the Stephan-Boltzmann law, proportional to the fourth power of temperature. If the medium emits spectral radiant energy corresponding to some temperature less than its thermal temperature, a second factor is introduced. This is the emissivity, ε , a measure of emission efficiency. Some surfaces in nature approach black body emission ($\varepsilon = 1$), but typically emission is by "grey bodies", where $0 < \varepsilon < 1$. Except for thin cirrus, clouds are opaque to infrared radiation and closely approximate black body emitters.

For most remote sensing purposes, infrared refers to wavelengths between 8 and 12.5 microns where emission from terrestial temperatures is maximized and a pronounced "window" exists. In this atmospheric window, absorption (and re-emission) is strong for clouds and slight for the gaseous constituents of the atmosphere. The temperature calculated from observed intensity of radiation is called the "brightness temperature". Only if $\varepsilon = 1$ does the brightness temperature equal the blackbody temperature.

The value of infrared measurements of rainfall estimation lies in the ability to relate atmospheric temperatures to cloud heights. If temperature is known as a function of height, either by actual sounding or from climatology, the height of a cloud may be inferred from the satellite infrared observations. Ordinarily, "grey" clouds are of no consequence in this context, because $\varepsilon < 1$ implies clouds which are thin (and, therefore, without precipitation). The problem of estimating rainfall from infrared data is distinguishing between cold clouds which are thick but are confined to the upper or middle troposphere, and cold clouds which extend into the lower troposphere.

2. Visible Images

Measurements of reflected solar radiation are made primarily in the visible window region, .3 to .7 micron. Factors which determine how effectively a precipitating cloud will reflect incident solar radiation are cloud composition, drop size distribution and cloud thickness. Clouds are made up of either water droplets (10 to 15 microns in diameter) or ice crystals. Cloud types of interest in this study are composed of water droplets which are significantly more reflective (bright) than ice crystal clouds. Clouds containing larger droplets, and more droplets per unit volume, reflect more light. These conditions commonly occur in precipitating clouds, where strong vertical motions and low level convergence of moisture flux are present. Thick clouds, and multiple layers of clouds, are more reflective than thin clouds. In visible satellite images, convective clouds typically have the brightest appearance.

Plank et al. (1955) measured reflectivity in a one-year sample of clouds near Boston with a vertically pointing radar. Thickness in stratiform clouds was well correlated with occurrence of precipitation. Precipitation was present in all clouds of thickness greater than 304 m (10,000 ft) or top temperature between -10 and -20° C.

In addition to cloud top temperature, the distinction between marine clouds (mainly onshore flow) and continental clouds (mainly offshore flow) was found to be important. In a study at Adelaide, South Australia, continental clouds produced substantial rain only when top temperatures were colder than -15° C and thicknesses were greater than 4600 m (15,000 ft). Comparable marine clouds produced heavier individual rainfalls. Clouds greater than 4600 m in thickness comprised less than one-third of raining clouds, but produced almost 50 % of rainfall. Thickness was especially important for marine clouds warmer than -10° C. No cases of rain were reported from clouds less than 600 m (2000 ft) thick. (Barrett and Martin, 1981).

From the above studies, Barrett and Martin (1981) concluded that "(a) as cloud thickness increases, precipitation is more probable and its intensity is likely to be greater, and (b) the relationship is stronger for clouds warmer than about -15° C".

3. Bispectral Estimation of Rainfall

Bispectral schemes combine elements of infrared and visible imagery to map the extent and distribution of precipitation. By themselves, these data sometimes fail to provide accurate information on where rain is falling and not falling. Together, they may succeed.

In the history of rain measurement by bispectral methods the study of Lethbridge (1967) is a major milestone. This study relates TIROS-IV window infrared

radiation to probability of precipitation for a late spring period. As expected, the probability of precipitation occurring during the three hours following satellite passage increased as the infrared temperature decreased, but was only as high as 50 % even for T < 249K. For reflected shortwave radiation, three hour precipitation probability was somewhat higher, reaching 65 % for radiance exceeding 35 Wm^{-2}. But the strongest relationships were found for infrared window and visible radiation together. Three-hour probabilities increased from 5 % for dark, warm scenes to 75 % for bright, cold scenes. For twelve-hour periods the probability of precipitation was as high as 85 %. Thus, Lethbridge concluded that cloud brightness is important because it distinguishes between low cloud and no cloud for high radiation temperatures, and thin cloud and thick cloud for low temperatures.

Other studies in the area of rainfall estimation were handicapped by problems of data location, time differences, instrument calibration, and variable visible viewing and illumination geometry. These constraints were mostly overcome in the study of Lovejoy and Austin (1979). Their technique combines geostationary satellite visible and infrared data; radar data were used to calibrate it. They divided rain subsets of the data by low or high intensity. The heavy rain classes tended to be brighter and colder. When compared with the radar data, rain area was highly correlated with rain amount, but area was weakly correlated with rain intensity. Thus Lovejoy and Austin concluded that determining rain area may be sufficient to achieve reasonable accuracy in an estimate of rain amount.

The objective of a study by Liljas (1982) was to apply a similar approach as that of Lovejoy and Austin's, but without the radar to calibrate it. It was developed for both frontal and convective precipitation. The method starts with the classification of cloud types into cumulonimbus and nimbostratus. As found by Lovejoy and Austin, clouds with very cold tops give the heaviest precipitation. A requirement for precipitation is that the cloud top temperature should be colder than -12° C. The indicated precipitation was compared with the available synoptic observations, airfield observations and four recording rain gauges. The method was found to give good information on the distribution of precipitation. It gives an indication of the relative intensity of rain both in fronts and in showers. It was also possible to detect intense precipitation in mesoscale cloud clusters between the synoptic ground stations. The NPS satellite-derived cloud and precipitation analysis program follows Liljas' rain estimation technique. Additional information regarding the NPS model is presented in Chapter 3.

B. RAINFALL FROM MICROWAVE REMOTE SENSING

1. General Properties of Microwave Radiation

For most meteorological purposes, the microwave portion of the spectrum extends from frequencies near one gigahertz (GHz) to frequencies of a few hundred GHz. In wavelengths this is approximately from 30 cm to 0.1 cm. The transmission characteristics of the atmosphere in the microwave spectrum are shown in Fig. 1 (from Rosenkranz, 1978). The three curves shown are: opacity due to oxygen (lower curve), opacity with 20 kg m^2 water vapor added to the oxygen (middle curve), and opacity with 0.2 kg m^2 stratus cloud added to the oxygen and water vapor (upper curve). The dominant features on the figure are resonant lines of oxygen between 50 and 70 GHz and at 119 GHz, and resonant lines of water vapor at 22 GHz and 183 GHz. At frequencies in the 10 to 50 GHz range, radiation in the microwave portion of the spectrum penetrates clouds, but is strongly absorbed by rain. This provides the potential for measuring rain from space (Wilheit et al., 1977).

Microwave radiation may be absorbed, reflected or scattered. Its behavior depends on elements of the Earth and atmosphere, whose influence depends in turn on temperature, dielectric state and microphysical properties such as roughness or size and shape. Active constituents at microwave frequencies are the water, ice and land surface of the Earth, the gases O_2 and H_2O of the atmosphere, and particles of various kinds, most notably cloud droplets and hydrometers.

For rainfall estimation purposes, microwave radiation is primarily characterized by intensity and polarization. The intensity is a linear function of temperature, and it is convenient to define a brightness temperature T_B such that

$$T_B = \varepsilon T \tag{1}$$

where ε is the emissivity as described in the previous section and T is the thermal temperature. Emissivity is a function of roughness of the surface, wavelength and angle of incident radiation.

At a point in space the electric field vector of an electromagnetic wave will trace an ellipse. Polarization describes the eccentricity and orientation of this ellipse and the direction the vector rotates. Circular polarization and linear polarization are the two components of the ellipse: together they determine its shape, orientation and direction. In microwave radiometry polarization ordinarily refers to the linear aspect. Often it is measured by the difference in brightness temperature between the horizontal and vertical

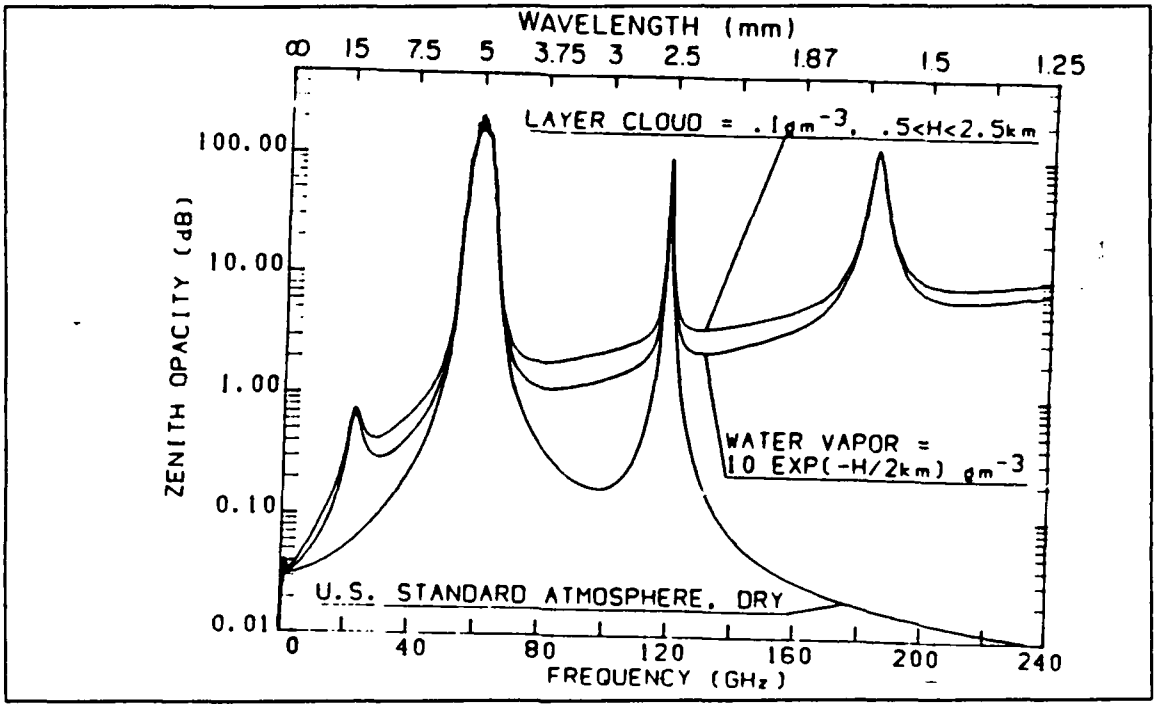

Fig. 1. Zenith opacity of the atmosphere as a function of frequency. (after Rosenkranz, 1978).

components of intensity, i.e. $T_{Bh} - T_{Bv}$, with vertical being defined as the normal to the surface.

The polarization of reflected, transmitted and emitted microwave radiation depends on molecular properties and the surface roughness of the medium. Like emissivity, it is a function of angle of view. Water surfaces such as the ocean produce highly polarized light at oblique viewing angles. Radiation emitted by atmospheric gases is not polarized; neither is there significant polarization in radiation emitted and scattered by cloud droplets and raindrops. Differences in polarization are a primary basis for distinguishing areas of rain over land and ocean.

2. Passive Microwave Measurement of Precipitation

Passive microwave rainfall estimates are usually based on either microwave absorption or scattering. In the former, rainfall is observed through the emission of thermal energy. A cold background is required in order to make such observations. Therefore, passive microwave rainfall estimates are only practical when viewing over the oceans. The liquid raindrops themselves are the dominant contributors to absorption

and emission, providing a direct physical relationship between the rainfall and the observed microwave radiances. In the case of scattering, the rainfall is estimated via the scattering within the rain column, which reflects the cold cosmic background towards the satellite. This process allows the observation of rainfall over any background, but since the scattering is primarily from the frozen hydrometeors aloft rather than from the raindrops, the relationship to rain rate is less direct than in the emission absorption regime. Generally, at frequencies below the 22 GHz water vapor line, absorption is the dominant process, and at frequencies above the 60 GHz oxygen complex, scattering dominates. Between 22 and 60 GHz either can be dominant according to the specific situation. Measurements using a frequency near the 22 GHz resonance of the water molecule have been used successfully to estimate the total water in a column of the atmosphere and are made as part of remote sensing of other parameters from space to help correct for the effects of atmospheric attenuation. (Wilheit, 1986).

Passive microwave methods utilizing the absorption-dominated mode have utilized the fact that the rain has a higher brightness temperature than the ocean surface because raindrops emit at near unit emissivity while the ocean surface has a relatively low emissivity of about 0.5. The models usually assume horizontally uniform liquid rain layers which extend up to the freezing level and that any ice that exists above this is essentially transparent at the frequencies of interest (typically 19 and 37 GHz). The study of Wilheit et al. (1977) describes a model used in relating observed brightness temperatures to rain rates. The model calculated brightness temperature over the ocean for frequencies of 19.35 GHz and 37 GHz as a function of rain rate for five different freezing level assumptions. For all freezing levels, the brightness temperature increases rapidly as a function of rain rate to a maximum in the neighborhood of 20 mm hr. The model was verified by comparing spaceborne radiometric observations with ground-based radar and by comparing ground-based, upward-viewing observations with direct rain measurements. The results of the ground-based validation showed good agreement at both frequencies between the observations and the theory which suggests that the atmospheric assumptions in the model are essentially correct at least for the conditions observed. Unfortunately, these relationships between T_B and rain rate are nonlinear. Therefore, a low bias in the rain rate measurement results when light and heavy rain rates are present together within a footprint. Also, there is some ambiguity between emission that is due to rain and that which is due to nonprecipitating cloud water.

The Mie theory (Mie, 1908) can be used to quantify the scattering properties of hydrometeors. The most important precipitation variables affecting brightness temperature measurements at any given frequency are hydrometeor size, phase, number density and depth of layer. If the theory is used to address a Marshall-Palmer size distribution (Marshall and Palmer, 1948), the single scattering albedo increase dramatically as microwave frequency increases (Fig. 2). Single scatter albedo is derived from the scattering at a single point source, as opposed to multiple scattering (skylight). The high single scatter albedos produced by the ice are of great importance for the production of microwave radiances that contrast with the precipitation's surroundings. Since ice has much smaller absorption coefficients than water, it has high albedos at all SSM/I frequencies. A single scatter albedo approaching one indicates that thermal radiation at or below an ice layer is negligible compared to scattering produced by the ice. If the scattering coefficient is large enough (such as at 85.5 GHz), and if there are no significant sources of downwelling radiation from the overlying atmosphere to be scattered back toward the spaceborne radiometer, very low brightness temperatures can result.

In radiative transfer calculations, if the single scattering albedo is high, then greater scattering coefficients translate into stronger brightness temperature depressions. This is shown in Fig. 3, where the relationship between T_B and surface precipitation rate has been modeled over both land and ocean surfaces (Wu and Weiman, 1984). This model assumes Marshall-Palmer size distributions of ice water contents that decrease with height above the rain which then increases in depth and density as the rain rates increase. From this model T_B depressions range from tens of degrees at 18 GHz to almost two hundred degrees at 85.6 GHz. Because of the small size of many precipitating cells, this change in T_B can occur over distances on the order of 100 m. Thus, volume scattering by precipitation is an impressive geophysical passive signature in the microwave spectrum.

Spencer (1986) introduced a scattering-based method for quantitatively measuring rainfall over the ocean from Nimbus-7 Scanning Multichannel Microwave Radiometer (SMMR) 37 GHz observations. This proves to be a considerable simplification at this frequency because only precipitation-size hydrometeors will cause scattering. Thus, there is no ambiguity concerning the effects of cloud water. Both horizontally (H) and vertically (V) polarized radiances are utilized which allow the discrimination between low T_B that are due to ocean emitted radiation (highly polarized) and low T_B that are due to precipitation (slightly polarized). "Polarized" here refers to the difference between the horizontally and vertically polarized T_B.

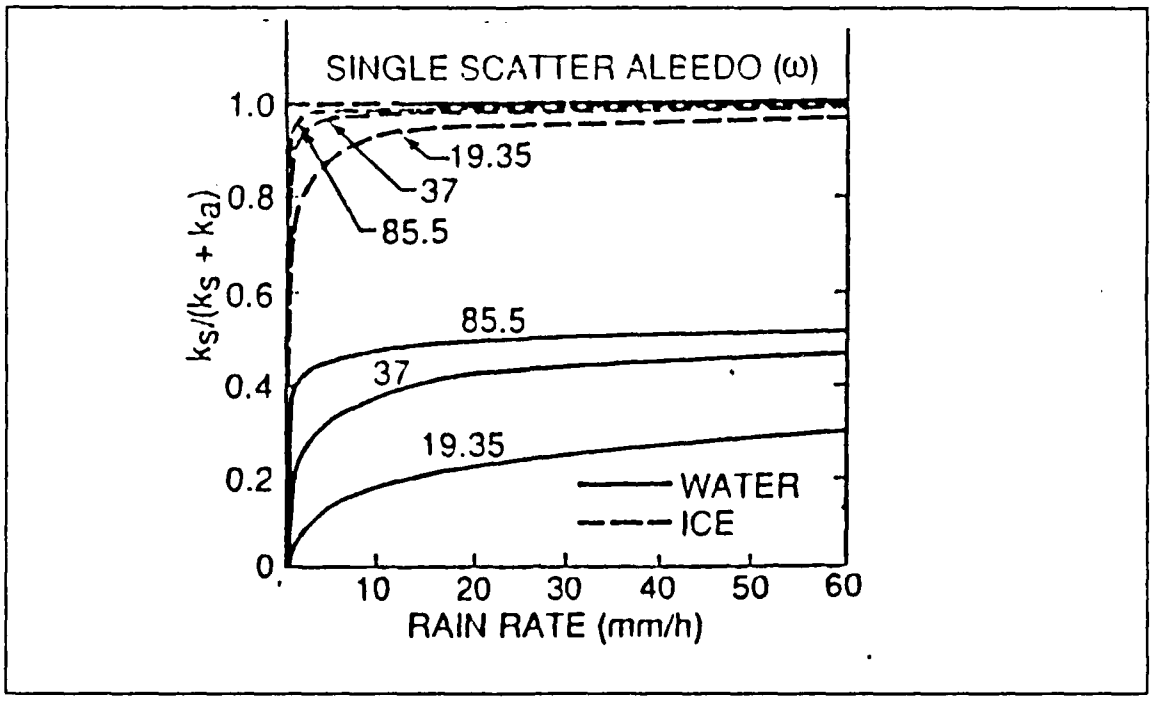

Fig. 2. Mie single scattering albedos vs. rain rate as a function of frequency (after Spencer et al., 1988).

Spencer's technique uses the observed scattering effects of precipitation on 37 GHz brightness temperatures in the oceanic environment. The technique requires an estimate of the effective radiating temperature of the cloudy portion of the atmosphere and a T_B measurement of the cloud-free ocean surface. These two measurements bound all possible combinations of clear and cloudy conditions within a footprint in terms of bipolarized brightness temperature. Because the technique involves a linear transformation between dual polarized brightness temperature and rain rate, there are no non-linear "footprint filling" effects and a unique footprint-averaged rain rate results. The results show that these SMMR-derived rain rates for five cases of convection over the Gulf of Mexico are closely related to simultaneously derived radar rain rates, having a correlation of 0.90. A similar technique using 37 GHz brightness temperatures is included in a precipitation method evaluated in this thesis. See the following chapter for details concerning this rain estimation scheme.

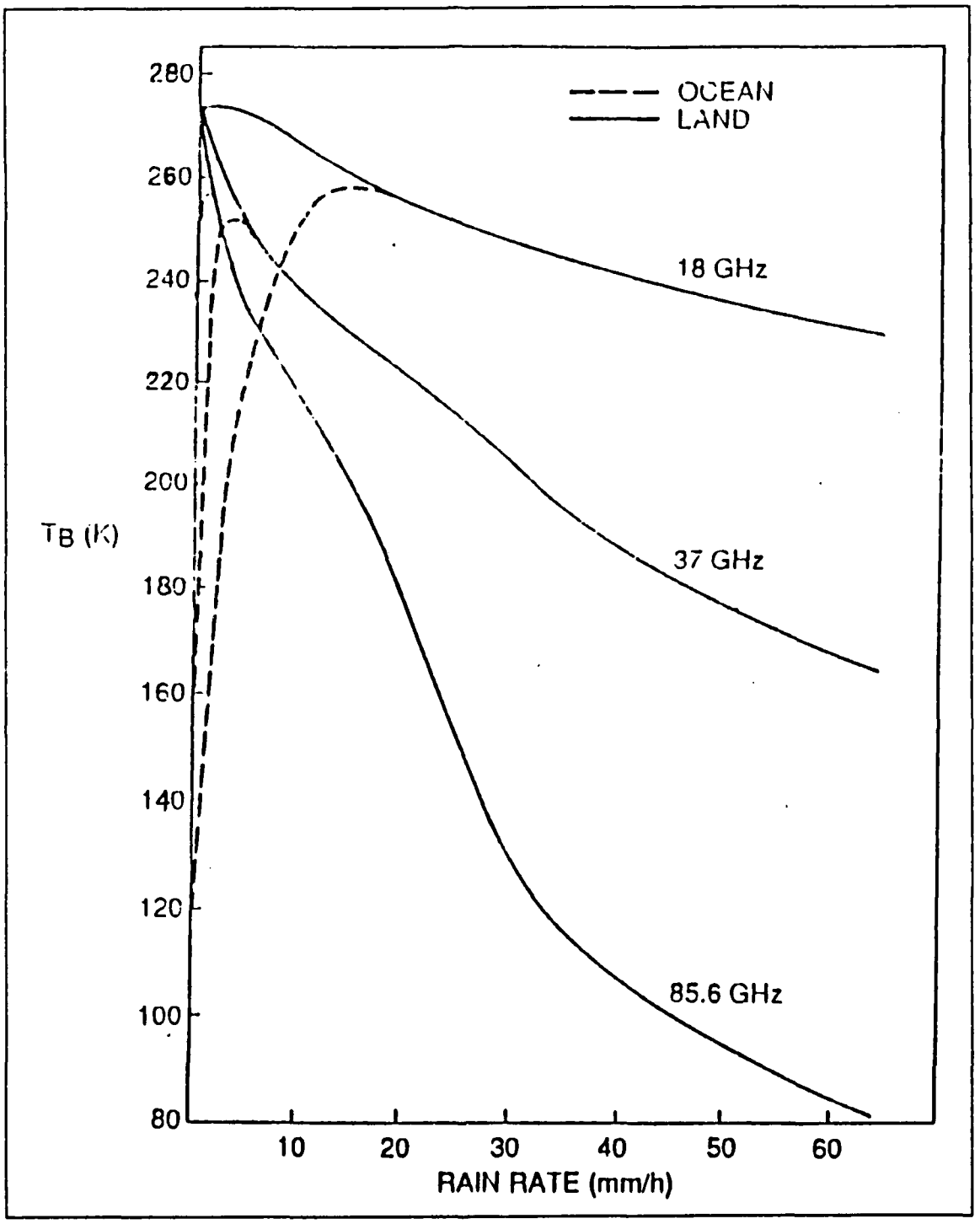

Fig. 3. Brightness temperature - rain rate relationships at 18, 37, and 85.6 GHz from model of Wu and Weinman (1984).

The above satellite studies were limited to a highest frequency of 37 GHz. The June 1987 launch of the first SSM I on a DMSP F8 satellite has resulted in a significantly improved precipitation monitoring capability from space. This instrument extends the spaceborne observational frequency capability to 85.5 GHz. Additional information concerning the instrumentation of the SSM I is presented in Chapter 3.

Spencer et al. (1988) identifies a method for retrieval of precipitation estimation over both warm and cold land, and ocean environments, from dual polarized 85.5 GHz scattering inferences. The study demonstrates that the polarization diversity available at 85.5 GHz from the SSM I allows discrimination between low brightness temperatures due to surface water bodies versus those due to precipitation. This scheme is used to analyze precipitation associated with the developing cyclone evaluated in this thesis. Details of this method are provided in the next chapter.

III. RAINFALL ANALYSIS TECHNIQUES

A. NPS CLOUD AND PRECIPITATION ANALYSIS MODEL

The Naval Postgraduate School (NPS) automated cloud and precipitation model produces analyses of important cloud and precipitation parameters including cloud amount, cloud type, cloud-top temperature, cloud-top height and precipitation intensity. The model was developed by Nelson (1982) who utilized Harris and Barrett's (1978) cloud amount estimate techniques, Liljas' (1982) cloud and precipitation intensity threshold method and Reynolds and Vonder Haar's (1977) bispectral cloud-top temperature scheme. The summary that follows is condensed from Wash et al. (1985).

The model uses digital satellite data from the visual and infrared channels from the GOES Visual-Infrared Spin Scan Radiometer (VISSR) or the NOAA Advanced Very High Resolution Radiometer (AVHRR). The model performs a movable window analysis anywhere within the satellite area coverage for a 512 x 512 grid array.

The model is composed of three main processors: (1) data input, (2) basic satellite and statistical calculations and (3) cloud and precipitation computations. Satellite calculations include conversion of infrared data counts to infrared temperatures using the GOES sensor conversion table (Clark, 1983) and visual data counts to albedos using the brightness normalizations scheme of Muench and Keegan (1979), to correct for sun angle and anisotropy. These infrared temperatures and albedos are used in the model instead of the raw GOES sensor counts. The calibration of AVHRR data is described by Brown et al. (1985) and Lauritson et al. (1979). Temperature-pressure soundings are obtained from the Fleet Numerical Oceanography Center (FNOC) for the center point of sixteen subsections of the infrared image.

Further processing of the visual data results in an average brightness and its standard deviation for each grid point. The average visual brightness value and corresponding infrared temperature, together with brightness standard deviation, are used to produce the cloud and precipitation analyses.

The bispectral classification uses infrared temperatures, visual albedos, and in some cases visible standard deviation values, to discriminate cloud type. The average visible brightness values and infrared temperatures are used in a series of threshold tests following Liljas (1982) in determining a particular cloud type (Fig. 4). In the case of discriminating between stratus and cumulus, stratocumulus and cumulus, and altostratus

and cumulus congestus, a texture test is conducted with the brightness standard deviation. Harris and Barrett (1978) performed a linear discriminant analysis using standard deviation values and vector dispersion to separate cumuliform and stratiform clouds. If the standard deviation is greater than the threshold value 0.05, then the cloud type is cumuliform due to the variation in albedo values. A standard deviation less than 0.05 results in a stratiform cloud type classification. A typical brightness standard deviation range for stratiform clouds is between 0.01 and 0.04.

The precipitation estimation follows Liljas' (1982) threshold technique, adopted from the results of Muench and Keegan (1979). The technique relates the cloud type information to precipitation areas. If the resulting cloud type is nimbostratus or cumulonimbus, the precipitation thresholds are activated. Three categories of intensity (light, moderate, or heavy) can result, depending upon the infrared temperature and visual albedo (Fig. 5).

The study of Wash et al. (1985) evaluated the model's performance by verifying five cases of GOES-East data over the eastern United States and western North Atlantic Ocean. Reasonable results were obtained from synoptic subjective evaluations performed on each case. The majority of cloud and precipitation analyses correctly characterized the mesoscale cloud and weather features. Less successful results were obtained from the single station-satellite data comparison used on the cloud type and precipitation parameters.

Most cloud types were analyzed correctly after modifications to the model were made based on an evaluation by Moren (1984). Nimbostratus was classified correctly 54 % of the time. Most nimbostratus classification errors were due to nimbostratus altostratus boundaries located near the verification station; surface observations of nimbostratus were classified as altostratus by the model.

The majority of precipitation analyses were successful, especially for multi-layered and nimbostratus clouds. 93 % of the surface reports of fair skies and 67 % of the precipitation reports were analyzed correctly by the model. Less successful results occurred in conjunction with cumulonimbus clouds.

The study of Spray (1985) evaluated the performance of the model for several 1985 winter and spring days. The evaluation found that the model produced fair analyses of precipitation distribution, although often the intensity was underestimated. The study of Pind (1987) focused on precipitation along the west coast of the United States and found that the model overestimated the areal coverage of the observed precipitation.

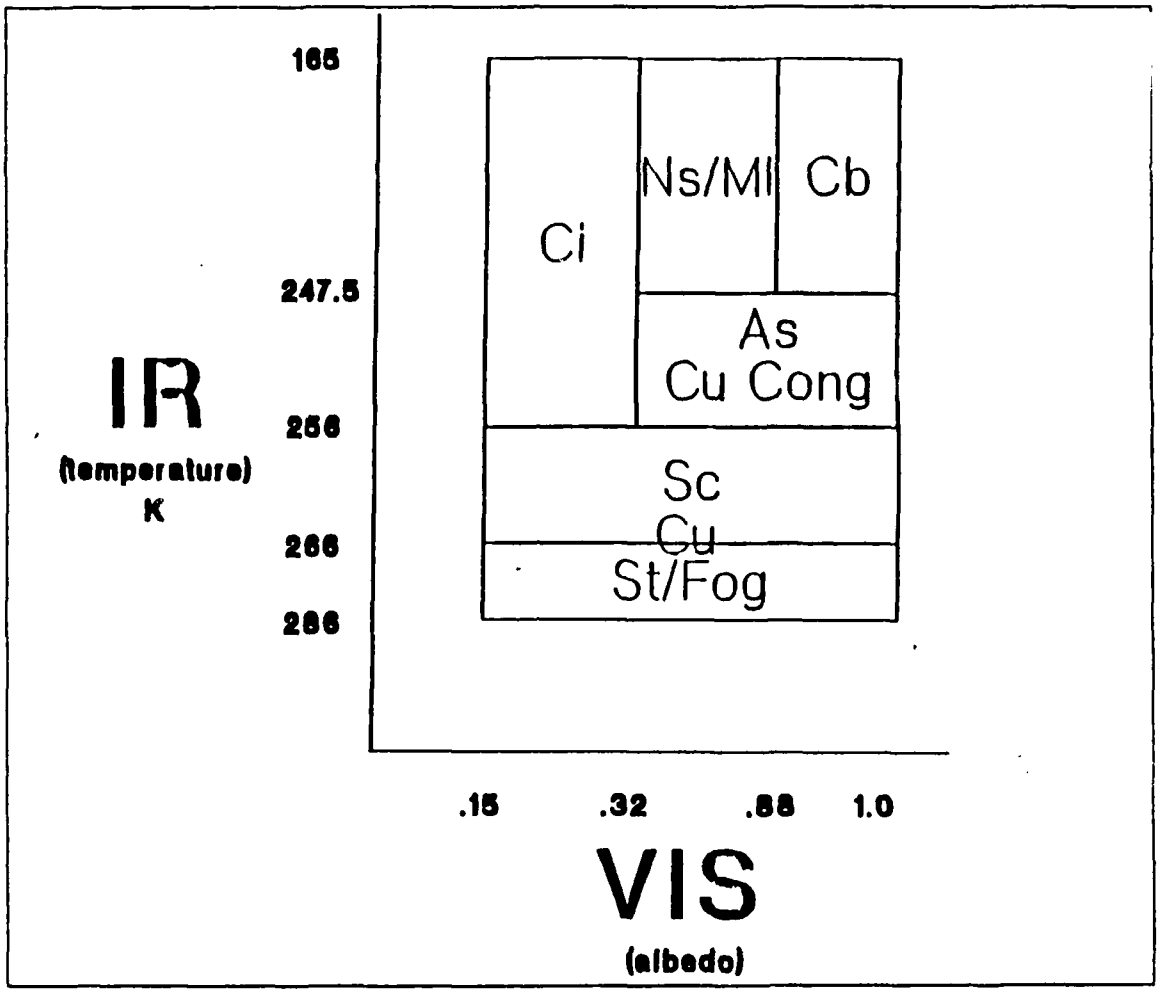

Fig. 4. Two-dimensional cloud typing graph using GOES IR and VIS satellite digital data. (after Spray, 1985).

B. PRECIPITATION ANALYSIS USING THE SSM/I

The SSM/I is a joint Navy/Air Force passive microwave radiometric system developed by the Hughes Aircraft Company (HAC) under the direction of the Navy Space Systems Activity (NSSA) and the Air Force Space Division. It is flown on the DMSP operational spacecraft as an all weather oceanographic and meterological sensor. The material presented in this section is condensed from Hollinger et al. (1987) and Spencer et al. (1988).

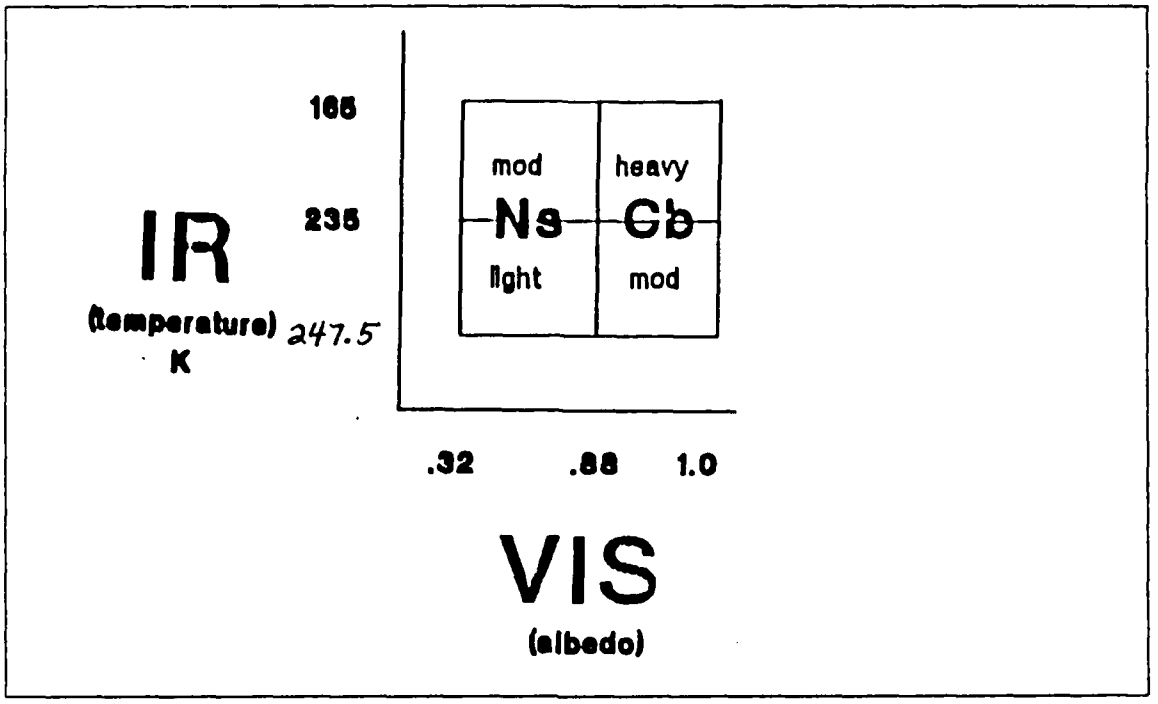

Fig. 5. Two-dimensional precipitation histogram using GOES IR and VIS digital satellite data. (after Spray, 1985).

1. Instrument Description

The SSM/I is a seven channel, four frequency, meteorological and oceanographic sensor. The instrument measures atmospheric/surface brightness temperatures at 19.3, 22.2, 37.0 and 85.5 GHz, all dual polarized (vertical and horizontal) except for 22 GHz. In addition to the SSM/I's channel uniqueness, its swath width is nearly twice that of its forerunner, the Nimbus-7 SSMR. The need for polarization correction due to antenna rotation is eliminated by the synchronous rotation of the feedhorn with the antenna.

The SSM/I rotates in a circular scan with a period of 1.9 seconds, during which time the satellite advances 12.5 km. Fig. 6 depicts the details of its scan geometry. The angle between satellite nadir and the antenna beam is a constant 45° . Thus, as the antenna rotates, the beams define the surface of a cone and, from the orbital altitude of 833 km, make a constant zenith angle of 53.1° . Earth atmosphere sensor data are collected over 102° of each rotation. This angle is centered on the satellite subtrack aft of the satellite and results in an Earth swath width of 1394 km. During the remaining

258° of each rotation, short bursts of calibration readings from hot and cold calibration sources are taken. The radiometer outputs are sampled differently on alternate scans. Scans are labeled as "A" and "B." Each A scan contains 64 sets of concentric measurements by all seven channels and 64 sets of concentric measurements by the two 85 GHz channels taken midway between each of the all-frequency scene stations. Each B scan contains 128 sets of concentric measurements by the two 85 GHz channels. The instrument measures the emitted energy with spatial resolution of 12.5 km at 85 GHz and 25 km at the three lower frequencies.

2. HAC Precipitation Retrieval

The rain rate estimation developed by HAC utilizes both the emission and scattering modes to estimate precipitation based on the observed brightness temperatures from the SSM I channels. The algorithm for extracting precipitation over the ocean use the brightness temperatures as independent variables in linear regression equations. The regression coefficients are determined using the climatology, geophysical models, radiative transfer models and an inversion algorithm. Eleven climates are defined for the environmental parameter retrieval (Table 1), for both land and the ocean cases.

The formula first checks for certain rain thresholds. The criteria given for ocean cases are the critical temperature of the 19H brightness temperature for the 'maybe rain' case CMRO, and the critical brightness temperature difference between the two polarizations of the 37 GHz frequency for 'maybe rain', CMRDO (Table 2). When either of the two criteria is met, i.e., when T_B (19H) is greater than CMRO or when T_B (37V) - T_B (37H) is less than CMRDO, the algorithm assumes that there is rain. The criterion for 'heavy rain' over the ocean, CHRDO, is also based on the difference in T_B between the two 37 GHz channels. When T_B (37V) - T_B (37H) is less than CHRDO, the 'heavy rain' condition is assumed. The algorithm criteria are listed in Table 2 for the eleven climates.

When rain is assumed from the criteria, rain rate (RO) is calculated by the following algorithm,

$$RO = C_{ro,o} + C_{ro,1}T_b(19H) + C_{ro,2}T_b(22V) + C_{ro,3}T_b(37V) + C_{ro,4}T_b(37H) \qquad (2)$$

The 22V brightness temperature is included due to the relatively high water vapor contamination at that frequency. The regression coefficients for all climate zones are listed in Table 3. Three categories of rain rate intensity will be used to compare with the NPS

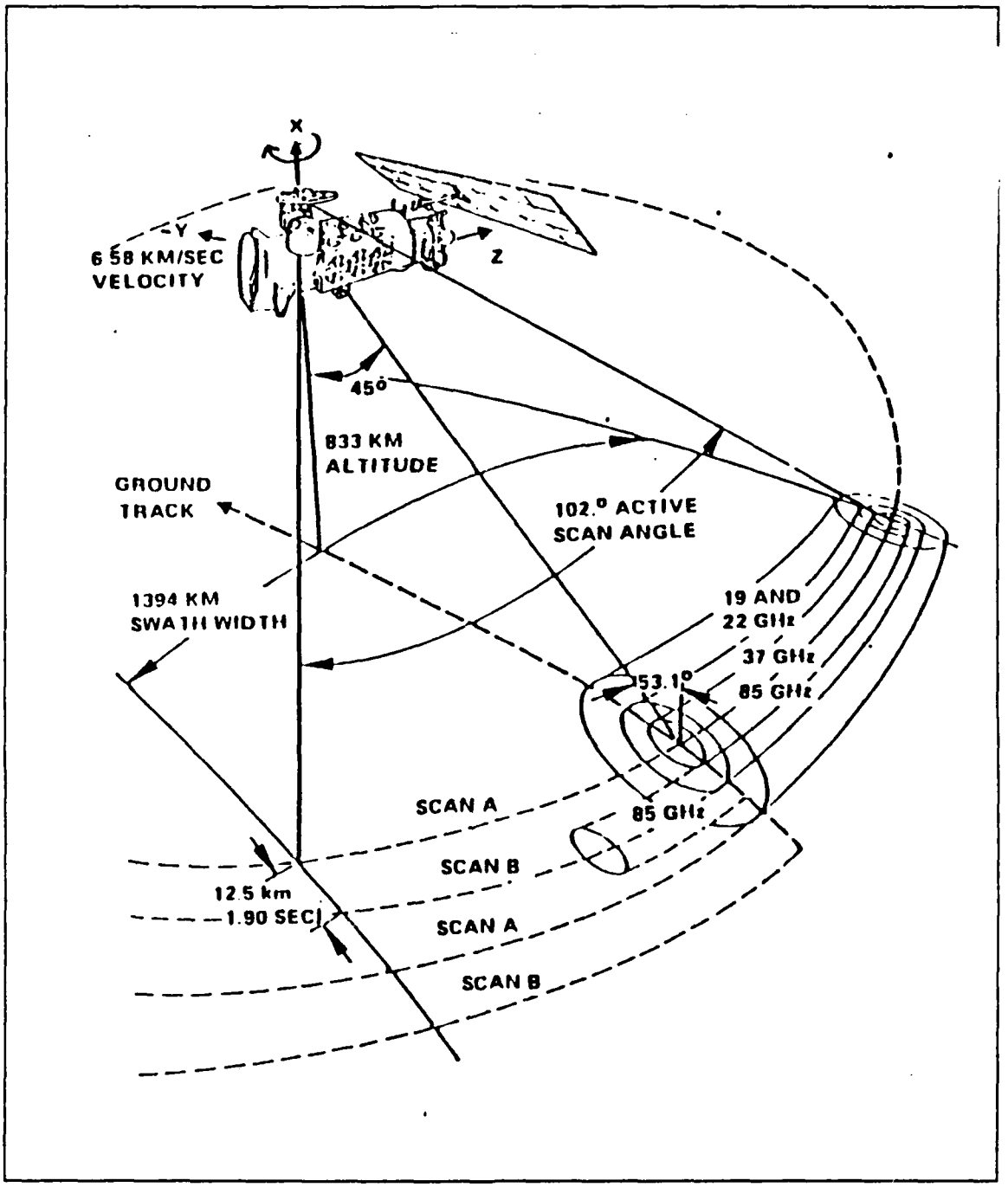

Fig. 6. SSM/I Scan Geometry. (after Hollinger et al., 1987).

Table 1. DEFINITION OF HAC CLIMATE CODES. (AFTER HOLLINGER ET AL., 1987).

Climate Code No.	Definition
1	Tropical-warm
2	Tropical-cool
3	Lower Latitude Transition-warm
4	Lower Latitude Transition-cool
5	Mid. Lat.-Spring/Fall
6	Mid. Lat.-Summer
7	Mid. Lat.-Winter
8	Upper Lat. Transition-cool
9	Upper Lat. Transition-cold
10	Polar-cool
11	Polar-cold

technique and are defined as follows: light (1-3 mm/hr), moderate (4-12 mm/hr) and heavy (> 13 mm/hr). These values are derived from NOAA's Radar Guidance Program for stratiform rain.

3. Scattering-based Precipitation Method

The precipitation scheme in the study of Spencer et al. (1988) utilizes the SSM/I's polarization diversity at 85 GHz to allow discrimmination between highly polarized radiances of the ocean from essentially unpolarized radiances from precipitation volume scattering. Because the polarization correction for water surfaces is best illustrated with non-precipitating clouds of varying opacity, the method addresses the effects of surface water and non-precipitating clouds together. With this in mind, a polarization corrected temperature (PCT) is formulated as follows:

$$PCT = (\beta T_{Bh} - T_{Bv})/(\beta - 1), \tag{3}$$

where

$$\beta = (T_{Bvc} - T_{Bvo})/(T_{Bhc} - T_{Bho}). \tag{4}$$

Table 2. RAIN CRITERIA FOR THE HAC ALGORITHM (AFTER HOLLINGER ET AL., 1987).

Climate Code	CMRO	CMRDO	CHRDO	CFGL	CHRL	CHRDL	CMRL	CMRDL
1	190	25	10	150	273	10	263	5
2	190	25	10	150	273	10	263	5
3	190	25	10	150	273	10	263	5
4	190	25	10	150	273	10	263	5
5	170	25	20	240	270	10	240	--
6	190	25	15	150	270	10	263	5
7	160	30	20	240	270	10	240	--
8	150	35	20	240	270	10	240	--
9	140	35	20	270	270	--	270	--
10	150	35	20	240	270	10	240	--
11	140	35	20	270	270	--	270	--

CMRO = Criterion for maybe rain over ocean for $T_B(19H)$

CMRDO = Criterion for maybe rain over ocean for $T_B(37V) - T_B(37H)$

CHRDO = Criterion for heavy rain over ocean for $T_B(37V) - T_B(37H)$

CFGL = Criterion for frozen ground for $T_B(37V)$

CHRL = Criterion for heavy rain over land for $T_B(37V)$

CHRDL = Criterion for heavy rain over land for $T_B(37V) - T_B(37H)$

CMRL = Criterion for maybe rain over land for $T_B(37V)$

CMRDL = Criterion for maybe rain over land for $T_B(37V) - T_B(37H)$

Here, T_{Bhc} and T_{Bvc} refer to the horizontally and vertically polarized cloudless ocean T_B, respectively, while T_{Bh} and T_{Bv} are horizontally and vertically polarized T_B that are at least partially affected by any combination of clouds and precipitation. T_{Bvc} and T_{Bhc} are the vertically and horizontally polarized T_B, respectively, of the ocean with no overlying atmosphere. β is the ratio of T_{Bv} warming to T_{Bh} warming resulting from only atmospheric gaseous absorption (primarily water vapor and oxygen). Spencer et al. found that $\beta = 0.45$ gives an empirically realistic PCT range of 275° K to 290° K. With $\beta = 0.45$, the PCT formula becomes

$$PCT = 1.818T_{Bv} - 0.818T_{Bh} \tag{5}$$

Cloud water causes brightness temperatures to decrease as the cloud water content or cloud thickness increases. Spencer et al. suggested a tentative threshold of 255° K for the delineation of precipitation, with a corresponding rain rate threshold of

Table 3. PRECIPITATION OVER OCEAN COEFFICIENTS FOR ALL CLIMATES. (AFTER HOLLINGER ET AL., 1987).

Climate code	$C_{ro,o}$	$C_{ro,1}$	$C_{ro,2}$	$C_{ro,3}$	$C_{ro,4}$
1	210.2800	.1217	-.7829	-.1830	.0998
2	215.1800	.1026	-.8059	-.1944	.1354
3	173.0400	.1938	-.6500	-.2291	.0808
4	169.2900	.1523	-.6065	-.3531	.2162
5	123.4000	.2019	-.4070	-.5117	.2969
6	135.8000	.2659	-.5170	-.2751	.0618
7	114.5500	.2708	-.6228	-.2836	.2521
8	9.5432	.1796	-.2109	.1214	-.0753
9	24.1020	.0825	.1367	-.3411	.0843
10	9.5432	.1796	-.2109	.1214	-.0753
11	24.1020	.0825	.1367	-.3411	.0843.

approximately 1-3 mm/hr. These values were based upon the theroretically expected T_B depressions from warm season non-precipitating cloud alone, the modeled effects of light precipitation, the observed relationship between aircraft radiometer and ground-based research radar measurements of a warm season thunderstorm complex, and comparisons between SSM/I radiances and simultaneous radar measurements for several storms. This thesis will utilize both the HAC retrieval and the PCT method in analyzing precipitation from a developing winter season cyclone.

IV. RESULTS

A. SYNOPTIC DESCRIPTION

This study investigates the precipitation associated with a cyclone that moved rapidly across the eastern North Pacific Ocean. The surface low positions with central pressures are presented in Fig. 7. A graph of the cyclone's central pressure with time (Fig. 8) shows a rapid deepening of 20 mb from 1800 UTC 16 January to 1200 UTC 17 January 1988. At 1800 UTC 16 January 1988, a 1008 mb low develops near 36° N 139° W as a frontal wave spreads clouds across much of the eastern North Pacific Ocean (Fig. 9). An upper level trough just west of the low can be identified by a comma cloud and indicates that deepening of the surface low is likely. By 0000 UTC 17 January, the low deepens to 1004 mb and moves east to 37° N 133° W (Fig. 10). Clouds and precipitation develop in the warm sector ahead of the low. At 1200 UTC 17 January, the upper level trough moves vertically over the surface low as it reaches peak intensity of 988 mb. The frontal cloud band wraps around the northern sector of the surface low and cold air advances behind the cold front, as shown by the outbreak of convective cloudiness (Fig. 11).

B. GOES IMAGERY AND NPS PRECIPITATION MODEL ANALYSES

The digitized GOES-West sectors presented in this section are produced using a movable grid for a 512 x 512 array with a 2 x 2 n mi visual (2 x 4 n mi infrared) resolution. Cloud and precipitation fields approximately cover a 1200 x 1200 n mi area. The GOES image (IR only) at 1516 UTC 16 January 1988 is shown in Fig. 12. A broad shield of middle to high level clouds between 35° and 40° N is evident ahead of the surface wave developing near 36° N 143° W. The clouds associated with a separate system to the north are merging with the surface wave. Another separate feature is the comma cloud centered near 39° N 147° W, also producing mostly upper-level clouds. Lower-level clouds form near the wave itself and extend southwest along the weak cold front.

GOES imagery at 1816 UTC shows a clearer view of the streaky cirrus bands that are probably associated with the jet stream. The visual data (Fig. 13) better depicts the western comma cloud as a separate feature. The infrared picture (Fig. 14) has the cold front still mostly composed of low clouds, but the visual image shows a distinct "rope" cloud associated with it.

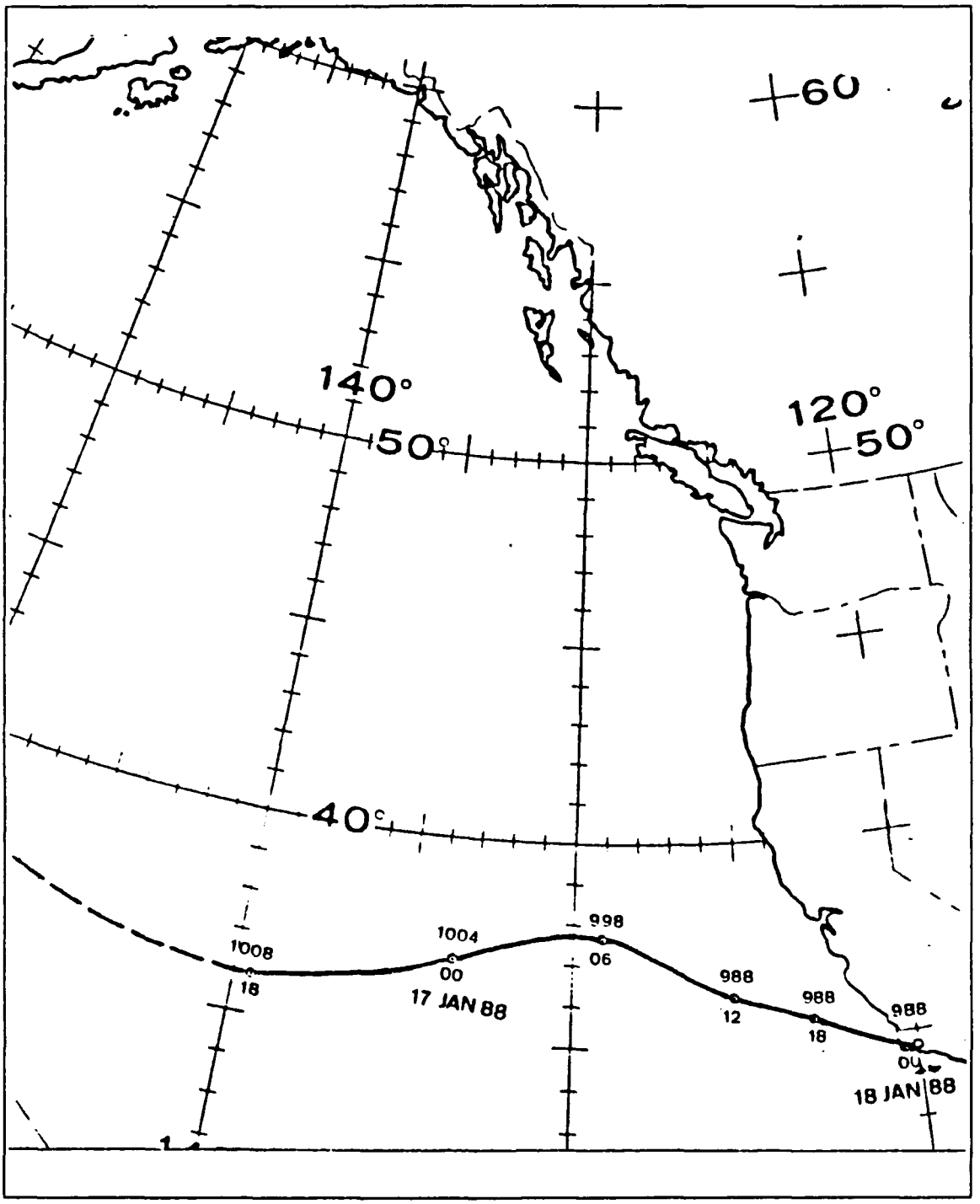

Fig. 7. Track of surface cyclone across the eastern North Pacific Ocean 16-18 January 1988 (after Atangan, 1988).

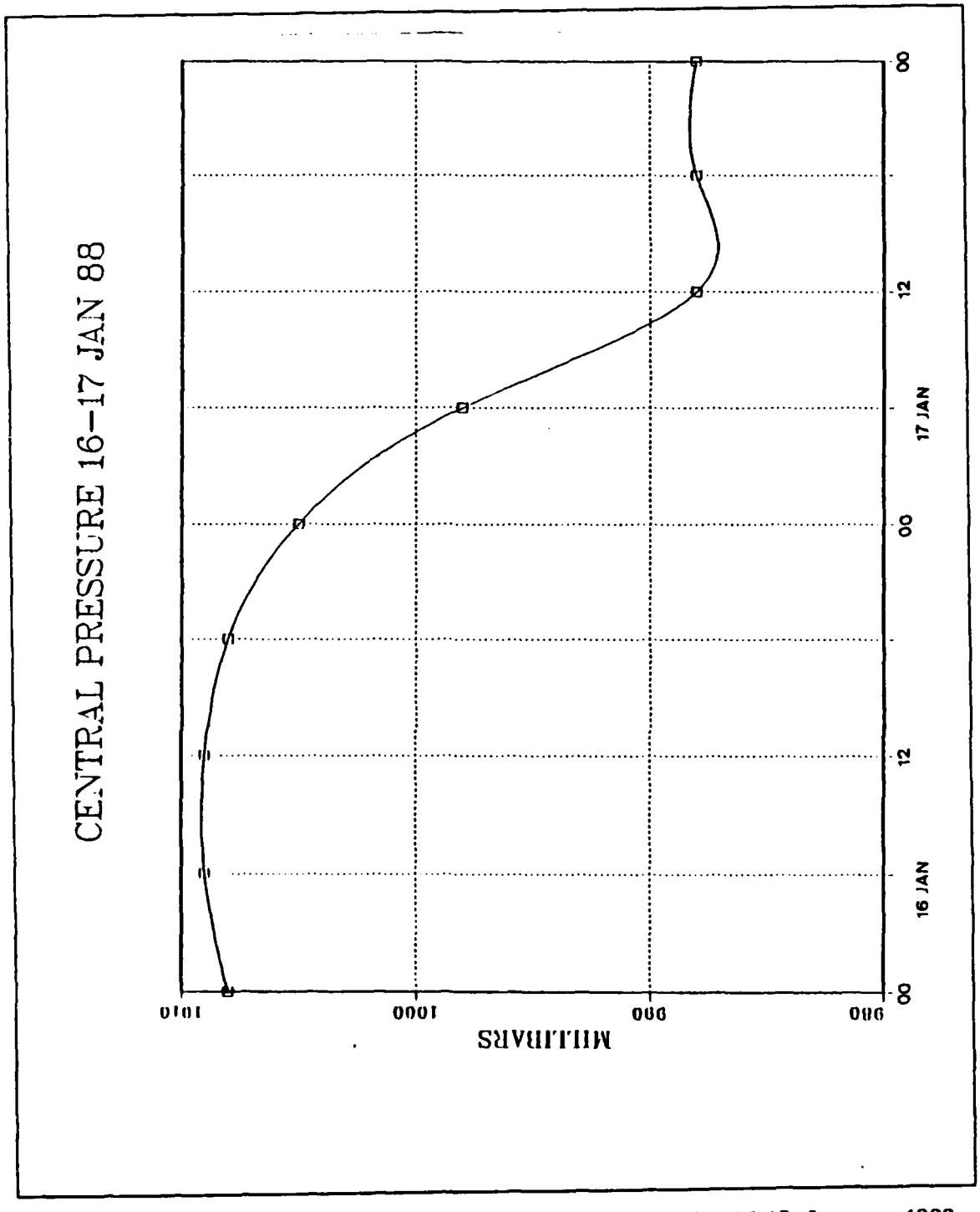

Fig. 8. **Time change of minimum central pressure for the 16-18 January 1988 cyclone (after Atangan, 1988).**

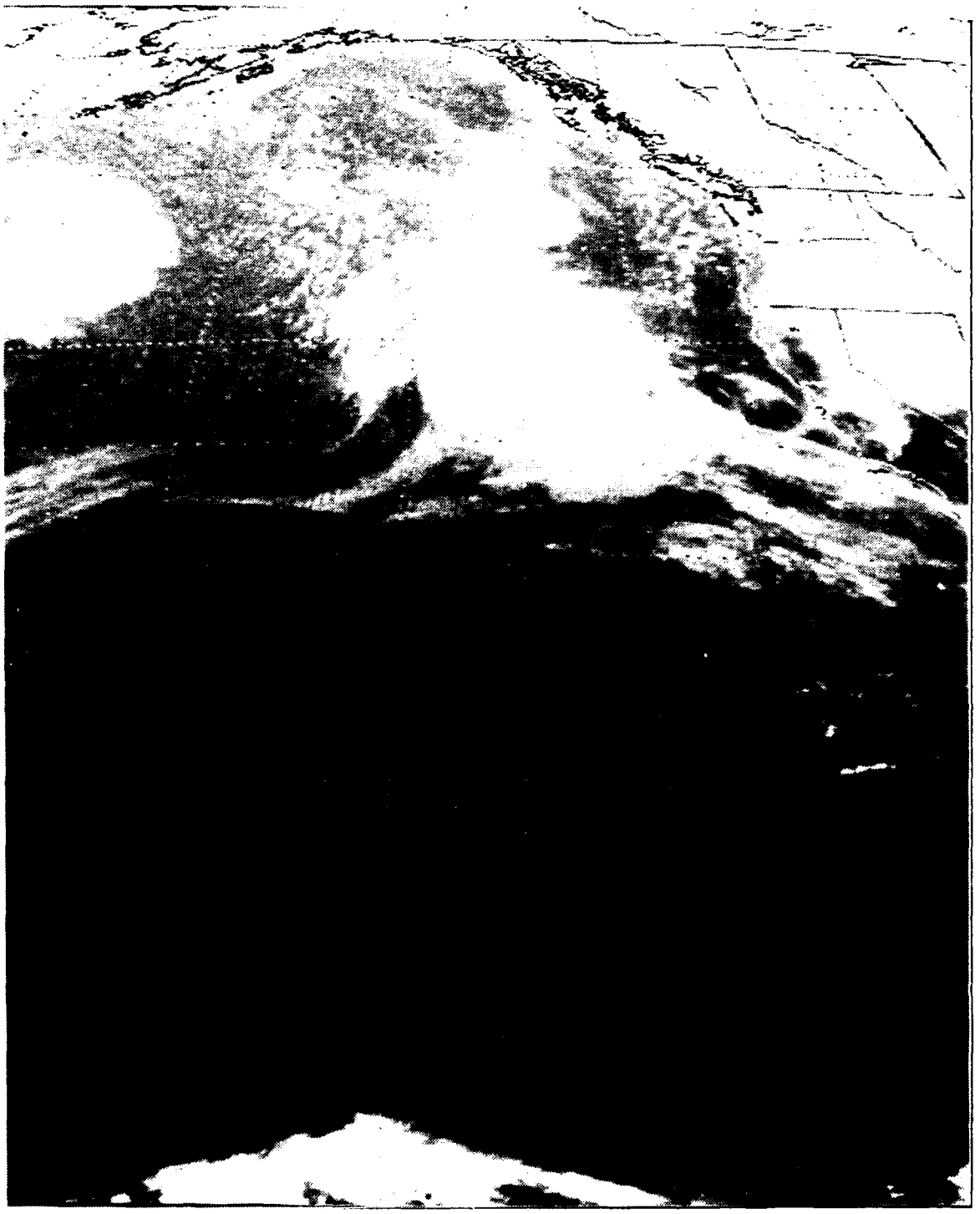

Fig. 9. GOES infrared image at 1800 UTC 16 January 1988.

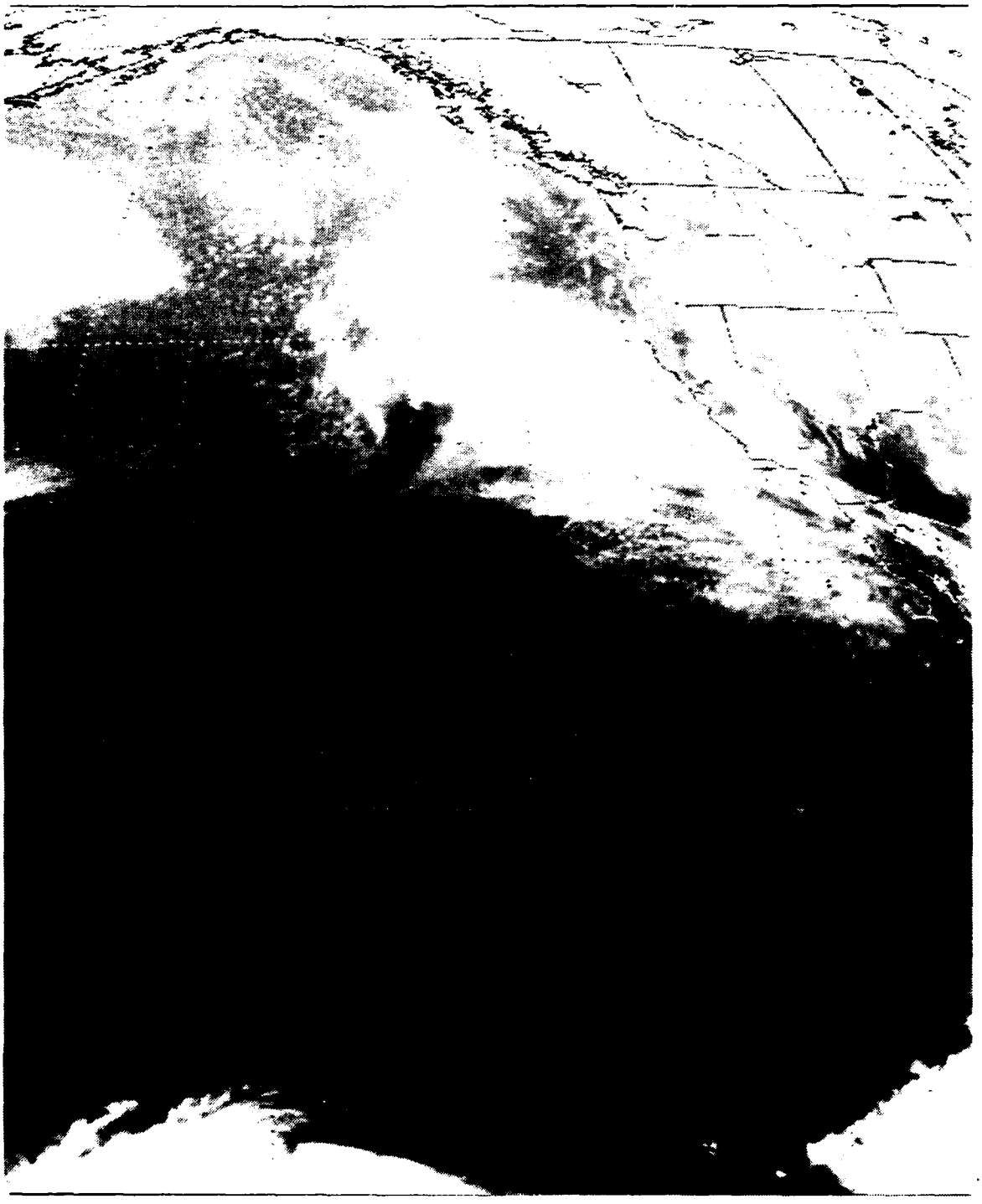

Fig. 10. GOES infrared image at 0000 UTC 17 January 1988.

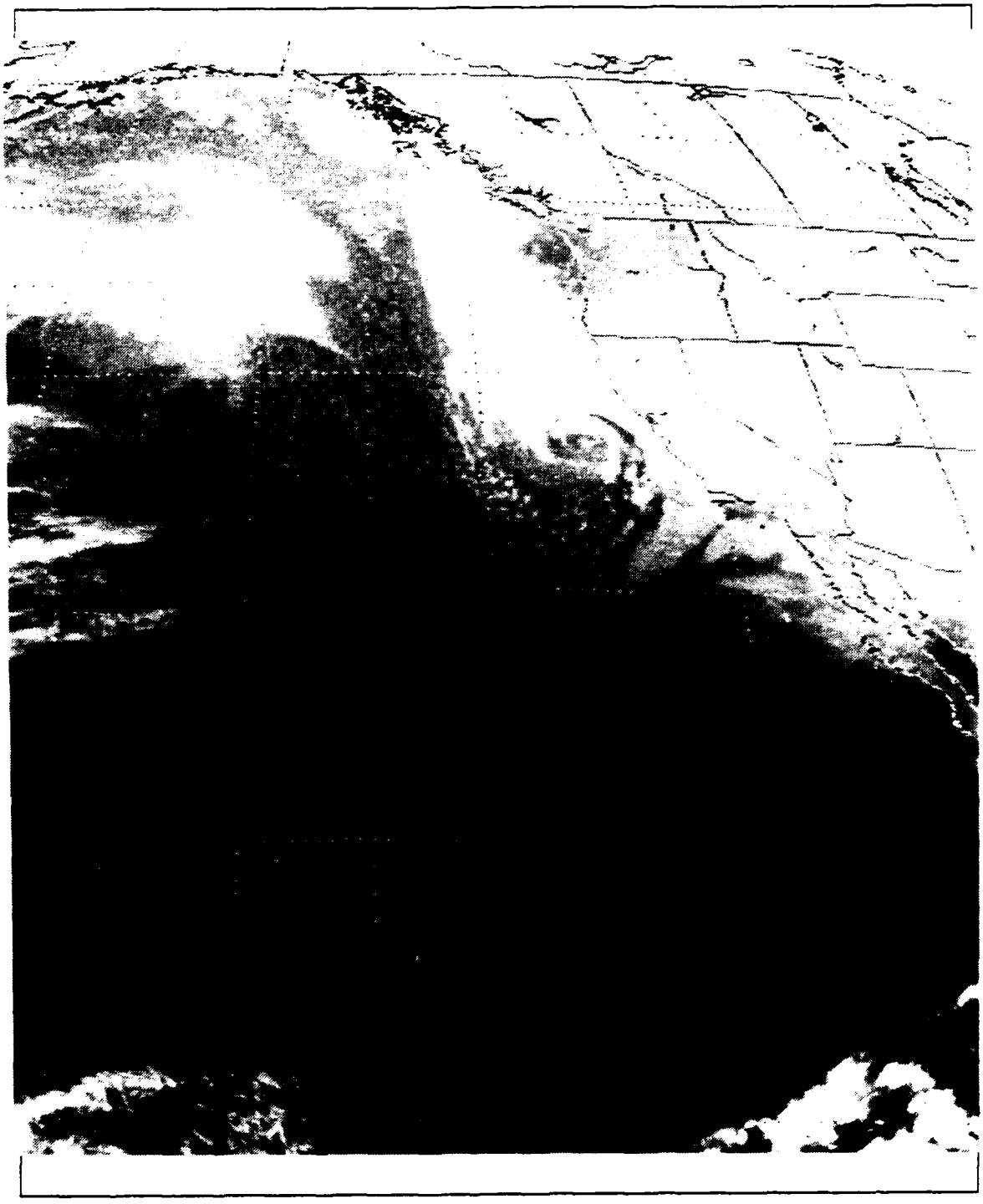

Fig. 11. GOES infrared image at 1200 UTC 17 January 1988.

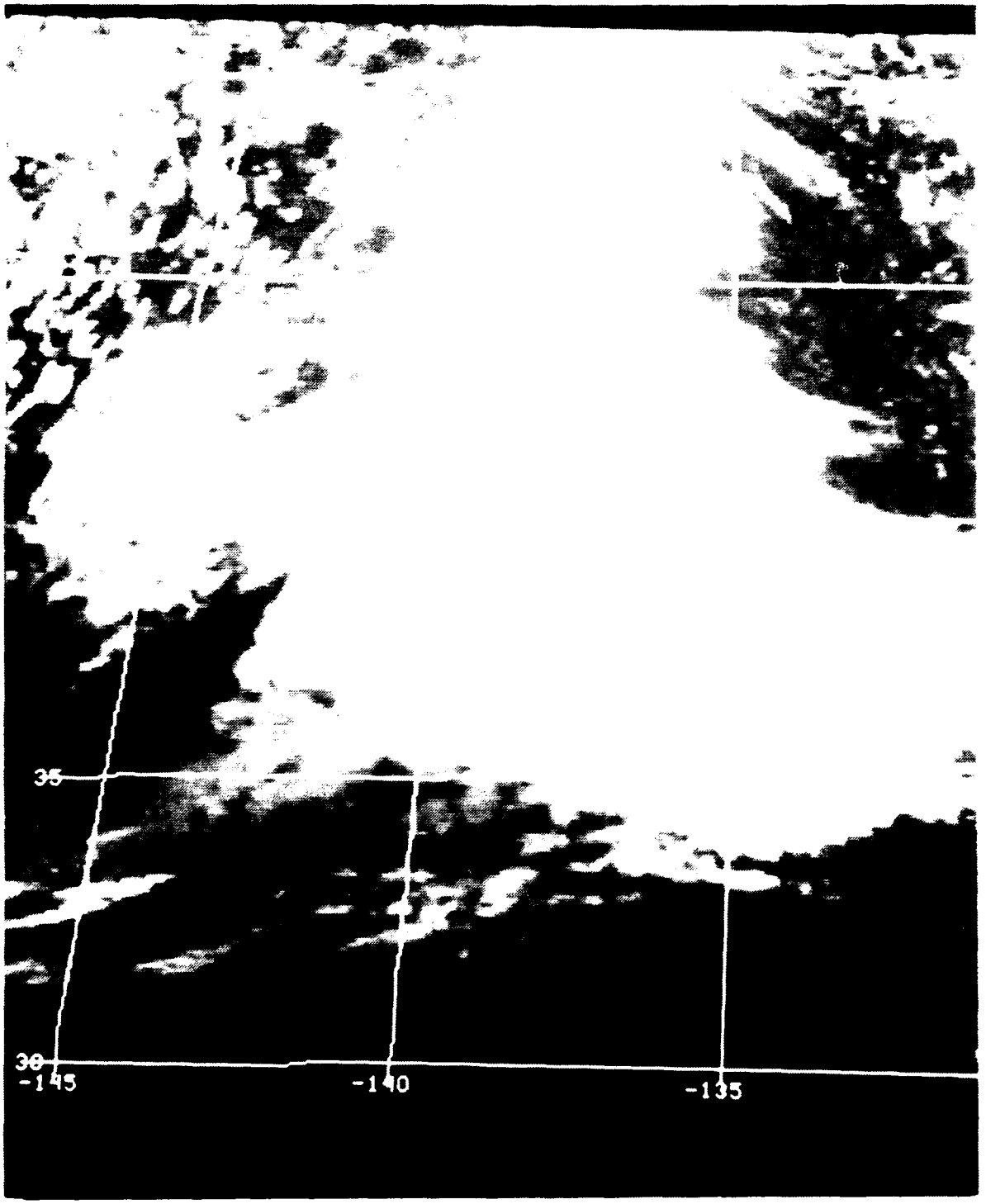

Fig. 12. GOES infrared image at 1516 UTC 16 January 1988.

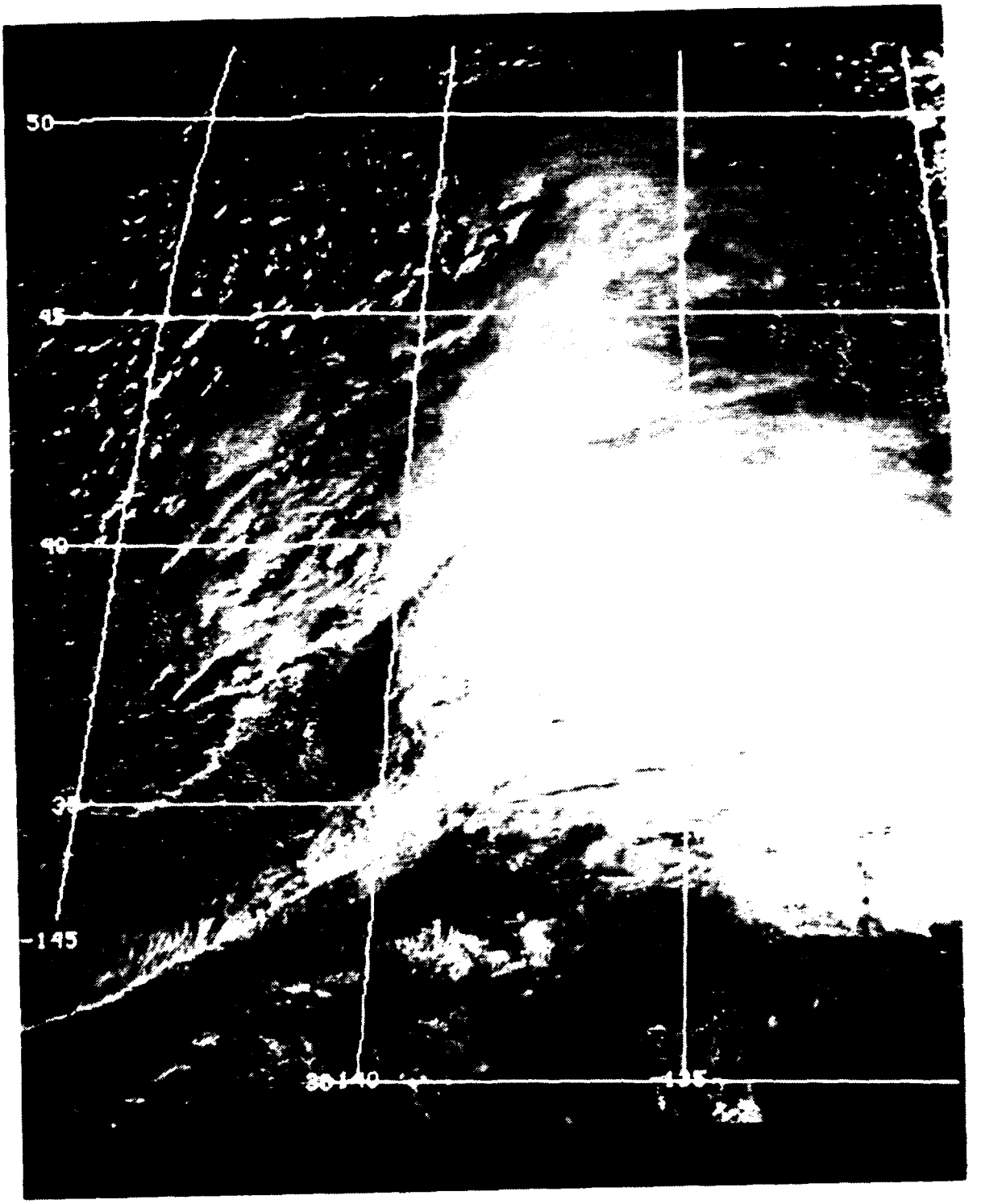

Fig. 13. GOES visual image at 1816 UTC 16 January 1988.

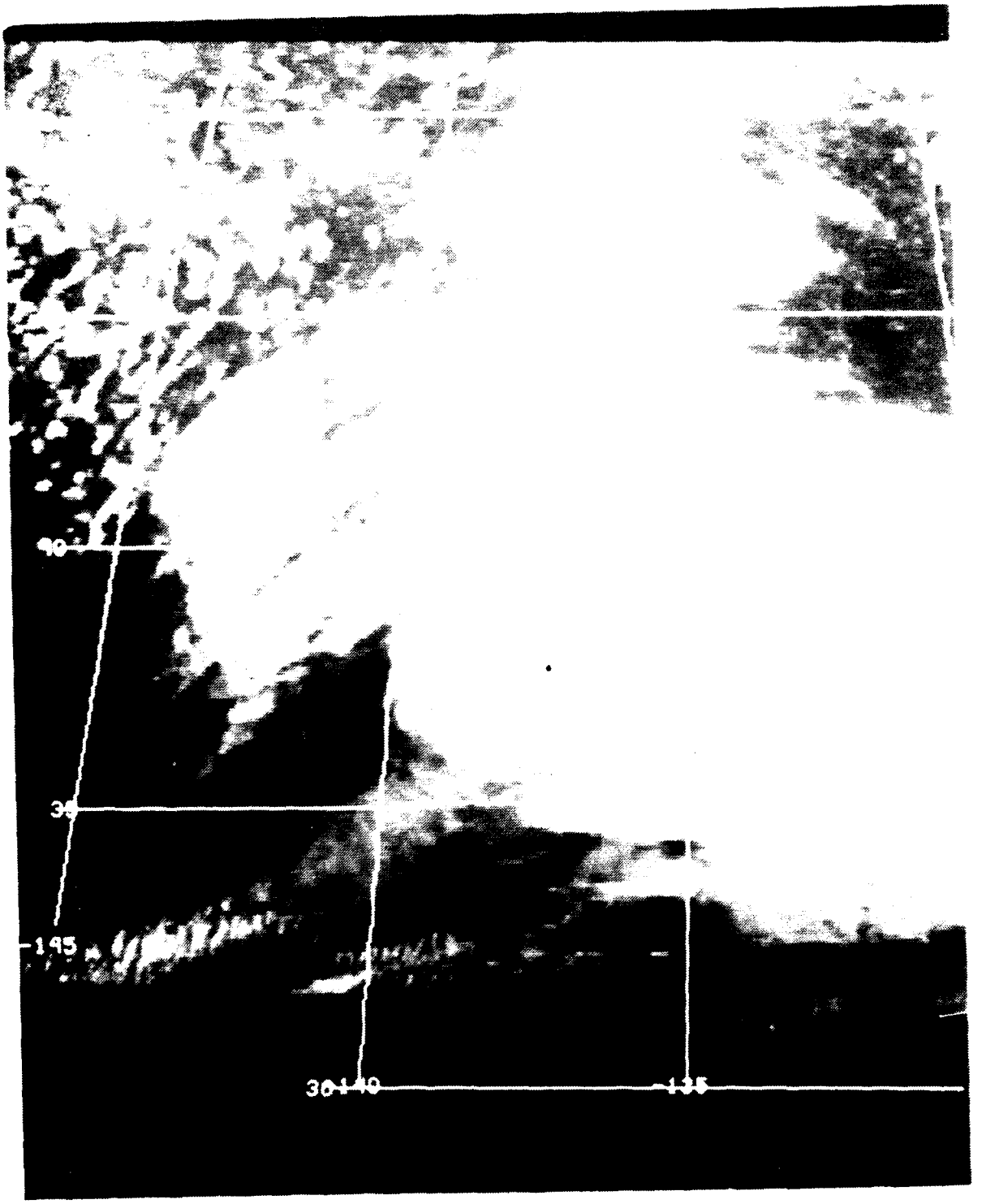

Fig. 14. GOES infrared image at 1816 UTC 16 January 1988.

The NPS precipitation analysis at this time (Fig. 15) depicts a broad area of light to moderate precipitation in the warm air ahead of the surface low. This basic analysis is consistent with the classic structure of warm advection precipitation shields ahead of a developing frontal wave (e.g. Palmen and Newton, 1969).

However, there are some questionable areas. At 1800 UTC moderate rain was reported by a ship near 37° N 140° W. This observation correlates reasonably well with the 1816 UTC visible image that indicates some convective activity near the low itself. However, the NPS model (Fig. 15) appears to underestimate the rain in this region, depicting only broken areas of light rain. The GOES cloud top temperatures are too warm (268K) along the cold front for a classification of rain (nimbostratus or cumulonimbus). However, scattered light to moderate rain is likely in the rope cloud. The model indicates moderate precipitation over the northern region (north of 39° N) because the cloud type analysis classifies the area as cumulonimbus. Based on the imagery, the clouds appear to be mostly cirrus with embedded multi-layered clouds advected ahead of the rain area. In the cold air west of the cyclone, an 1800 UTC ship observation at 37° N 146° W reported rain in the vicinity; none is indicated on the NPS analysis in that area, but there are isolated rain signatures nearby.

Fig. 16 and Fig. 17 depict the visual and infrared GOES imagery at 2316 UTC 16 January. The data show a more organized cyclone with increased convective features near the low and the northern part of the cold front. The multi-layered cloud shield continues to expand downstream of the surface low. Open cell clouds behind the comma cloud west of the frontal low indicate low level cold air advection approaching. The infrared image still shows the cold front to be composed of low clouds. The NPS precipitation analysis at 2316 UTC (Fig. 18) shows most of the activity still associated with warm front. The rain coverage in this area is more compact and representative of the cloud imagery than shown at 1816 UTC, indicating that the cloud structure has become better defined. A 0000 UTC ship observation in the vicinity of the warm front at 37° N 130° W reported rain during the past hour which verifies the model there.

The limitations of the visible and infrared data in depicting precipitation are still present. Some cirrus clouds east-southeast of the cyclone appear to have been misclassified as precipitating clouds. In general, the visual-infrared based estimate seems to have the same problems of overestimating the precipitation intensity downstream of the low and not depicting any precipitation with the shallow cold frontal clouds.

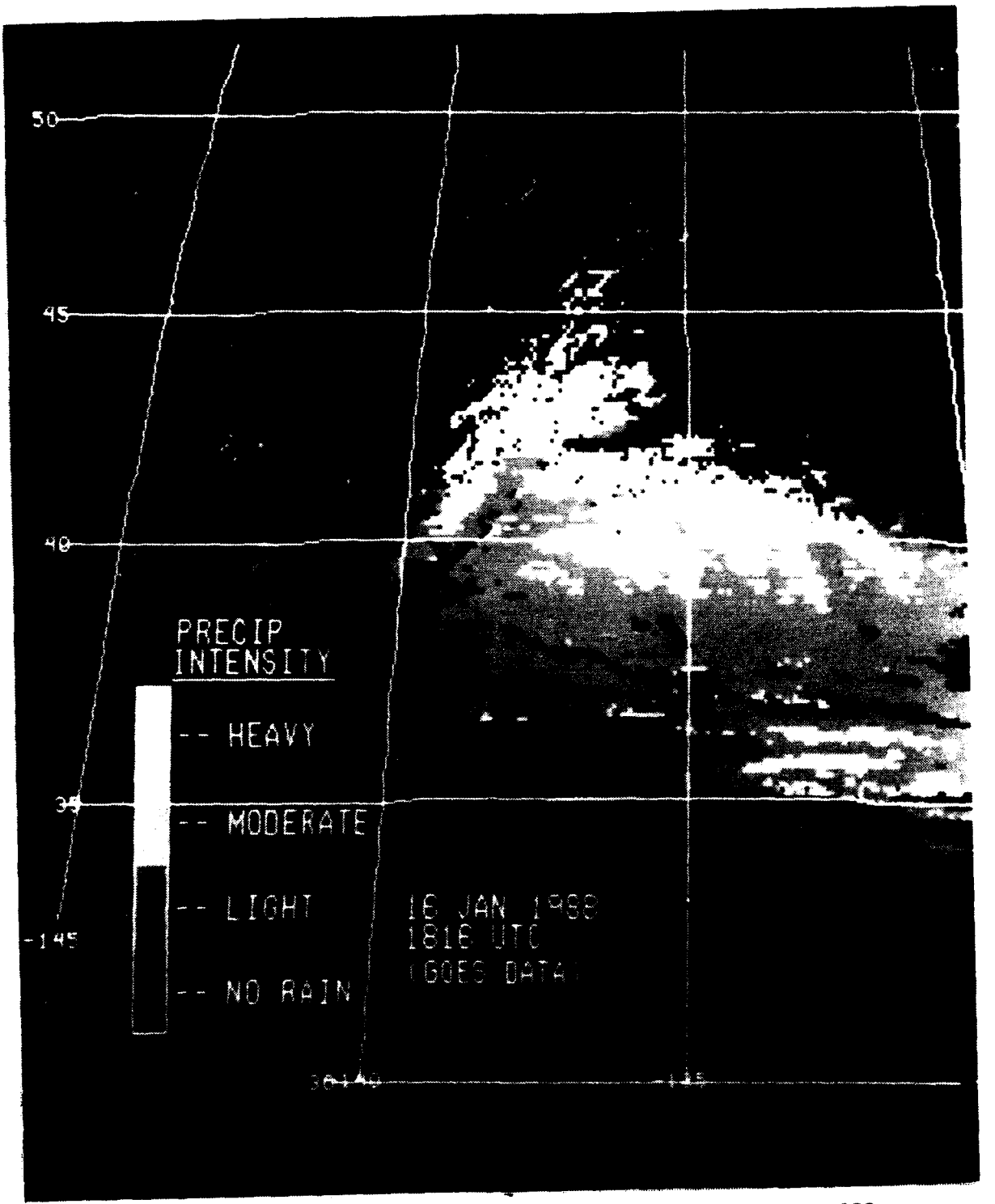

Fig. 15. NPS precipitation analysis (GOES) at 1816 UTC 16 January 1988.

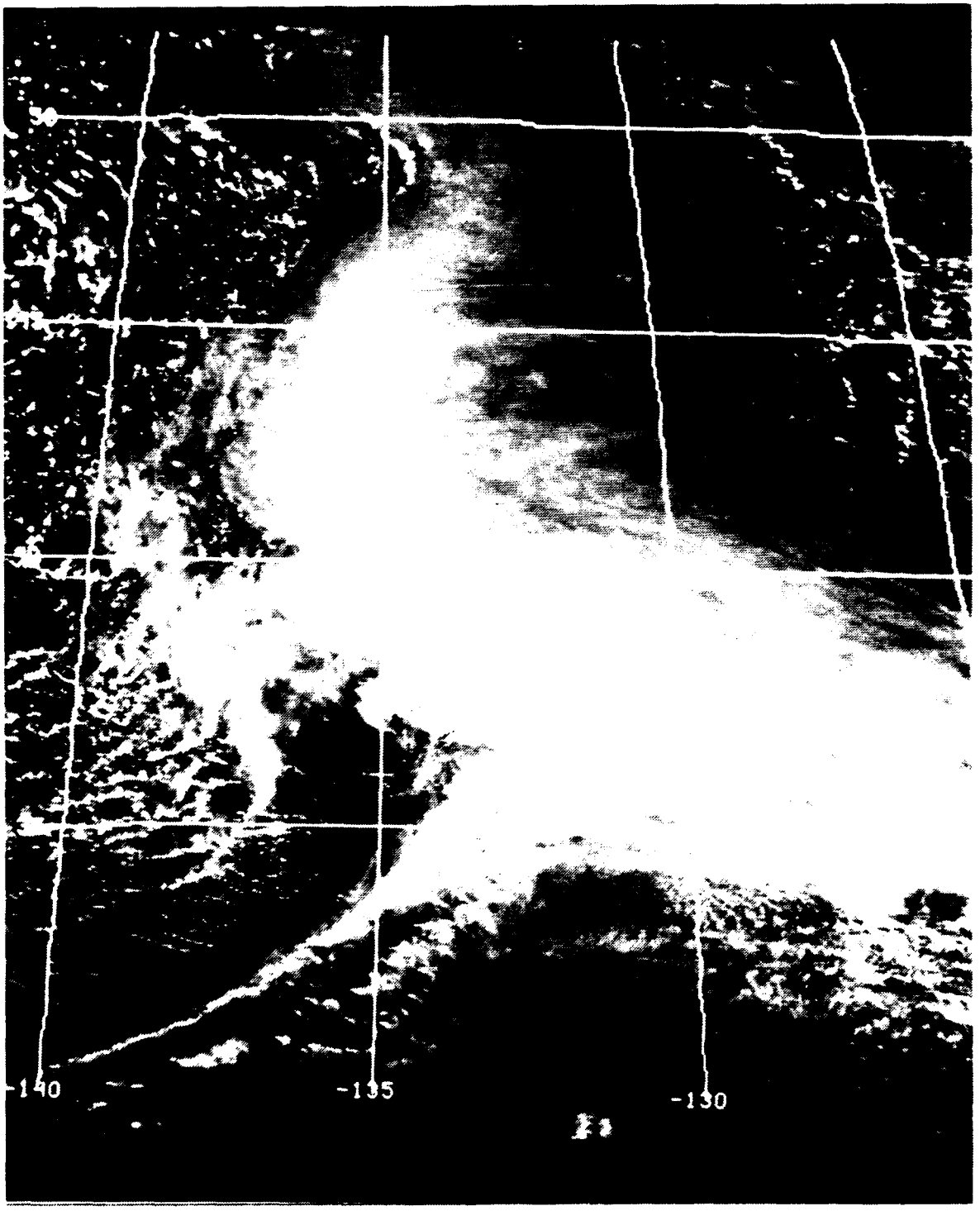

Fig. 16. GOES visual image at 2316 UTC 16 January 1988.

Fig. 17. GOES infrared image at 2316 UTC 16 January 1988.

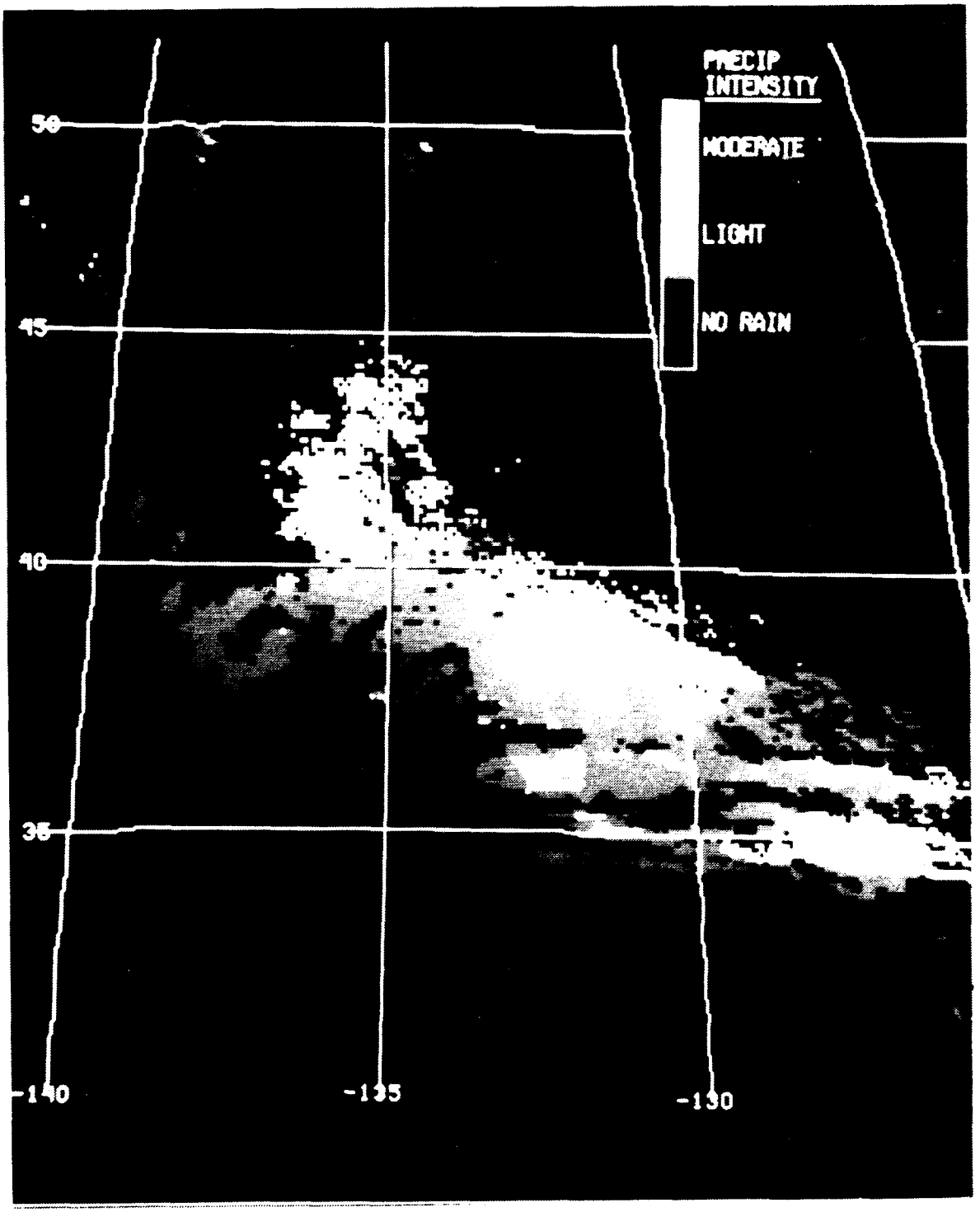

Fig. 18. NPS precipitation analysis (GOES) at 2316 UTC 16 January 1988.

The GOES image (IR only) at 0316 UTC 17 January 1988, shown in Fig. 19, has the low continuing to develop and the front starting to occlude. Coldest cloud top temperatures (230K) surround the low at the apex of the front (37° N 128° W) and in the low's northern sector (38° N 132° W). Significant cold air advection is evident behind the approaching comma cloud, indicating that continued deepening of the surface low is imminent. The cirrus shield persists downstream of the low.

C. AVHRR IMAGERY AND NPS PRECIPITATION ANALYSIS

The AVHRR data presented in this section are remapped into a cylindrical equal distant projection for a 512 x 512 array with a resolution that increases from 0.6 n mi at the nadir point to 2.4 n mi at the edge of the scan. The cloud and precipitation fields approximately cover a 900 x 900 n mi area. The available AVHRR imagery better depicts the basic features described in the previous section. Fig. 20 illustrates the infrared AVHRR image at 1700 UTC 16 January. The picture shows finer detail of the irregularly-shaped convective clouds near the low and along the cold front, and the streaked nature of the jet stream cirrus upstream of the cyclone. Visual and infrared AVHRR imagery at 2300 UTC 16 January, illustrated in Fig. 21 and Fig. 22, also describe these features well. The classic warm front structure of an upward sloping cloud sheet can be discerned from the visual image which shows the multi-layered features becoming progressively thinner (darker) downstream of the cyclone. The highly reflective clouds near the low are an indication of increased thickness, larger cloud droplets and significant precipitation. The visual image depicts a distinct rope cloud in association with the cold front, but the infrared image shows low clouds along the front.

The corresponding NPS precipitation analysis based on the 2300 UTC AVHRR imagery is illustrated in Fig. 23. The analysis has moderate rain in the cloud shield area, but none is shown along the cold front. Like the GOES data, cloud top temperatures are too high (263K) for rain classification along the cold front. Further upstream of the low, cloud top temperatures are four to eight degrees colder than corresponding GOES data which causes the model to classify cumulonimbus in areas where cirrus shields are present. Consequently, the areal coverage and intensity of the forecasted rain appear to be overestimated in this area. In the next section, SSM/I data are used to map the precipitation of this storm.

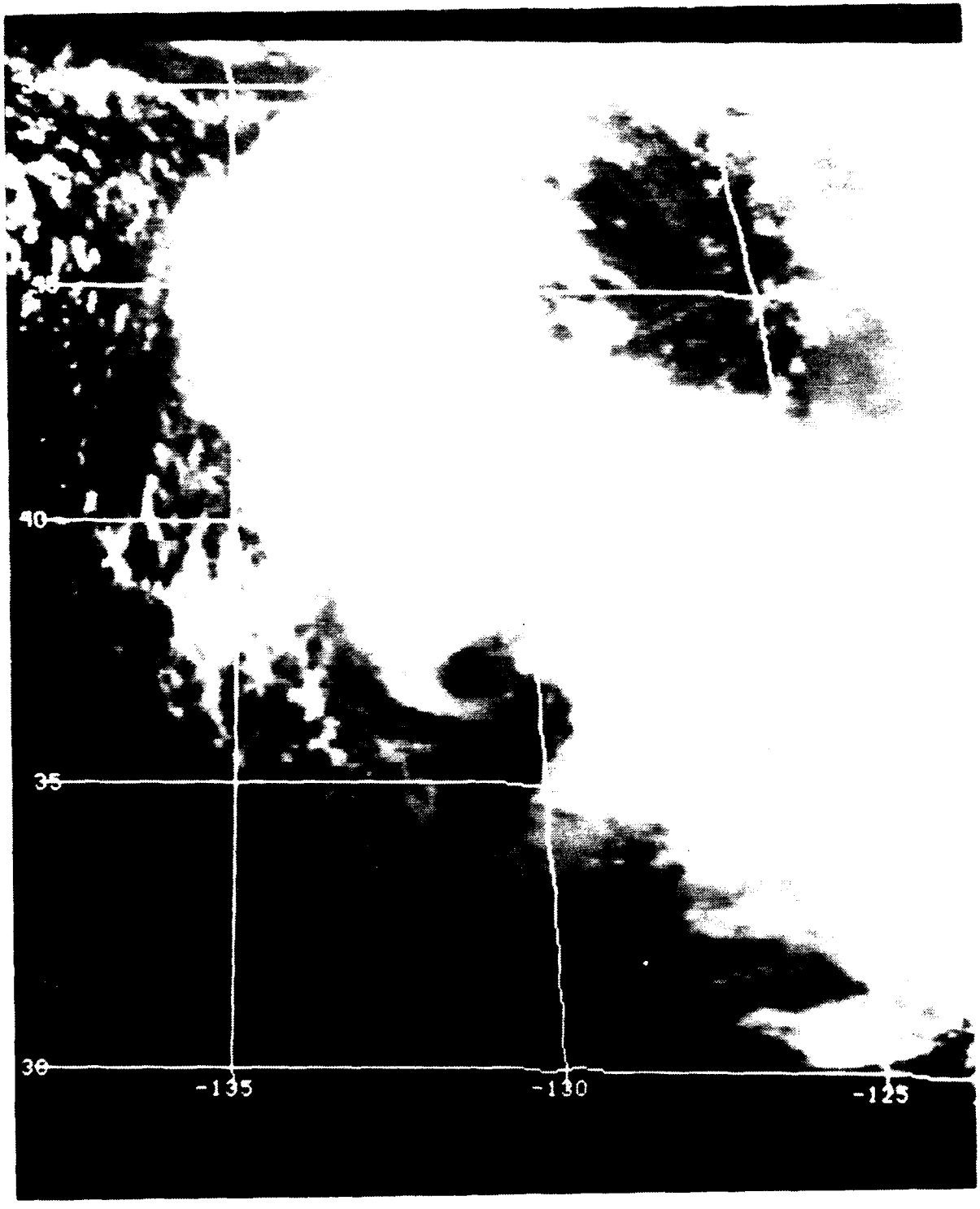

Fig. 19. GOES infrared image at 0316 UTC 17 January 1988.

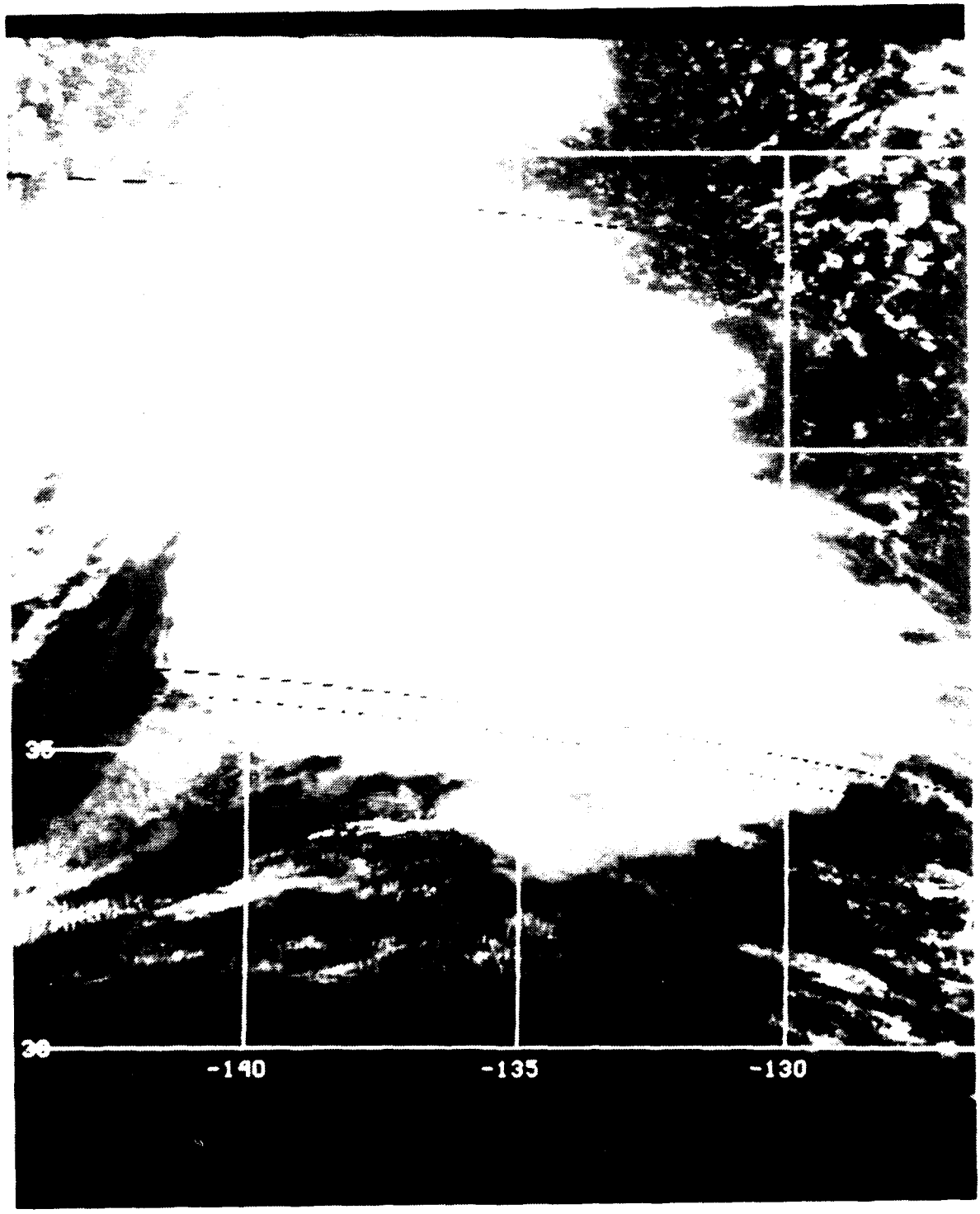

Fig. 20. TIROS-N AVHRR infrared image at 1700 UTC 16 January 1988.

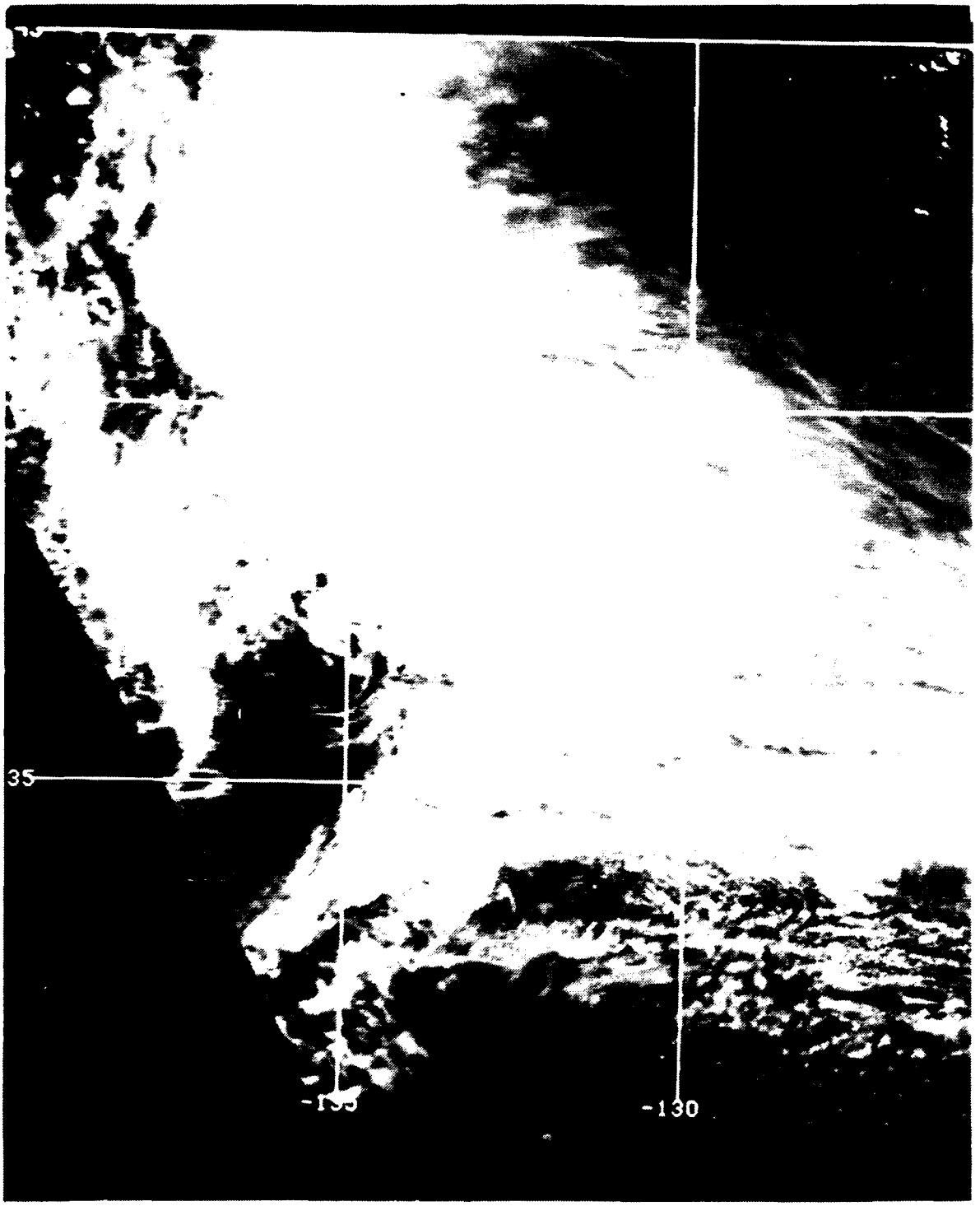

Fig. 21. TIROS-N AVHRR visual image at 2300 UTC 16 January 1988.

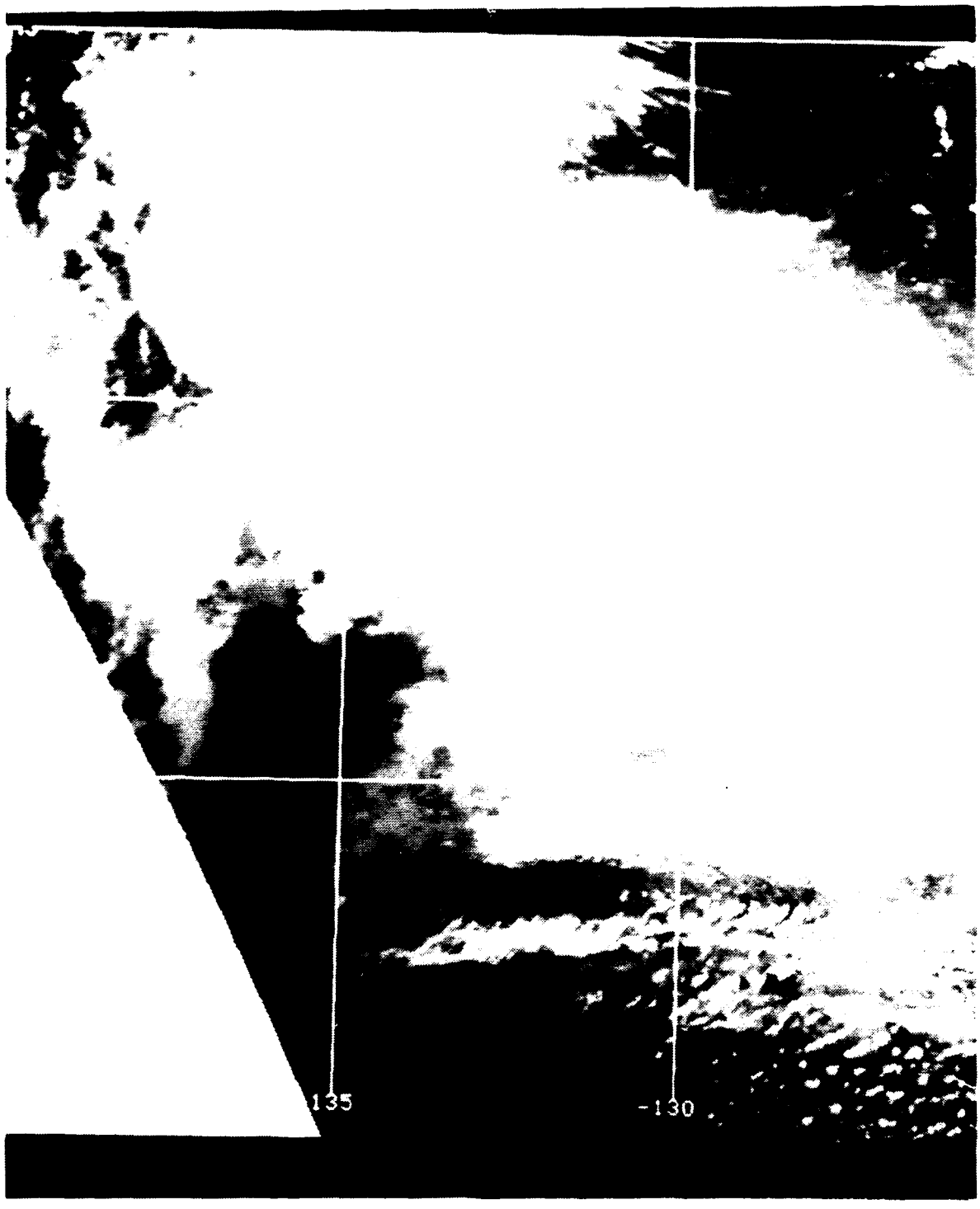

Fig. 22. TIROS-N AVHRR infrared image at 2300 UTC 16 January 1988.

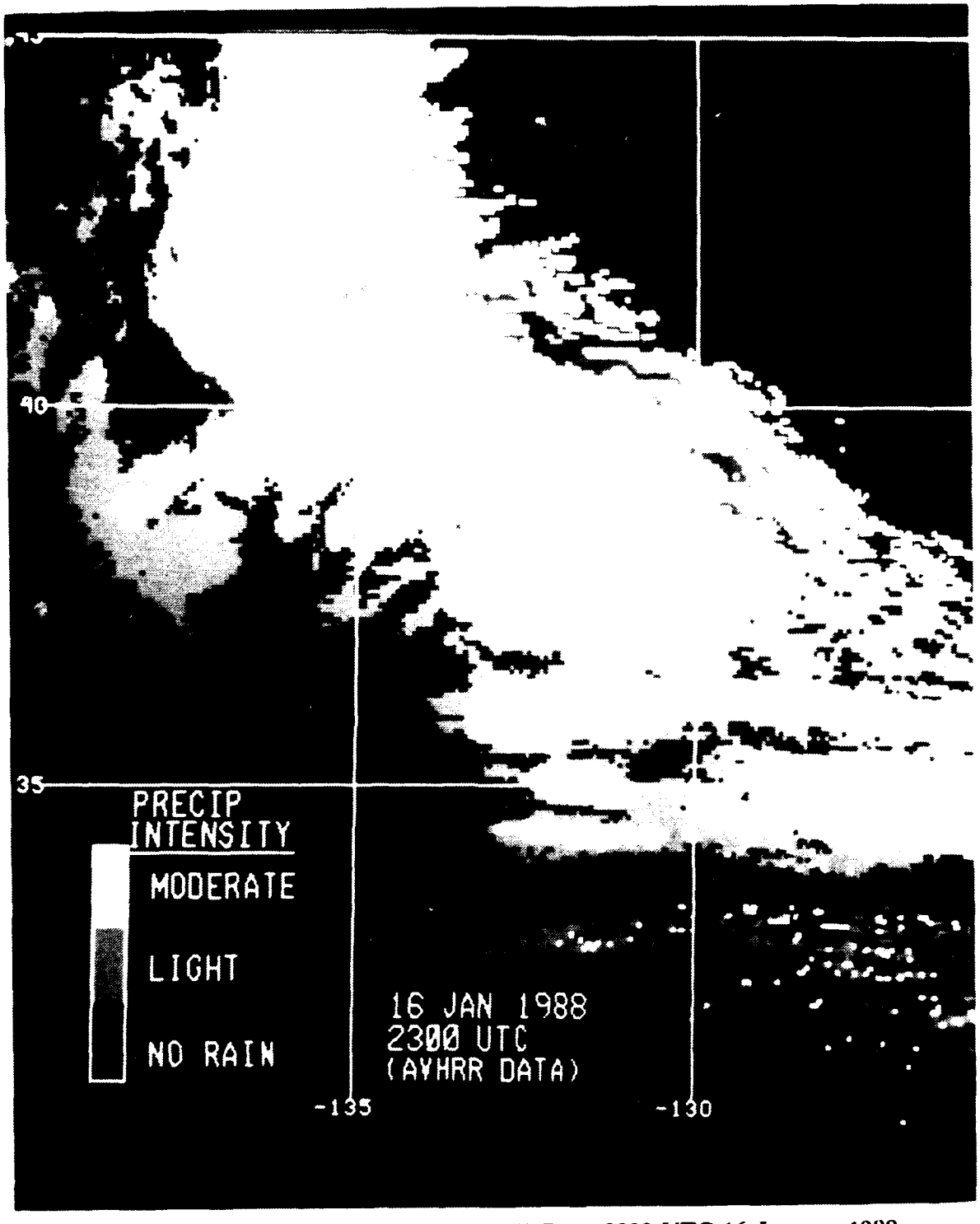

Fig. 23. NPS precipitation analysis (AVHRR) at 2300 UTC 16 January 1988.

D. SSM/I DATA AND PRECIPITATION ANALYSES

1. Brightness Temperature Data at 1500 UTC 16 January 1988

The SSM I brightness temperature data fields are produced using a movable grid for a 512 x 512 array with a field of view that decreases with increasing frequency. The following list indicates the field of view for each channel:

19V - 55.3 km
19H - 55.1 km
22V - 48.6 km
37V - 32.2 km
37H - 32.7 km
85V - 14.8 km
85H - 14.8 km

Fig. 24 and Fig. 25 illustrate the horizontal and vertical components of 19 GHz brightness temperature data. Data at this low frequency theoretically provide the most direct physical relationship between rainfall and observed microwave radiances of the five SSM I channels. At 19 GHz, the opacity of the atmosphere due to water vapor and oxygen is relatively low, so the liquid drops themselves become the dominant contributors to absorption and emission. In these figures, the ocean background is dark (cold) and the atmospheric liquid drops water vapor is bright (warm). The advantage of viewing atmospheric moisture with low frequency microwave energy is readily apparent, as the frontal wave is easily discernable and separate from the trough to the north and the comma cloud to the west. Evidence of rain can be seen where 19H T_B exceeds 160K, which is one of the HAC rain criterion for a middle latitude winter climate. Horizontal and vertical brightness temperature data at 37 GHz, depicted in Fig. 26 and Fig. 27, have very similar features to those at 19 GHz. Evidence of rain from the HAC retrieval can be seen where T_B (37V) - T_B(37H) < 30K. The coverage of this rain criterion is illustrated in Fig. 28. Embedded within the front are three distinct bright (warm) areas in all four images near 36° N 143° W, 37° N 142° W and 37° N 140° W. In these areas, both HAC rain criteria are met. The rain reported 1800 UTC at 37° N 140° W likely corresponds to the bright area near 36° N 143° W, based on upper-level steering flow (west-northwest) and speed of the system (50 kts). However, without more conventional surface observations at this time, it is impossible to confirm precipitation areas. The 37 GHz data provides better resolution due to its smaller field-of-view.

Brightness temperature data at 22 GHz, depicted in Fig. 29, show that the frontal wave and other cloud features are less distinctive than those at 19 GHz and 37 GHz due to the high degree of water vapor contamination at 22 GHz. The noteworthy

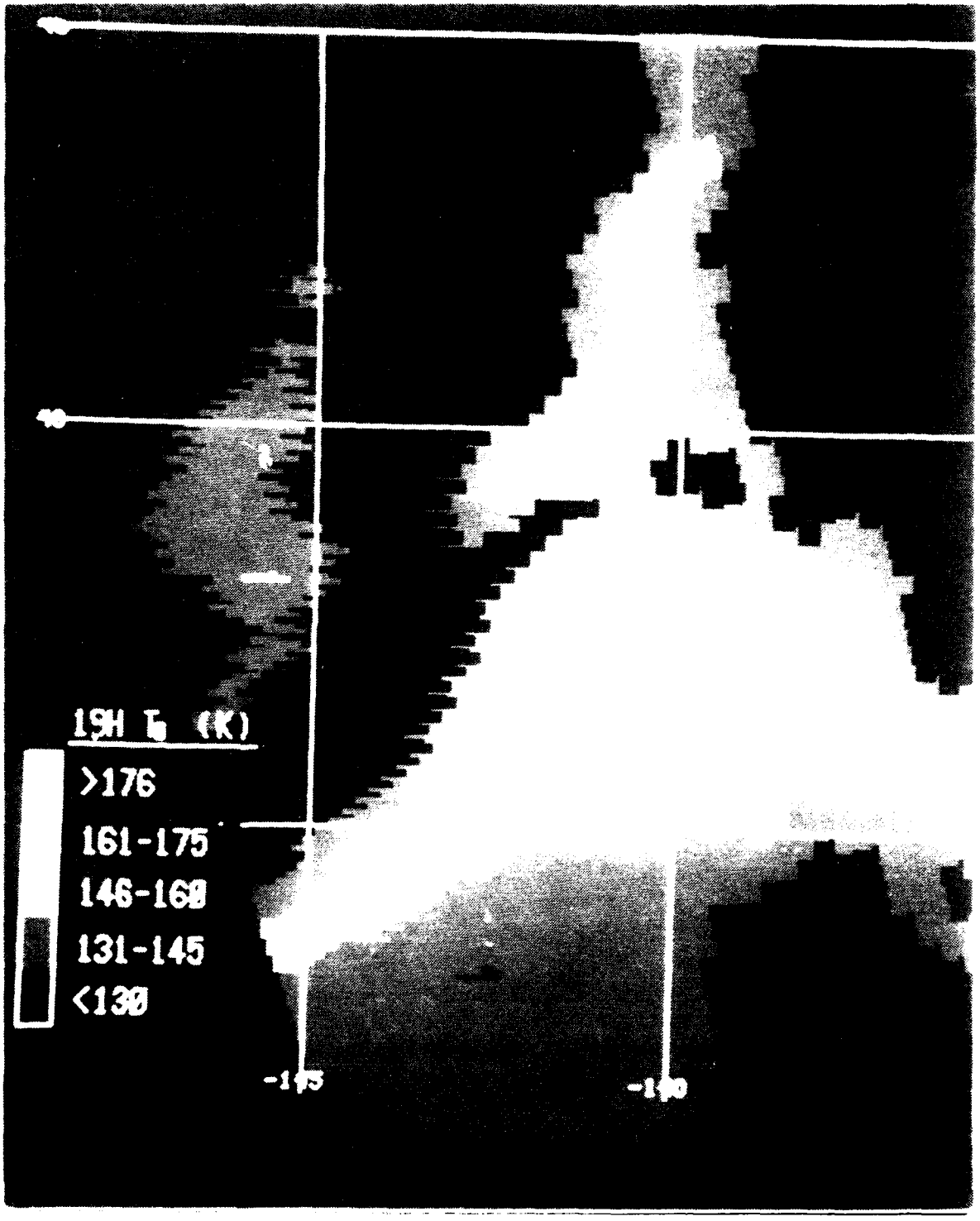

Fig. 24. SSM/I 19 GHz (horizontal) brightness temperature image at 1500 UTC 16 January 1988.

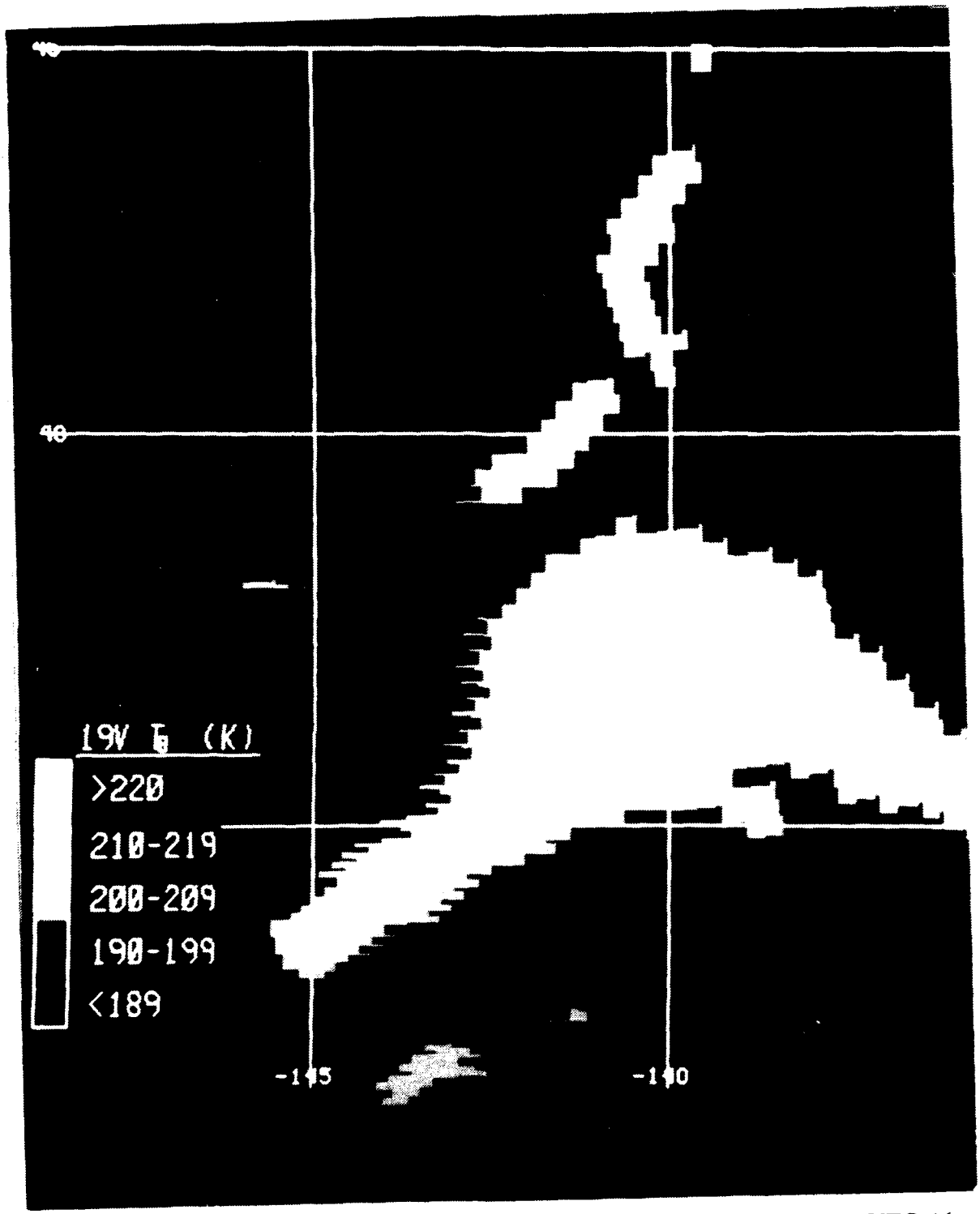

Fig. 25. SSM/I 19 GHz (vertical) brightness temperature image at 1500 UTC 16 January 1988.

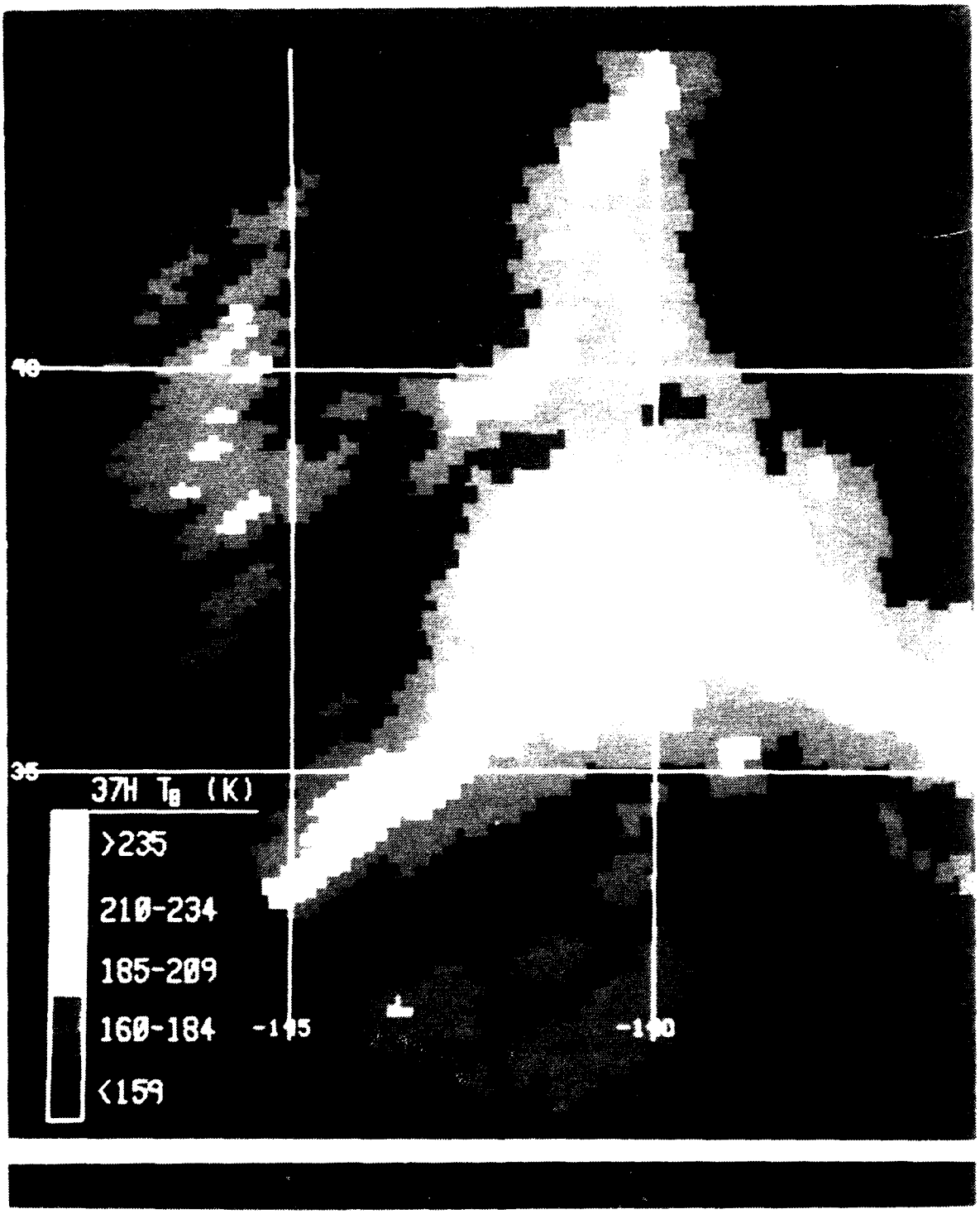

Fig. 26. SSM/I 37 GHz (horizontal) brightness temperature image at 1500 UTC 16 January 1988.

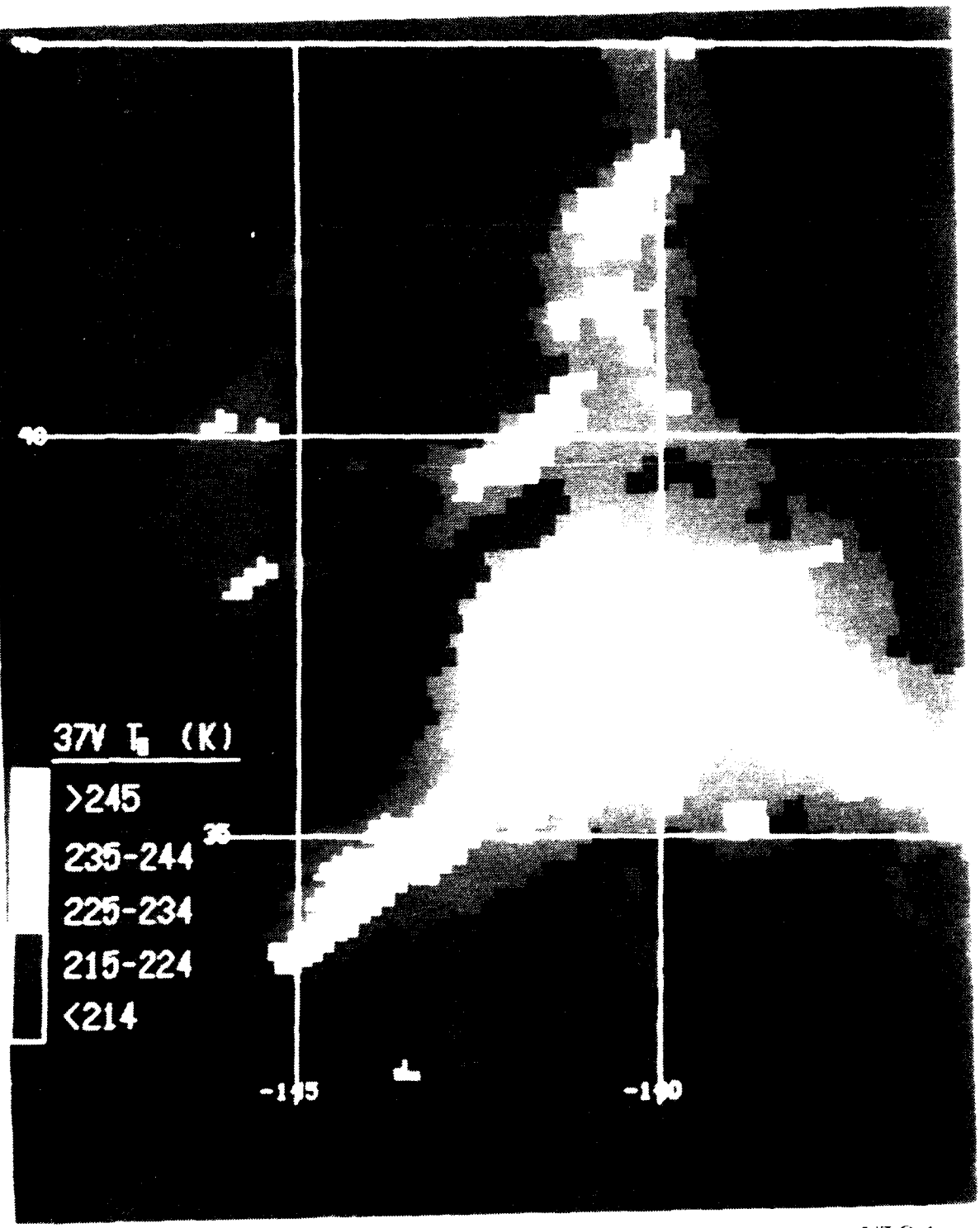

Fig. 27. SSM/I 37 GHz (vertical) brightness temperature image at 1500 UTC 16 January 1988.

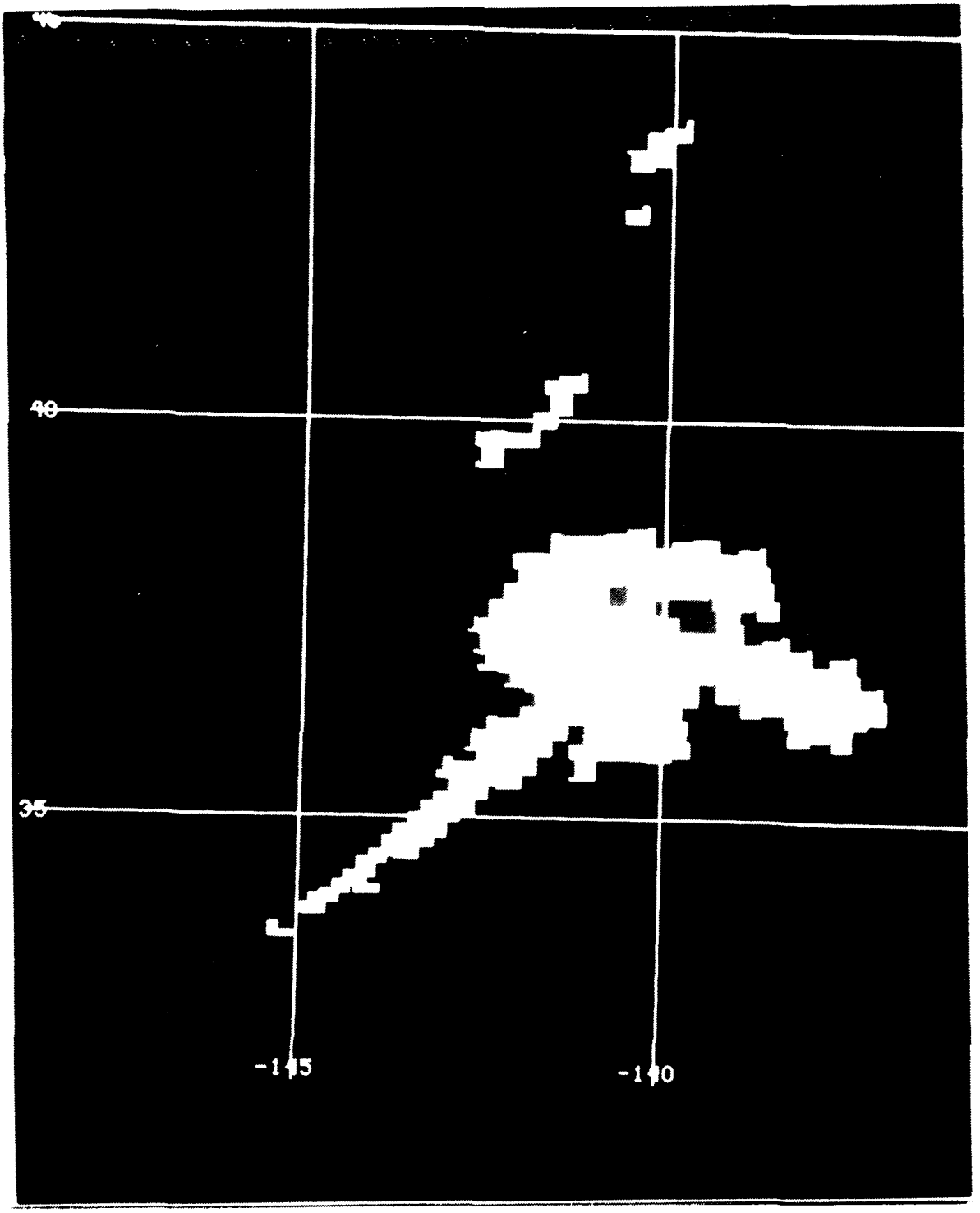

Fig. 28. SSM/I 37 GHz brightness temperature difference (37V - 37H) < 30K at 1500 UTC 16 January 1988.

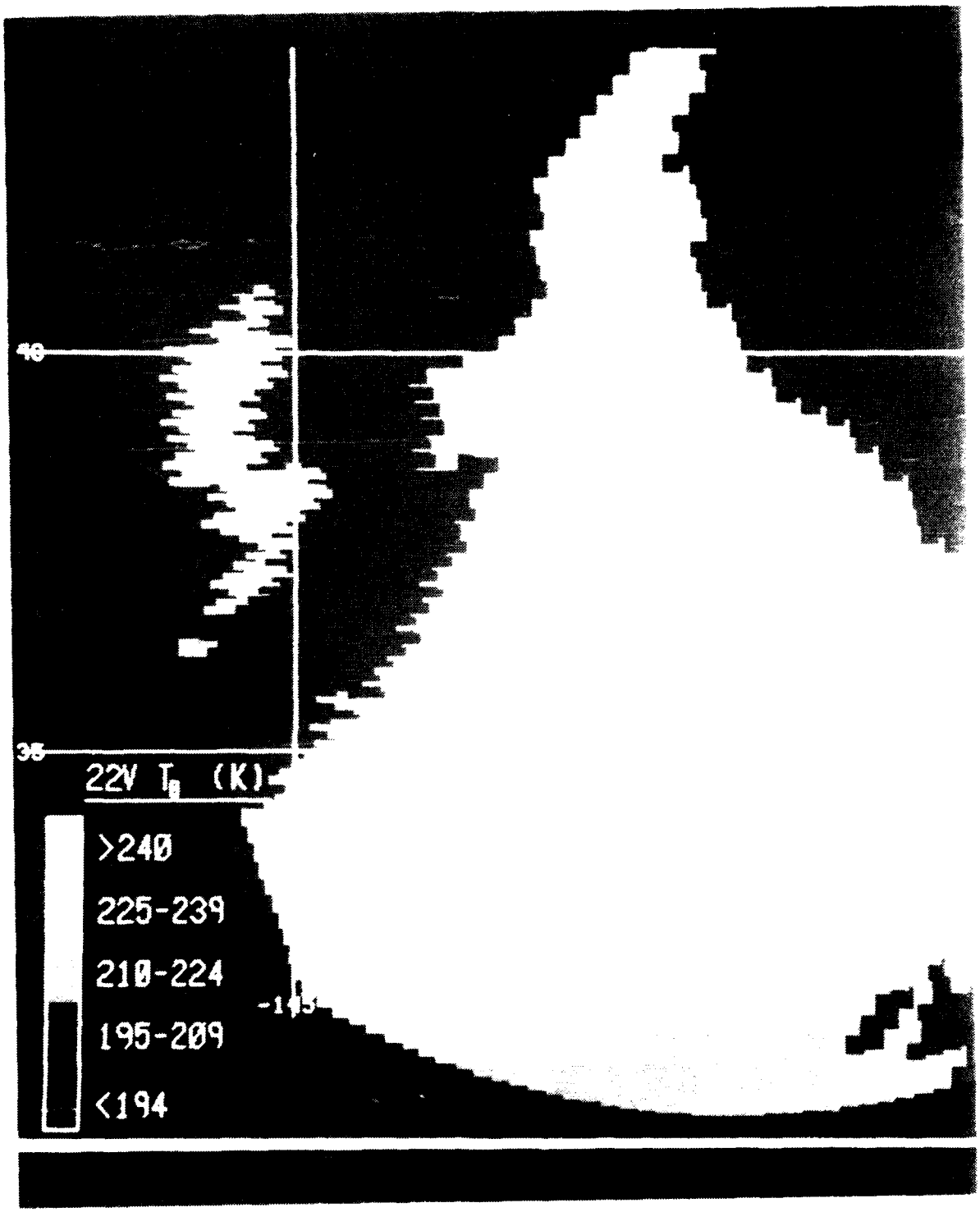

Fig. 29. SSM/I 22 GHz (vertical) brightness temperature image at 1500 UTC 16 January 1988.

feature of this channel is the widespread moisture evident in the warm sector of the frontal wave. Also, the brightest areas embedded in the front correspond well to those shown at 19 and 37 GHz, which adds credibility to the likelihood of precipitation in those regions.

Fig. 30 and Fig. 31 show the horizontal and vertical T_B images at 85 GHz. At this frequency, the attenuation effects of both absorption and scattering are evident. These effects are illustrated very clearly due to the higher resolution at 85 GHZ. Within the cold front, the bright features indicate warm emission from the low-level cumuliform clouds. Embedded within the warm region are scattered cool areas that may represent volume scattering effects from precipitation-size ice. It is interesting to note that the cool area centered near 36° N 143° W has a corresponding distinct brightness at the three lower frequencies. The most striking features are the isolated dark (cold) areas on the 85V image associated with the western comma cloud and the front to the north. These signatures are likely the scattering from precipitation-size ice caused by convection. The dark areas associated with the northern front correlate to bright areas at 19 GHz where T_B (19H) > 160, which supports the possibility of rain in those regions.

2. Precipitation Analysis at 1500 UTC 16 January 1988

The HAC retrieval algorithm for rain rate uses an emission mode (T_B (19H)) and the polarization diversity at 37 GHz for the scattering effect. The resultant rain rate from this algorithm is depicted in Fig. 32. This figure represents the results calculated directly by HAC. The coverage of precipitation concentrated near the low itself and along the cold front are consistent results based on the visible and infrared imagery which shows most of the potentially precipitating clouds in those areas. The primarily light rain rate intensity (< 4 mm hr) is also reasonable in view of the fact that the cyclone is in a formative stage at this time.

However, the HAC algorithm underestimates the coverage of rainfall, based on the criteria from which it is formulated, i.e. T_B (19H) > 160K and T_B(37V) - T_B (37H) < 30K. Compared with the areal coverages of the 19 GHz T_B threshold (Fig. 24) and the 37 GHz polarization difference rain flag (Fig. 28), the rain coverage of the retrieval algorithm is notably smaller. The reason for this inconsistency is not known. Based on a subjective analysis of corresponding visual and infrared imagery, the HAC algorithm appears to underestimate the rain coverage, especially within the northern front and in the cold, unstable air associated with the western comma cloud. This problem may be attributed to the large field of view at the lower frequencies, which will not resolve the brightness temperatures associated with the smaller, isolated rain features.

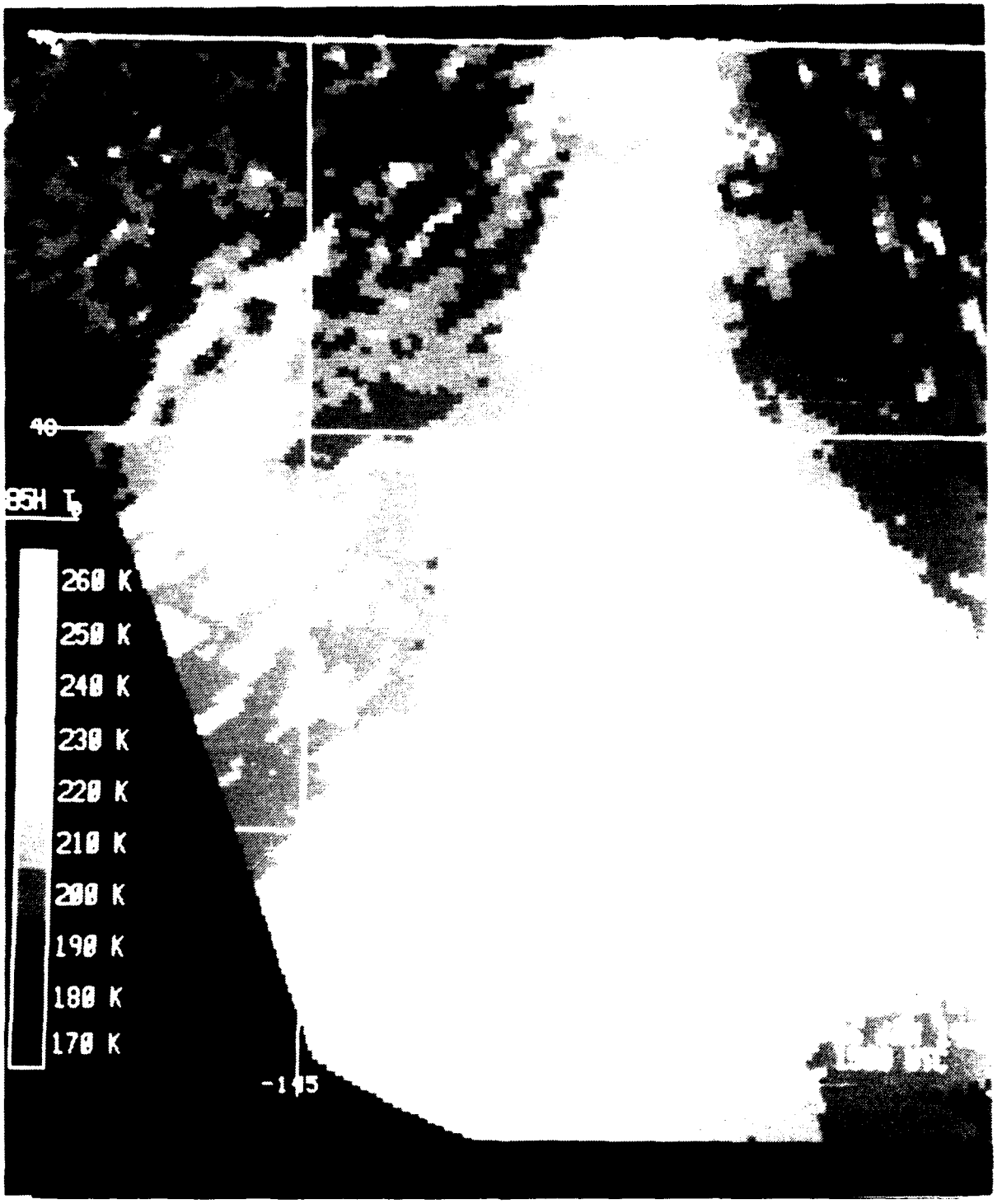

Fig. 30. SSM/I 85 GHz (horizontal) brightness temperature image at 1500 UTC 16 January 1988.

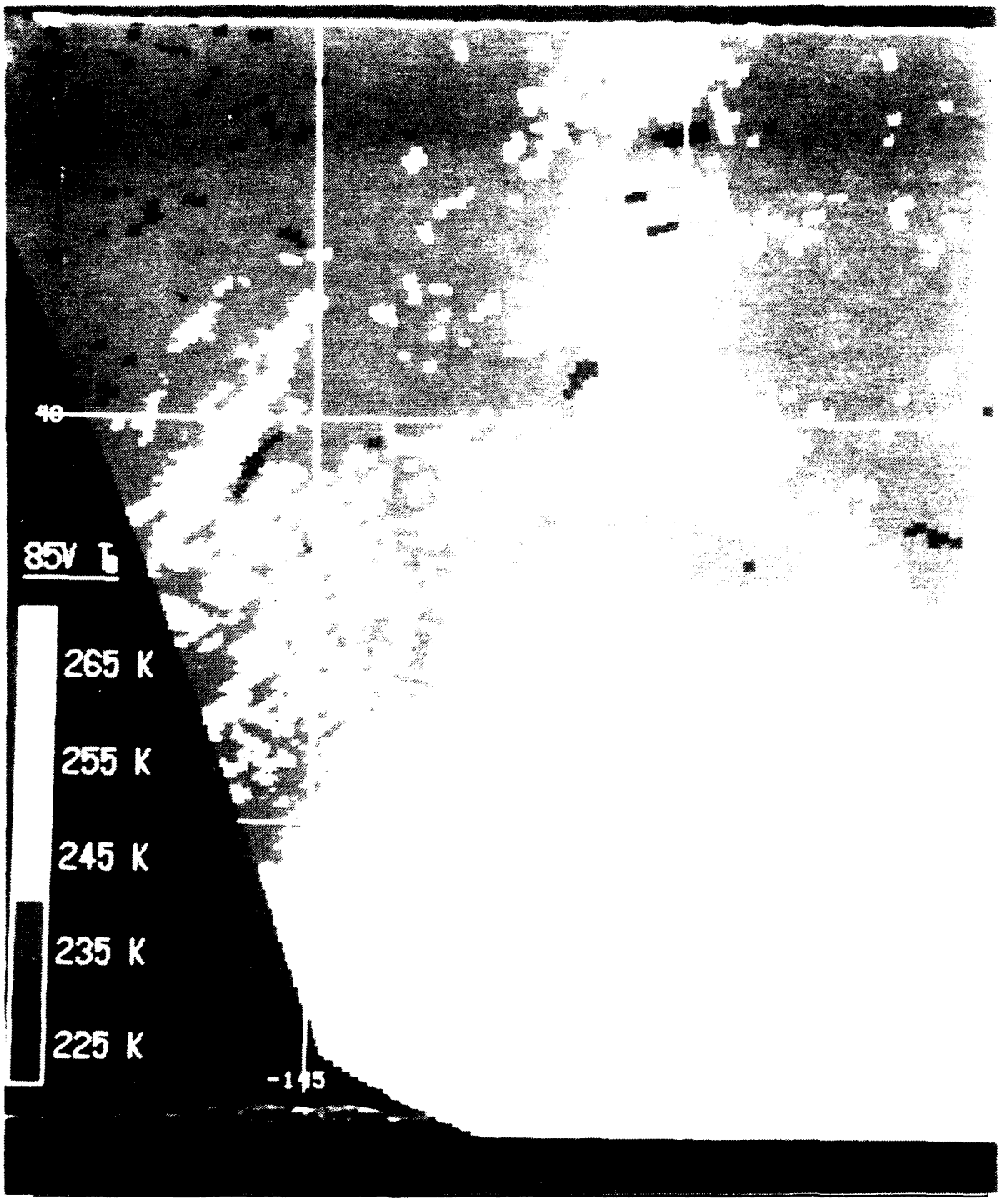

Fig. 31. SSM/I 85 GHz (vertical) brightness temperature image at 1500 UTC 16 January 1988.

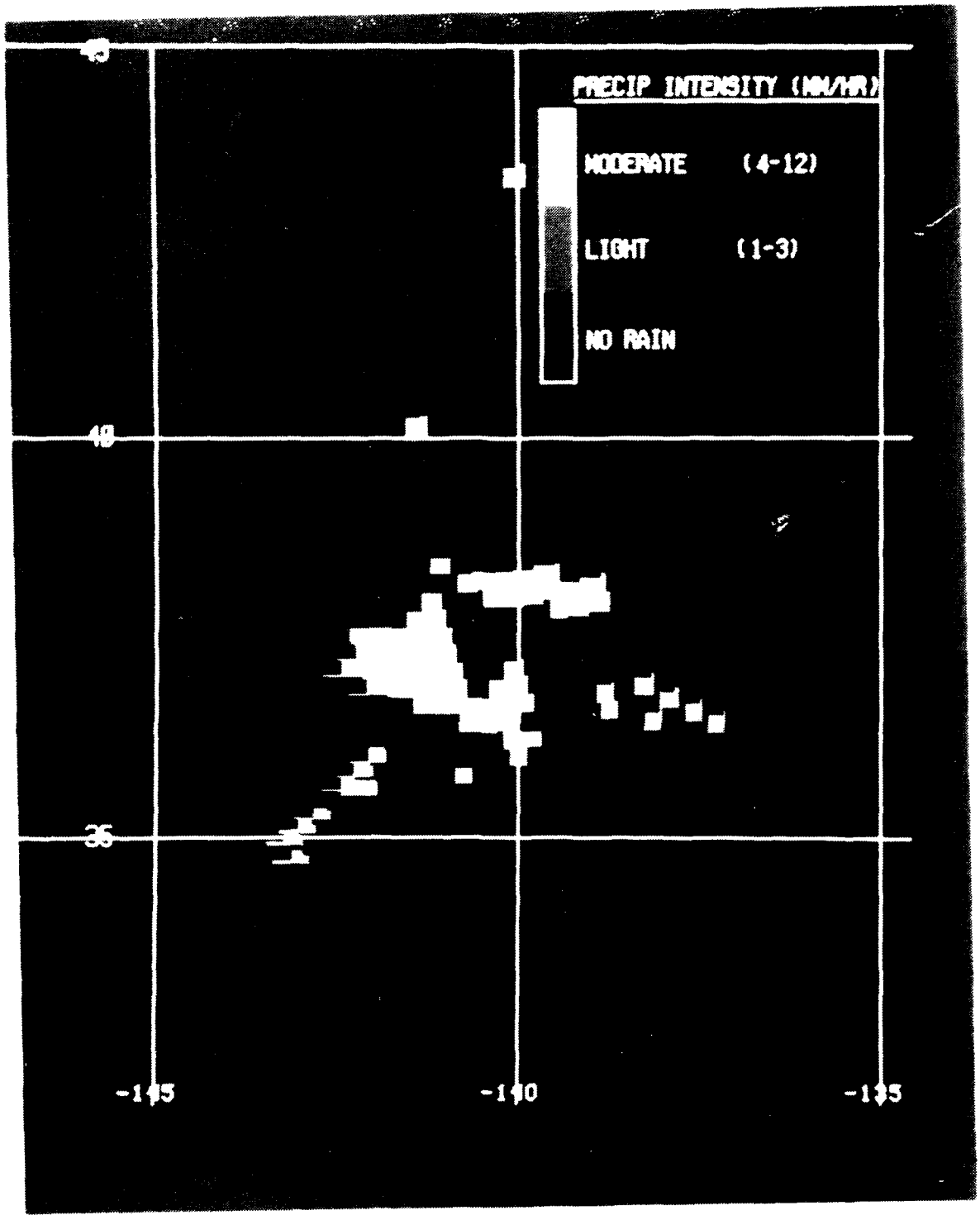

Fig. 32. SSM/I HAC precipitation image at 1500 UTC 16 January 1988.

The PCT algorithm at this time, illustrated in Fig. 33, shows more rainfall in the northern latitudes, especially associated with the northern front. Here, the lower freezing levels and convective clouds increase the probability of scattering from precipitation-size ice particles. The 1800 UTC rain report at 37° N 146° W adds credibility to the rain signature associated with the comma cloud northwest of the frontal wave. The rain area in the northern front appears reasonable based on the solid cloud signature associated with it. The potential weakness of the PCT scheme lies in its inability to estimate rain dominated by stable or warm processes. This problem is evident by the lack of rain signature within the core of the developing low and along the northern part of the cold front.

3. Brightness Temperature Data at 0300 UTC 17 January 1988

Microwave radiance data 12 hours later reveal a more organized system. From the 19 GHz brightness temperature data, shown in Fig. 34 and Fig. 35, the outline of the storm is depicted by a classic cyclonic signature. The large spatial pattern of the HAC rain flag (> 160K at 19H) suggests that significant precipitation development has occurrred within the frontal system. The maximum temperature within the 19H warm core is 222K. Not surprisingly, a 0000 UTC ship observation at 37° N 130° W reported rain within the past hour. The relatively high emissivity of the land feature (California coast) is an indication that microwave precipitation methods using emission-dominated modes (low frequency) cannot discern rain over land, especially at lower rain rates.

Fig. 36 and Fig. 37 illustrate the horizontal and vertical brightness temperatures at 37 GHz. These images depict a broad area of rain signature proposed by the HAC method, i.e. $T_B(37V) - T_B(37H) < 30K$. Fig. 38 shows the areal coverage of this rain criterion. This area represents volume scattering from precipitation-size ice particles produced by increased convective activity around the storm. It is interesting to note that the 12 hour T_B warming of the core region is significantly less (< 10K) than that seen at 19 GHz. This reduction in warming can be directly attributed to the cooling from the scattering (Spencer, 1986).

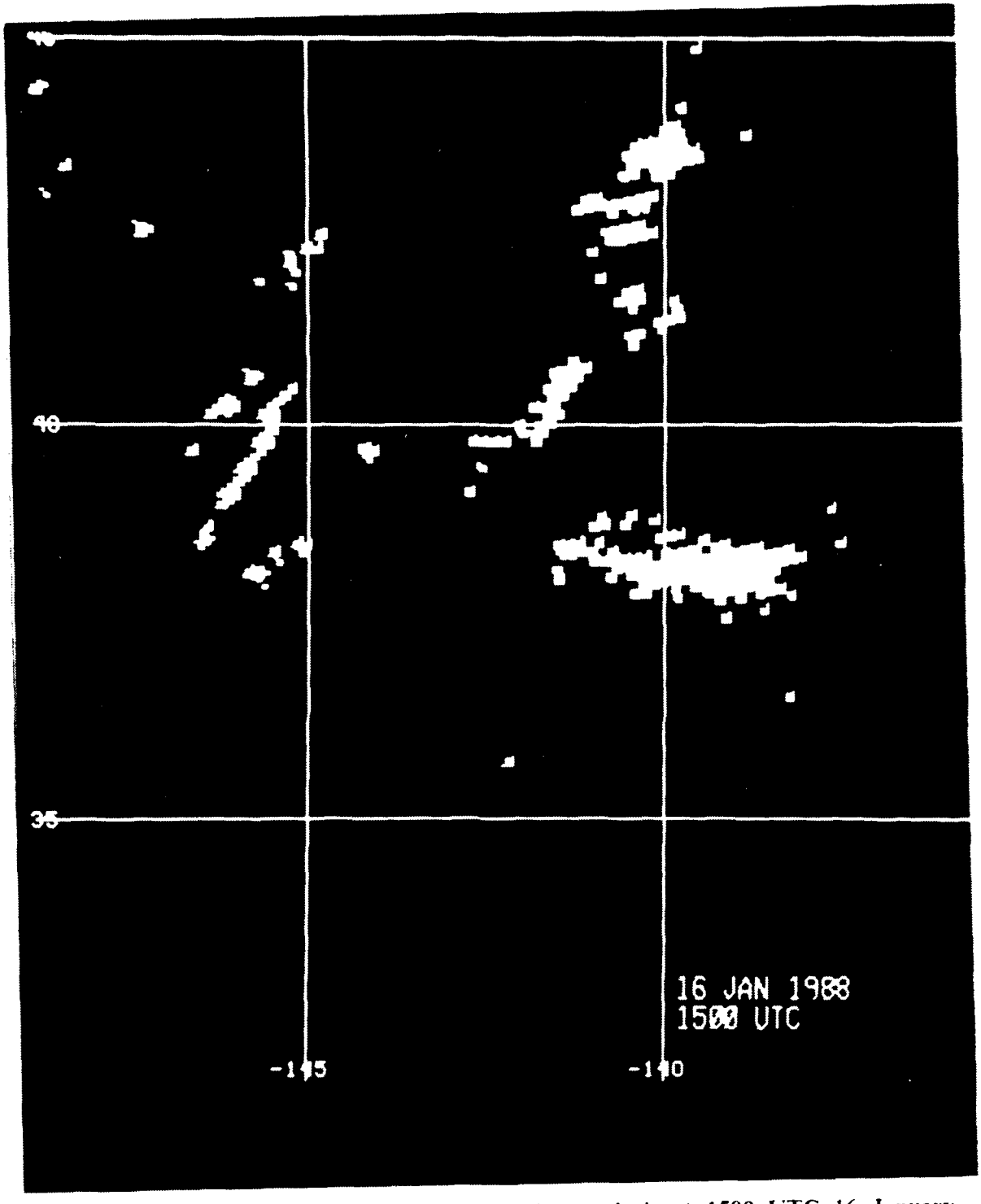

Fig. 33. SSM/I 85 GHz PCT precipitation analysis at 1500 UTC 16 January 1988: Coverage depicts PCT < 255K, rain rate ≥ 1-3 mm hr.

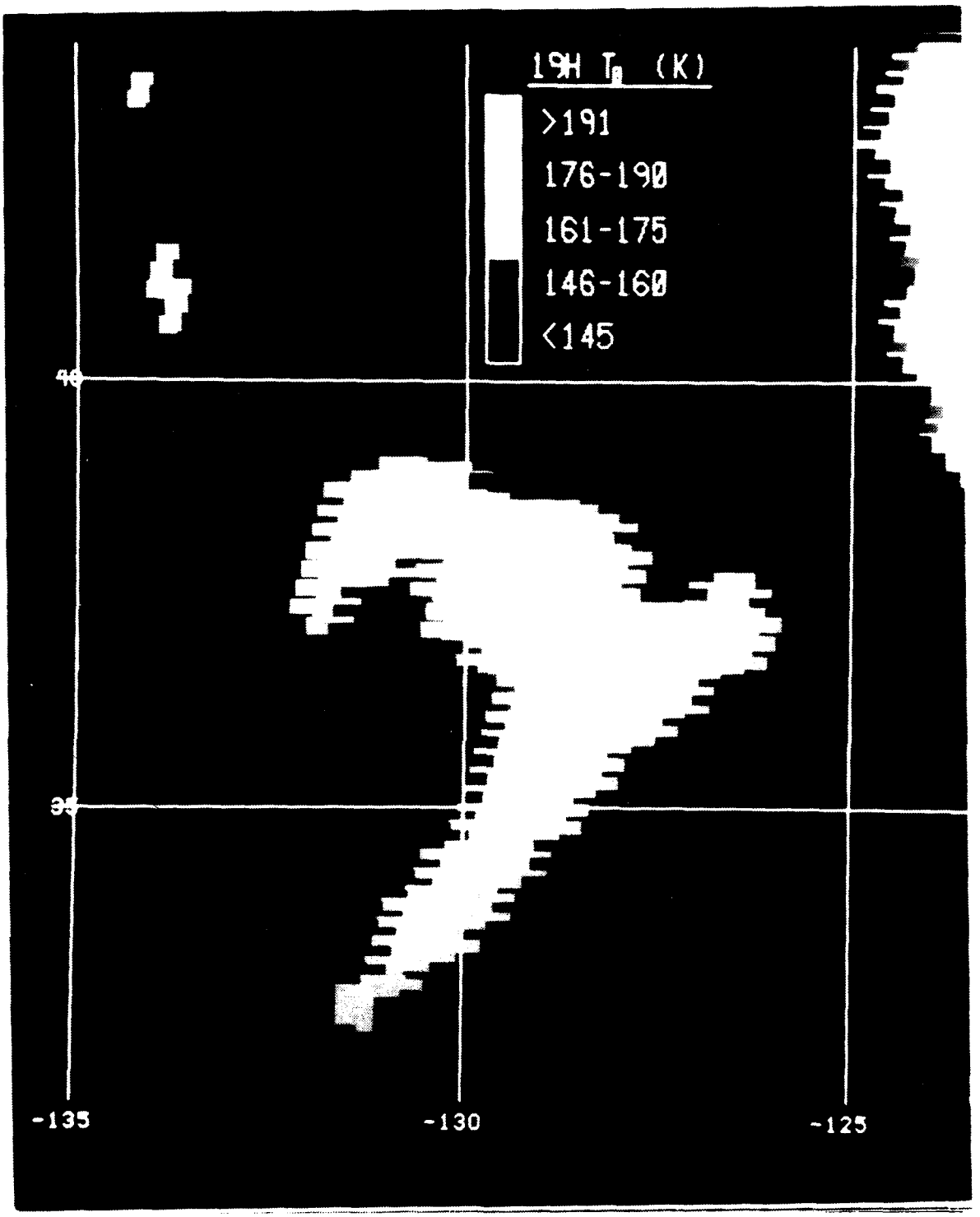

Fig. 34. SSM/I 19 GHz (horizontal) brightness temperature image at 0300 UTC 17 January 1988.

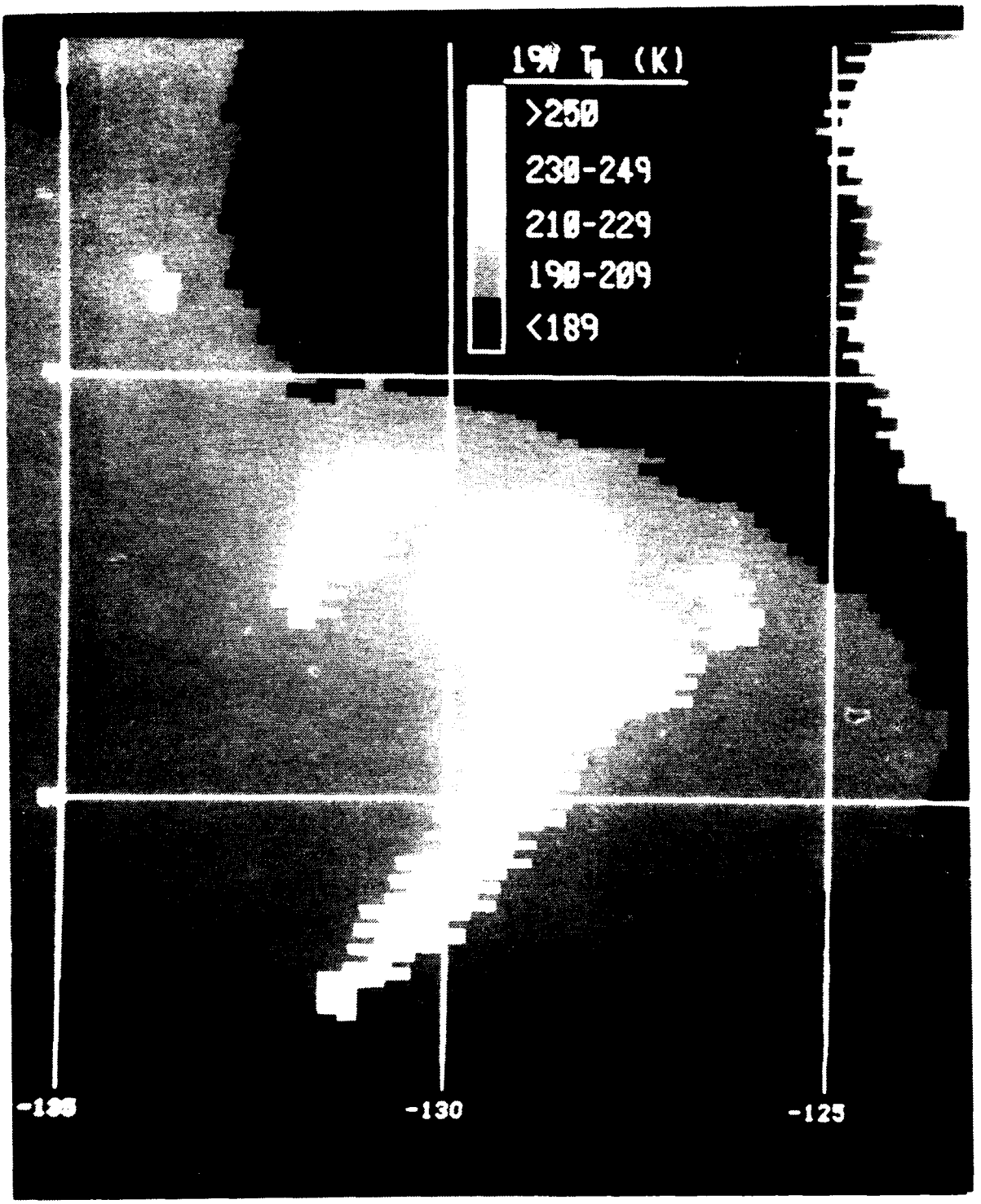

Fig. 35. SSM/I 19 GHz (vertical) brightness temperature image at 0300 UTC 17 January 1988.

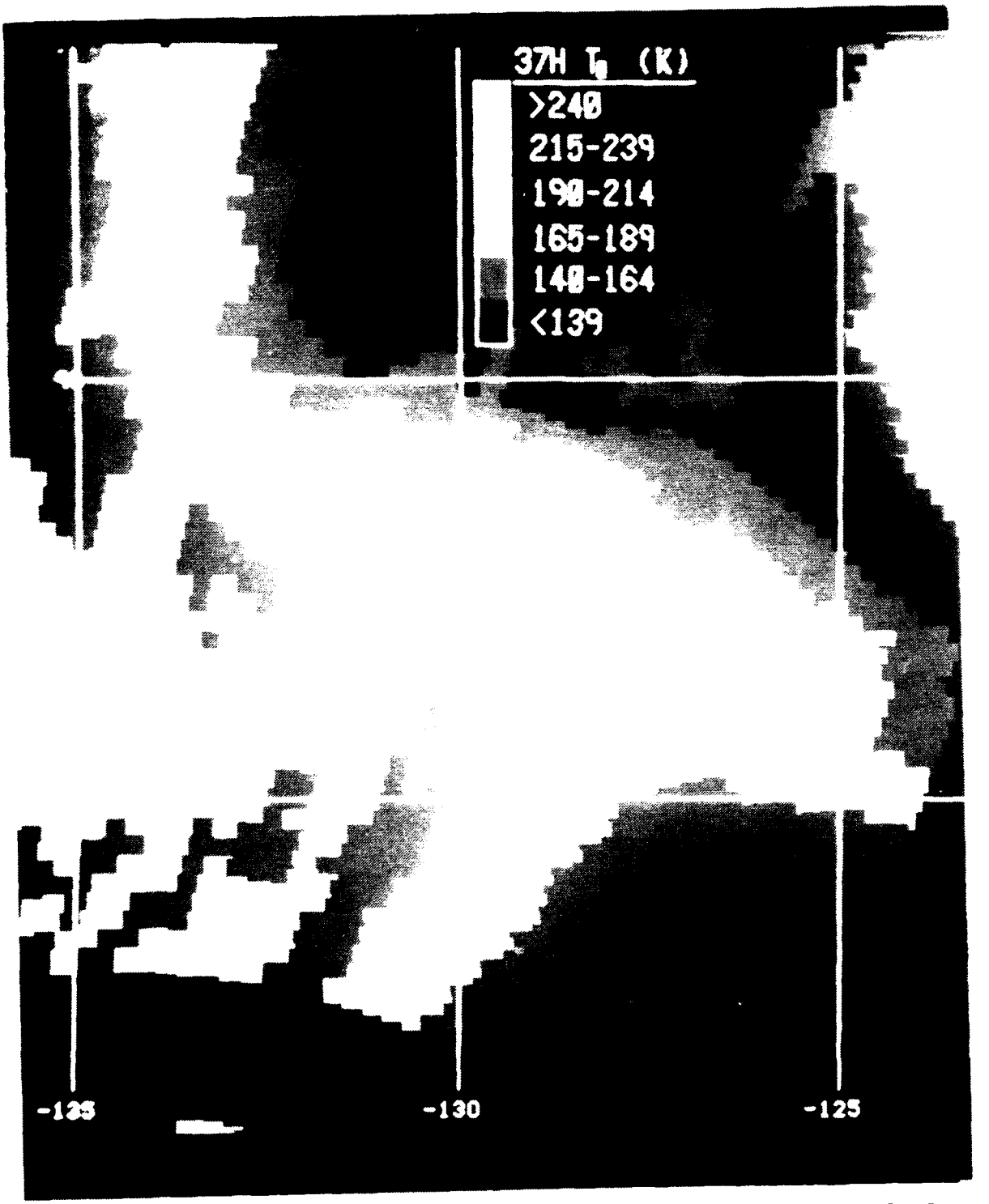

Fig. 36. SSM/I 37 GHz (horizontal) brightness temperature image at 0300 UTC 17 January 1988.

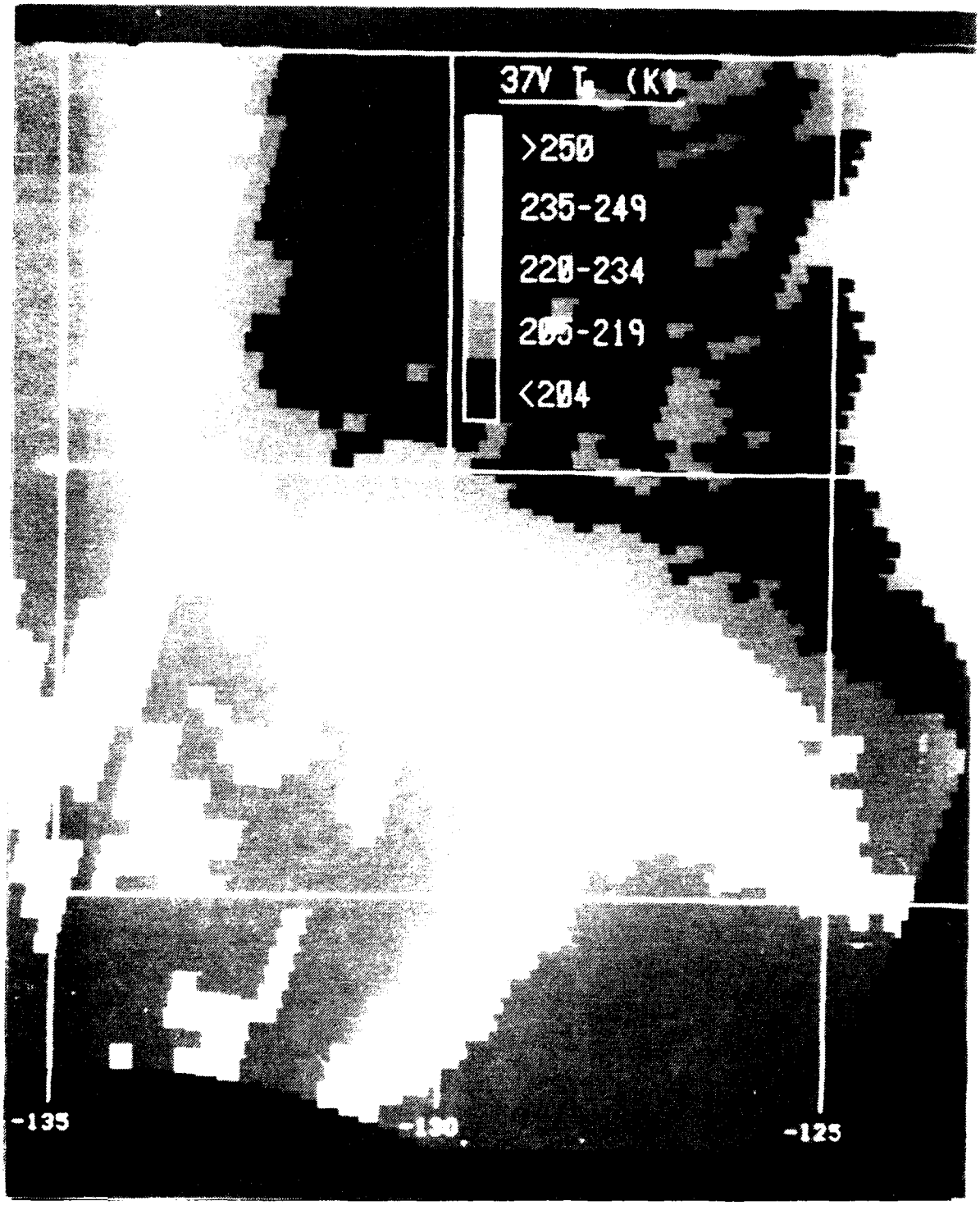

Fig. 37. SSM/I 37 GHz (vertical) brightness temperature image at 0300 UTC 17 January 1988.

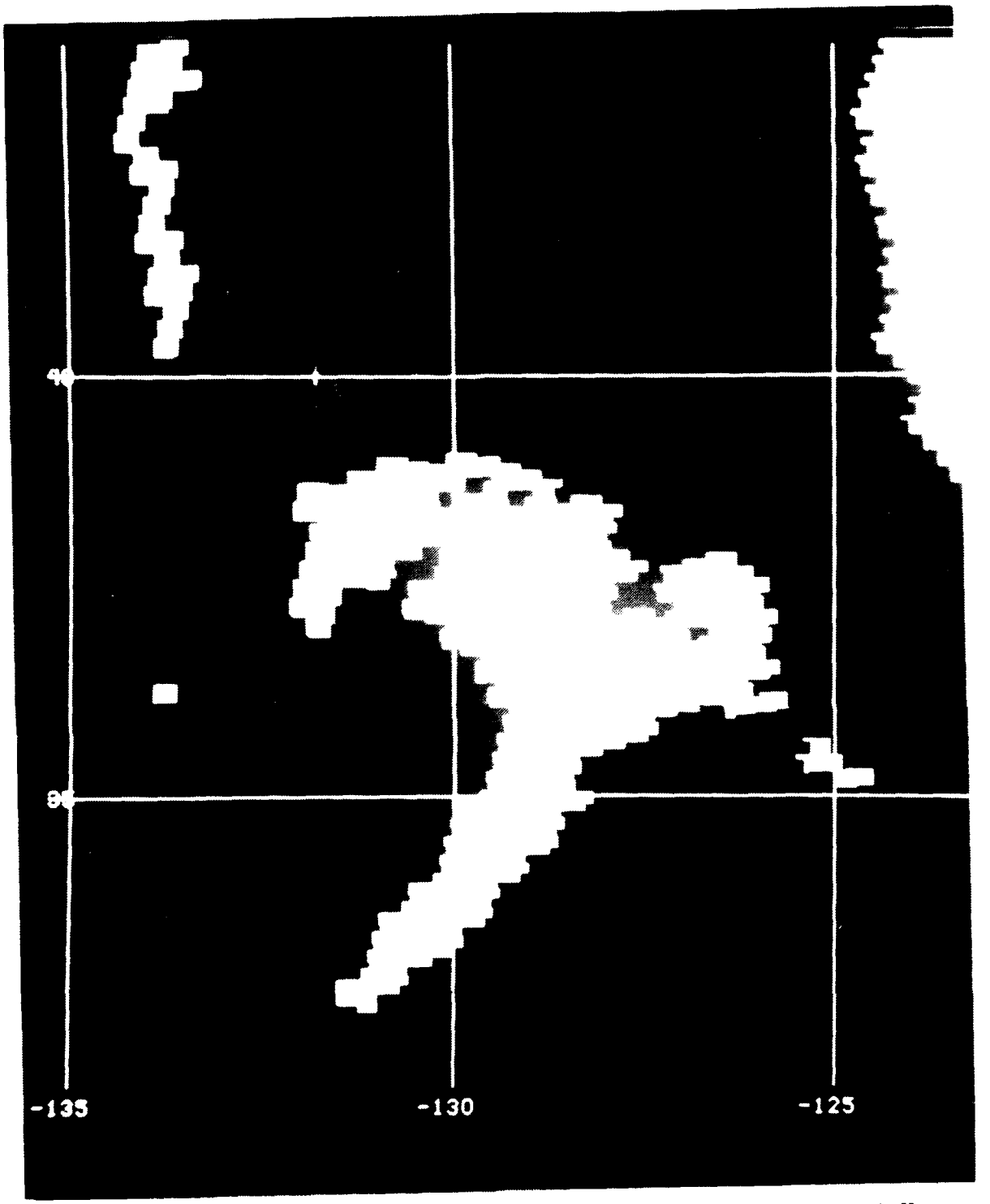

Fig. 38. SSM/I 37 GHz brightness temperature difference (37V - 37H) < 30K at 0300 UTC 17 January 1988.

The 85H (Fig. 39) and 85V (Fig. 40) images depict two distinct cold areas within the occluded front. The relatively small polarization difference (85V - 85H) between them again shows the effects of volume scattering by precipitation-size ice particles. This is another indication of the increased instability forcing stronger convection within the occluded front. These T_B depressions correlate well to the bright features in the lower frequncy images as well as the bright, cold tops shown on the corresponding infrared image (Fig. 19). The cold front is still dominated by the relatively warm emission from the stable lower level clouds.

4. Precipitation Analysis at 0300 UTC 17 January 1988

At this time, the HAC algorithm (Fig. 41) depicts a solid core of significant precipitation within the frontal system. Moderate rain is shown in the northern two-thirds of the frontal system which is consistent with precipitation occurrence within oceanic cyclones (Palmen and Newton, 1969). The retrieval produces a significant rain signature in the stratiform clouds along the cold front which is synoptically reasonable in view of the overall development of the system.

However, the rain coverage produced by the HAC algorithm again falls short when compared to the 19H and 37 GHz rain threshold criteria, Fig. 34 and Fig. 38, respectively. Also, The HAC method shows a lack of precipitation within the open cell clouds west of the low. Based on the 1800 UTC rain observation at 37° N 146° W and 0316 UTC 17 January GOES infrared imagery, these clouds likely produced convective, showery activity. Again, poor spatial resolution at the lower frequencies attribute to the lack of rain signature in these isolated features.

The 85 GHz PCT precipitation coverage at 0300 UTC 17 January, illustrated in Fig. 42, shows solid coverage in two areas around the northern periphery of the low, similar to the that of HAC. The convective nature of the precipitation in these areas produces more ice. The high sensitivity of 85 GHz channels to ice above the freezing level is the basis for the identification of rain by the PCT scheme. The isolated rain cells west of the low indicate the advantage of using a scheme based on 85 GHz data with its better resolution. The disadvantage of this scattering-based method is apparent once again in its lack of rain signature associated with the stable clouds along the cold front.

E. SUMMARY

The NPS model, based on a bispectral analysis of visible and infrared data, appears to give a representative analysis of the warm frontal precipitation preceding the developing low, although the intensity was probably overestimated in some areas due to a

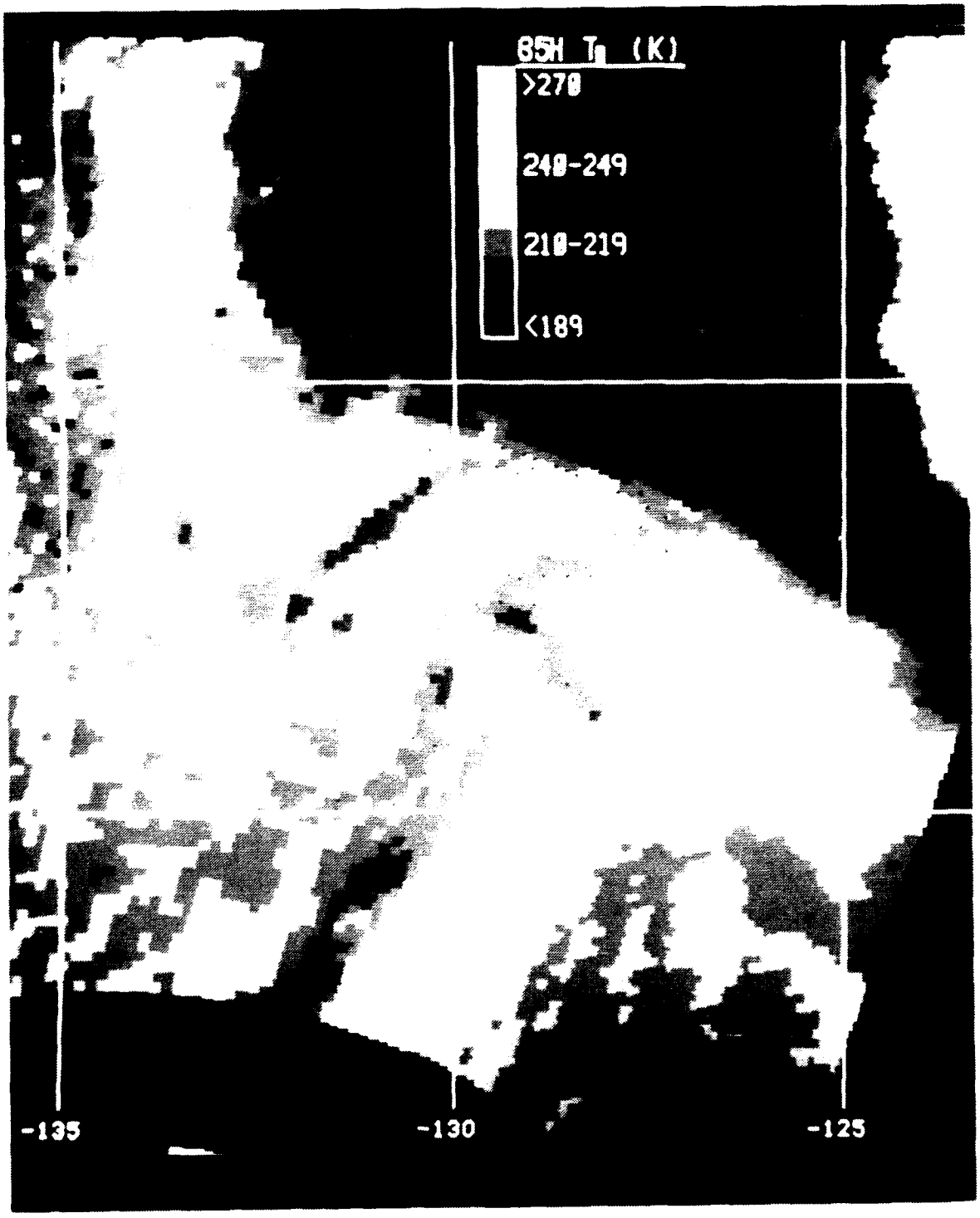

Fig. 39. SSM/I 85 GHz (horizontal) brightness temperature image at 0300 UTC 17 January 1988.

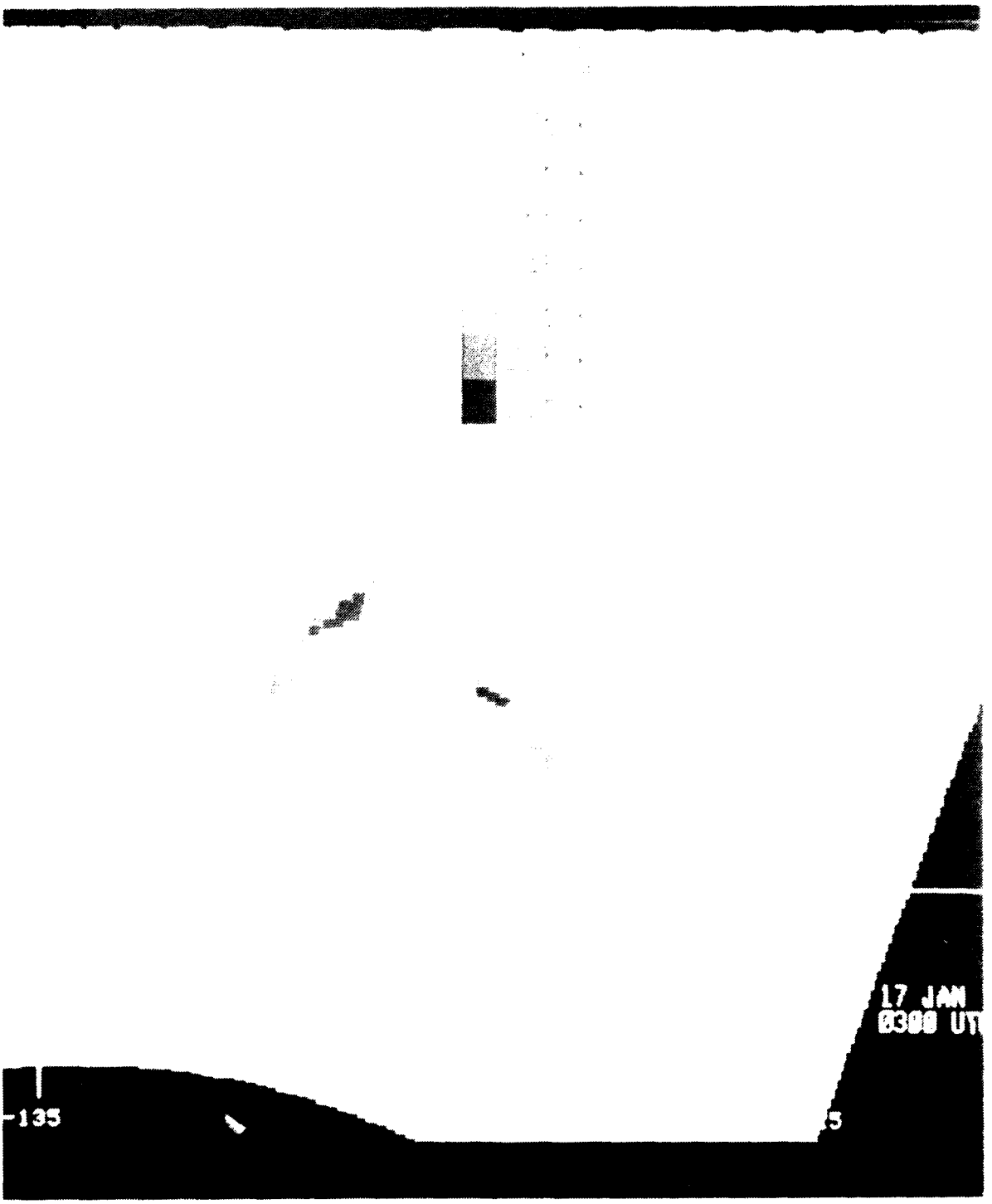

Fig. 40. SSM/I 85 GHz (vertical) brightness temperature image at 0300 UTC 17 January 1988.

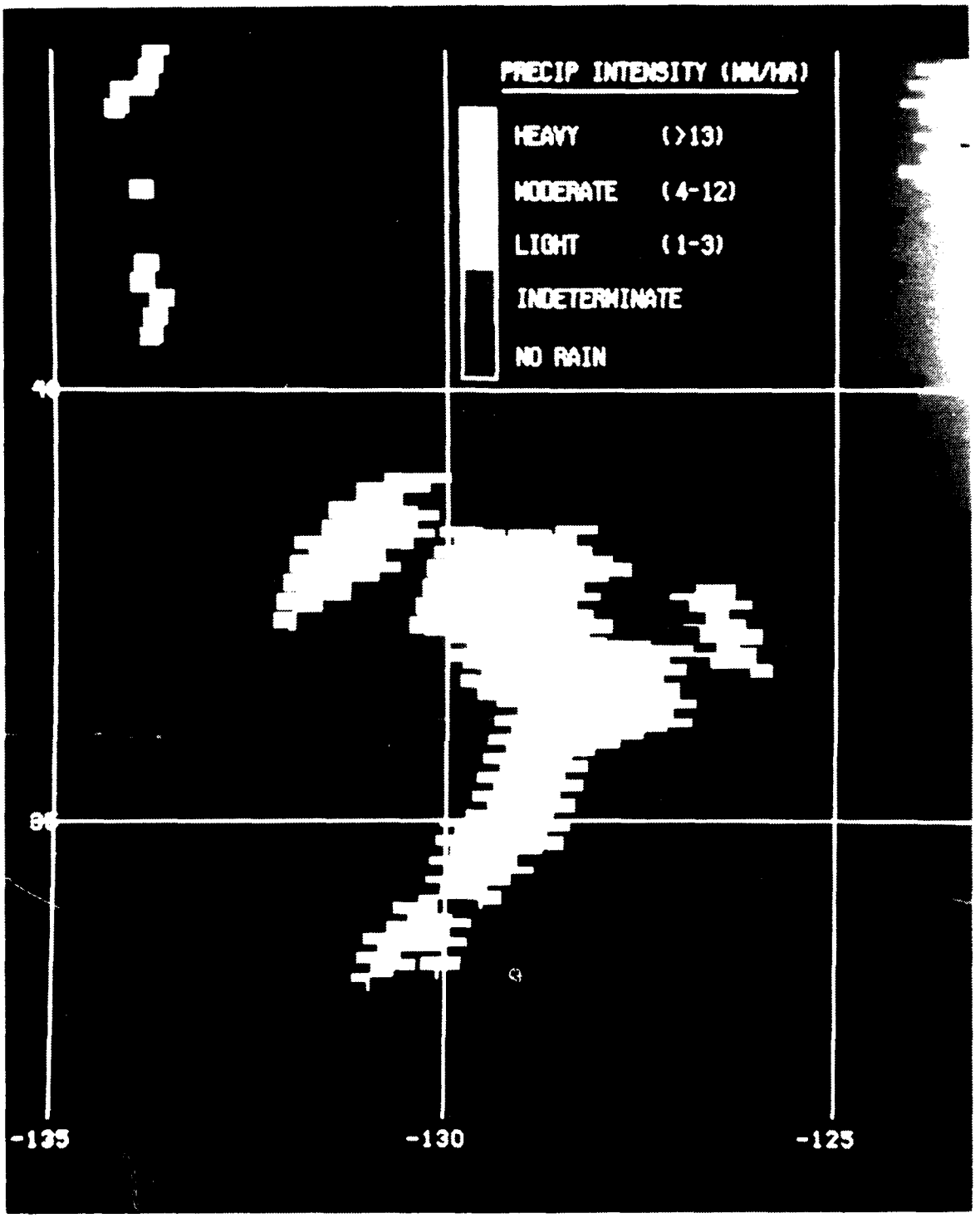

Fig. 41. SSM/I HAC precipitation estimate at 0300 UTC 17 January 1988.

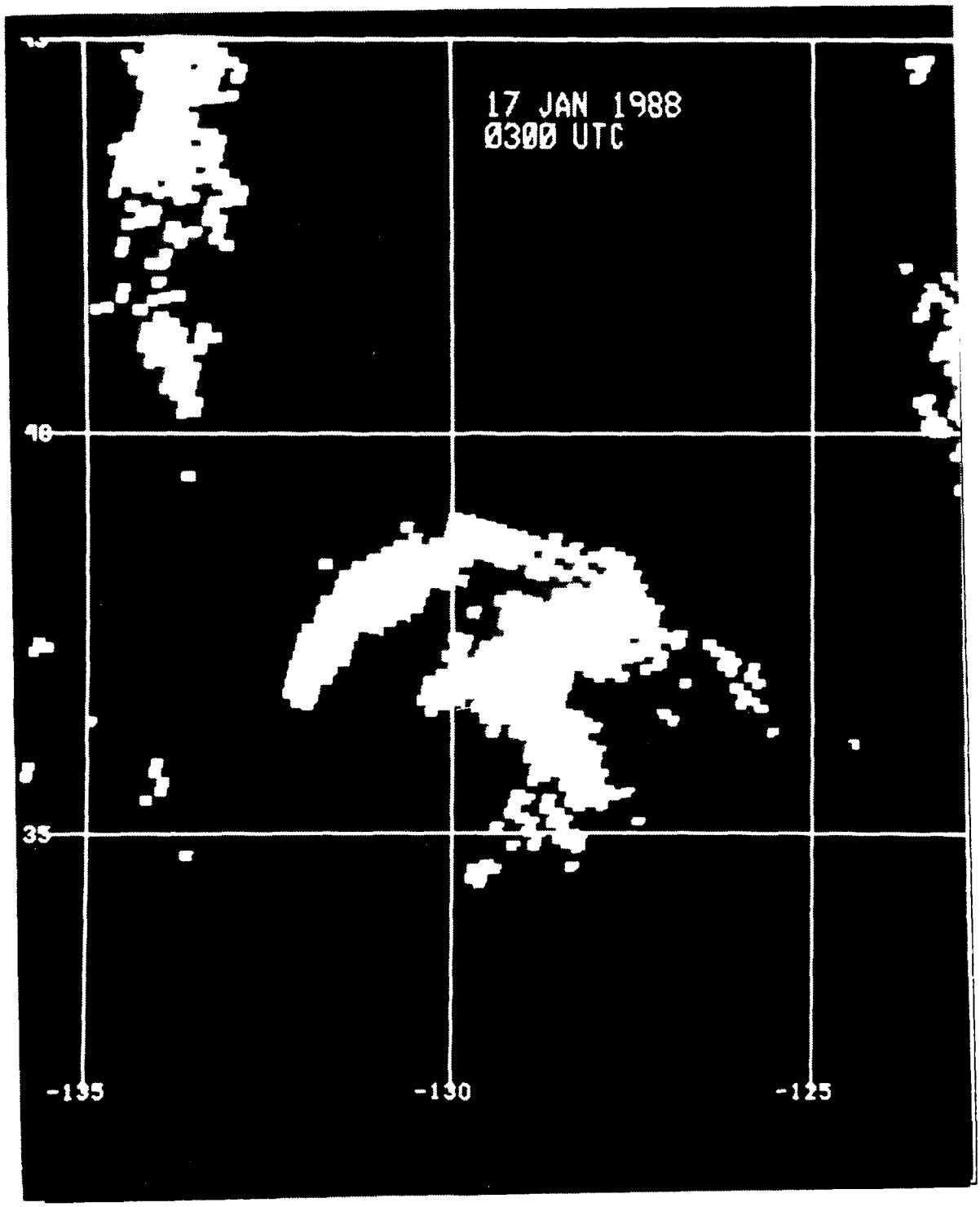

Fig. 42. SSM/I 85 GHz PCT precipitation analysis at 0300 UTC 17 January 1988: Coverage depicts PCT < 255K, rain rate ≥ 1-3 mm hr.

misclassification of cumulonimbus in areas where cirrus clearly dominated. The rain analysis was poor along the cold front where cloud tops were too warm for a rain classification, although visible imagery showed a distinct band of clouds with some embedded nimbostratus. There was little appreciable difference in rainfall analysis between GOES and AVHRR data.

The two methods based on SSM I data gave a more representative analysis of precipitation. The sophisticated algorithm developed by Hughes Aircraft Company depicted potential rainfall very well for the most part. Both the areal coverage and intensity of rain associated with the cyclone appears reasonable, based on subjective analyses of the visible and infrared imagery, and the brightness temperatures. The weaknesses of this algorithm were its underestimation of rain coverage compared to the rain threshold criteria and its inability to focus on isolated, convective precipitation.

On the other hand, the 85 GHz PCT method from the study by Spencer et al. (1988) produced a representative rainfall distribution within the cold, open-celled features to the west of the cyclone. It also analyzed the convective activity within the occluded front and in the northern front. Like the visible-infrared method, this scattering-based retrieval lacked coverage associated with warm-topped, stratiform clouds along the cyclone's cold front.

V. CONCLUSIONS AND RECOMMENDATIONS

Precipitation remains one of the most difficult weather parameters to monitor. This fact is especially evident over the open oceans where conventional data (surface and radar observations) are inadequate. This thesis illustrates that digital data from various satellite platforms, combined with modelled algorithms and thresholds, can provide a better rainfall analyses than heretofore available. Three techniques were used to evaluate precipitation for a developing winter cyclone over the eastern North Pacific Ocean: the NPS cloud precipitation model using infrared and visible data from the GOES or TIROS-N AVHRR; the sophisticated HAC rain retrieval that utilizes SSM I 19, 22 and 37 GHz data; and an algorithm developed by Spencer et al. (1988) that uses the SSM I 85 GHz polarization corrected temperature (PCT).

From a subjective analysis of the visible infrared imagery and a few ship reports, the NPS model produced reasonable results in depicting the cyclone's precipitation. The technique displayed a representative analysis of the warm frontal rainfall preceding the developing low, although the intensity was likely overestimated in some areas due to a misclassification of cumulonimbus where cirrus clearly dominated. The precipitation coverage appeared more representative as the cyclone deepened and its associated cloud structure became more definitive. The NPS model lacked rainfall coverage adjacent to the cyclone and along it's cold front, where cloud tops were too warm for a rain classification. However, a nearby ship report and the visible data gave solid evidence for some embedded precipitation within those areas. The limitations of this technique are inherent in any visible infrared scheme in that it only senses the tops of the clouds, not the hydrometeors themselves, thereby being an indirect form of estimation. Future work for improving the NPS model should include testing the threshold values for different geographic regimes, namely, land vs. ocean.

The HAC precipitation estimation, based on 19 GHz emission and 37 GHz scattering effects, produced a synoptically representative analysis of the cyclone's precipitation. It's coverage and intensity of rain correlated well with the low's cloud structure and the corresponding brightness temperature signatures. The algorithm's primary weakness was that it underestimated the rain coverage compared to the threshold values from which it is initiated, i.e. $T_B(19H) > 160K$ and $T_B(37V - 37H) < 30K$. For both times that the SSM I data was evaluated, the spatial pattern associated with these criteria were

larger (and synoptically more representative of rain coverage) than that calculated by the algorithm. Also, the HAC scheme did not depict any rain associated with smaller scale or isolated features such as the open-celled convection in the cold air west of the cyclone. This likely stems from the relatively poor resolution of the SSM/I's lower frequencies.

The strengths of the PCT method from Spencer et al. (1988) appeared to complement the weakness of the HAC retrieval. The method's sensitivity to precipitation-size ice scattering and the relatively good resolution of 85 GHz data provided a much better representation of rain within the isolated convective features. However, like the NPS model, the PCT method did not depict any rain adjacent to the cyclone and along its cold front. The 255K PCT threshold may have to be adjusted to fit the various types of rain within a typical mid-latitude winter cyclone. More studies are needed to quantify the relationships between 85 GHz brightness temperature depressions and rain rates at the surface, especially over land areas with abundant surface observations.

Ultimately, a combination of a scattering (high frequency) microwave method with an emission (low frequency) microwave scheme is needed to give the most accurate results of obtaining complete rainfall determination. Incorporation of an 85 GHz scattering method into the present HAC retrieval would provide the best opportunity for immediate improvements in rainfall estimates. Visible and infrared data will always be useful in resolving ambiguities and in identifying the types and coverage of cloud systems that are imaged by the passive microwave instruments. Efforts to estimate precipitation from visible and infrared data must continue since SSM/I data is available only twice daily. Additional satellite-based studies are required to continue progress on the difficult problem of mapping oceanic precipitation.

LIST OF REFERENCES

Atangan, J. F. H., 1988: Satellite signatures of rapid cyclogenesis. Master's Thesis, Naval Postgraduate School, Monterey, CA, 51 pp.

Barrett, E. C. and D. W. Martin, 1981: *The Use of Satellite Data in Rainfall Monitoring*. Academic Press, London, 340 pp.

Brown, O. B., J. W. Brown, and R. H. Evans, 1985: Calibration of advanced very high resolution radiometer infrared observations. *J. Geophys. Res.*, **90**, 11667-11677.

Clark, J. D., 1983: *The GOES User's Guide*, NOAA National Environmental Satellite, Data, and Information Service. 156 pp.

Harris, R. and E. C. Barrett, 1978: Toward an objective nephanalysis. *J. Appl. Meteor.*, **17**, 1258-1266.

Hollinger, J., R. Lo, G. Poe, R. Savage and J. Peirce, 1987: *Special Sensor Microwave Imager User's Guide*, Naval Research Laboratory. 120 pp.

Lauritson, L., G. J. Nelson, and F. W. Porto, 1979: Data extraction and calibration of TIROS-N NOAA radiometers. NOAA Tech. Memo, TM NESS 107, 81pp.

Lethbridge, M., 1967: Precipitation probability and satellite radiation data. *Mon. Wea. Rev.*, **95**, 487-490.

Liljas, E., 1982: Automated techniques for the analysis of satellite cloud imagery. *Nowcasting*, ed. K. Browning, Academic Press, London, 177-190.

Lovejoy, S. and G. L. Austin, 1979: The delineation of rain areas from visible and IR satellite data for GATE and mid-latitudes. *Atmosphere-Ocean*, **17**, 77-92.

Marshall, J. S. and W. McK. Palmer, 1948: The distribution of raindrops with size. *J. Meteorol.*, **5**, 165-166.

Mie, G., 1908: Beitrage zur optik truber median, speziell kolloidaler metallosungen (Contribution on the optics of scattering media, special colloidal metal solutions). *Annalen der Physik*, **25**, 377-445.

Moren, C. A., 1984: Evaluation of the SPADS automated cloud analysis model. Master's Thesis, Naval Postgraduate School, Monterey, CA, 139 pp.

Muench, H. S. and T. J. Keegan, 1979: Development of techniques to specifiy cloudiness and rainfall rate using GOES imagery data. AGFL-TR-79-0255, AD A084, 46 pp.

Nelson, C. A., 1982: Estimation and mapping of cloud and rainfall areas with an interactive computer. Master's Thesis, Naval Postgraduate School, Monterey, CA, 134 pp.

Palmen, E., and C. W. Newton, 1969: *Atmospheric Circulation Systems.* Academic Press, New York, 603 pp.

Pind, M. D., 1987: Evaluation of satellite-derived precipitation along the west coast of the United States. Master's Thesis, Naval Postgraduate School, Monterey, CA, 81 pp.

Plank, V. G., D. Atlas and W. H. Paulsen, 1955: The nature and detectability of clouds and precipitation as determined by 1.25 centimeter radar. *J. Meteor.*, **12,** 358-378.

Reynolds, D. W. and T. H. Vonder Haar, 1977: A bispectral method for cloud paramter determination. *Mon. Wea. Rev.*, **105,** 446-457.

Rosenkranz, P. W. 1978: General theoretical aspects of passive microwave remote sensing. Appendix to *High Resolution Passive Microwave Satellites* (D. H. Staelin and P. W. Rosenkranz, eds.), Massachusetts Institute of Technology, Cambridge, MS.

Spencer, R. W., 1986: A satellite passive 37 GHz scattering based method for measuring oceanic rain rates. *J. Climate Appl. Meteor.*, **25,** 754-766.

Spencer, R. W., H. M. Goodman and R. E. Hood, 1988: Precipitation retrieval over land and ocean with the SSM I: identification and characteristics of the scattering signal. Accepted by *J. Atmos. and Ocean. Tech.*

Spray, L. A., 1985: Geostationary satellite analyses of precipitation and cloud parameters. Master's Thesis, Naval Postgraduate School, Monterey, CA, 100 pp.

Wash, C. H., L. A. Spray and L. C. Chou, 1985: Satellite cloud and precipitation analysis using a minicomputer. NPS-63-85-003, 90 pp.

Wilheit, T. T., 1986: Some comments on passive microwave measurement of rain. *Bull. Amer. Meteor. Soc.*, **67,** 1226-1232.

Wilheit, T. T., A. T. C. Chang, M. S. V. Rao, E. B. Rodgers and J. S. Theon, 1977: A satellite technique for quantitatively mapping rainfall rates over the oceans. *J. Appl. Meteor.*, **16,** 551-560.

Wu, R., and J. A. Weinman, 1984: Microwave radiances from precipitating clouds containing aspherical ice, combined phase, and liquid hydrometeors. *J. Geophys. Res.*, **89,** 7170-7178.

INITIAL DISTRIBUTION LIST

		No. Copies
1.	Defense Technical Information Center Cameron Station Alexandria, VA 22304-6145	2
2.	Library, Code 0142 Naval Postgraduate School Monterey, CA 93943-5002	2
3.	Chairman (Code 63Rd) Department of Meteorology Naval Postgraduate School Monterey, CA 93943-5000	1
4.	Chairman (Code 68Co) Department of Oceanography Naval Postgraduate School Monterey, CA 93943-5000	1
5.	Professor Carlyle H. Wash (Code 63Wx) Department of Meteorology Naval Postgraduate School Monterey, CA 93943-5000	6
6.	Professor Philip A. Durkee (Code 64De) Department of Meteorology Naval Postgraduate School Monterey, CA 93943-5000	2
7.	LCDR T. F. Sheridan, USN Naval Oceanography Command Detachment Box 10, Diego Garcia FPO San Francisco 96685-2905	2
8.	Director Naval Oceanography Division Naval Observatory 34th and Massachusetts Avenue NW Washington, DC 20390	1
9.	Commander Naval Oceanography Command NSTL Station Bay St. Louis, MS 39522	1

10. Commanding Officer
Naval Oceanographic Office
NSTL Station
Bay St. Louis, MS 39522 — 1

11. Commanding Officer
Fleet Numerical Oceanography Center
Monterey, CA 93943 — 1

12. Commanding Officer
Naval Environmental Prediction Research Facility
Monterey, CA 93943 — 1

13. Chairman, Oceanography Department
U. S. Naval Academy
Annapolis, MD 21402 — 1

14. Chief of Naval Research
800 North Quincy Street
Arlington, VA 22217 — 1

15. Office of Naval Research (Code 420)
Naval Ocean Research and Development Activity
800 North Quincy Street
Arlington, VA 22217 — 1